Quasi-Steady Model Enhancements of Airborne Wind Energy Systems

Mihkel Talmar

TU Delft

The cover page photo has been provided by Kitepower B.V.
URL: thekitepower.com

Quasi-Steady Model Enhancements of Airborne Wind Energy Systems

by

Mihkel Talmar

to obtain the degree of Master of Science
in Sustainable Energy Technology
at Delft University of Technology,
to be defended publicly on 27 July 2021 at 13:00.

Student number: 5157110
Project duration: November 9, 2020 – July 27, 2021
Thesis committee:

Dr.-Ing. R. Schmehl,	TU Delft, supervisor
Dr.ir. D. de Tavernier,	TU Delft
Dr.ir. C. de Visser,	TU Delft
ir. M. Schelbergen,	TU Delft

An electronic version of this thesis is available at http://repository.tudelft.nl/.

Faculty of Electrical Engineering,
Mathematics and Computer Science

Abstract

The quasi-steady model (QSM) was developed to calculate the power output of a soft-wing airborne wind energy (AWE) system operated in pumping cycles. The comparison with experimental data shows that the original formulation of the model underestimates the power output. The model does not take inertial forces into account and highly simplifies the reel-out flight path. In this work, these assumptions are critically reviewed and their impact on the simulation results assessed.

The effect of inertial forces is analytically described for a helical flight path with fixed turning radius around the downwind axis. The derived analytical solution for this flight path verifies the formulation of inertial forces in spherical coordinates proposed in earlier studies. The proposed equations are modified and added to the QSM. Both, the analytically developed set of equations and the QSM with added inertia are compared for the helical flight case. It is observed that at larger cone angles where the tether length is rather short, but the turning radius is large, the inertial effect increases the tether force and the power output. With small cone angles this effect reverses. Based on the example case, the impact of the inertial effects on the output power computed with the QSM is limited to 1-2% for lightweight soft kites.

In the original formulation of the QSM the figure-of-eight maneuvers are not resolved. Instead, the tether is reeled out at representative constant values for the elevation, azimuth and course angles. QSM output based on real flight path coordinates is used as a benchmark to calculate the accuracy of reel-out path simplifications. The power output error of resolving reel-out flight with constant angles is on average 4.1% when compared to the reference simulations. An alternative flight path representation is developed, fitting a known figure-of-eight, lemniscate, to measured asymmetric reel-out flight paths. By flying the fitted figure in the QSM, the output power error caused by this path representation is estimated to be only 1.7% in comparison to the reference simulations. It is recommended to use this fitting method based on a class function/shape function transformation technique (CST), to parametrize the reel-out flight path, despite the added complexity.

The study has shown that the accuracy improvement by including the inertial effects in the QSM is marginal if the model is limited to lightweight soft wing simulation. As a follow-up study the inertial effects should be tested with bigger kites and heavier rigid-wing systems. The adjusted CST fitting method together with the inertial equations enable these maneuvering flight simulations in the QSM.

Preface

The two people who receive my sincerest gratitude are the thesis supervisor Dr. Ing. R. Schmehl and ir. M. Schelbergen. The help from these people in this eight-month project is enormous and their guidance has enabled me to formulate the answers for the thematic research problems in focus to bring this project to a successful end. The given thesis topic has been rewarding from the perspective of self development and has sparked my interest in alternative concepts for harvesting electricity from wind.

My special appreciation goes also to Kitepower B.V. and their representative Mr. Marcello Ghilardi who provided me with the measurement data of their pumping kite power system. This set of measurements has helped me in the validation process of developed concepts for the quasi-steady model.

The thesis committee consists of the supervisor Dr.-Ing. R. Schmehl, Dr.ir. D. de Tavernier, Dr.ir. C. de Visser and ir. M. Schelbergen, who are all affiliated to TU Delft. Please accept my deepest thanks for agreeing with the offered role and making a contributing to my graduation.

With the help of aforementioned people the project has been enjoyable and they have boosted me with innovative ideas and positive energy to make a small contribution to renewable transition. Thank you all!

Mihkel Talmar
Pärnu, June 2021

Contents

Nomenclature

Abbreviations

AWE Airborne wind energy

GWEC Global Wind Energy Council

HAWT Horizontal axis wind turbine

KCU Kite control unit

QSM Quasi-steady model

SLSQP Sequential Least Squares Programming

Coordinates

(r, θ, ϕ) Spherical coordinate system

(x_k, y_k, z_k) Coordinates of the kite

(x_w, y_w, z_w) Wind reference frame

$(x_\omega, y_\omega, z_\omega)$ Turning reference frame

Greek Letters

α	Inflow angle
β	Elevation angle
χ	Course angle
Δ	Shift of CST shape
δ	Difference between $\mathbf{L}$ and $\mathbf{L_0}$ vectors
$\dot{\chi}$	Course rate
γ	Half of the cone angle
κ	Kinematic ratio
λ	Tangential velocity factor
μ	Non-dimensional parameter, links $\overline{\lambda}$ and f_x
ω	Angular velocity
$\overline{\lambda}$	Circumferential velocity factor
ϕ	Azimuth angle
ρ	Air density
θ	Inclination angle
$\theta_{\omega,\tau}$	θ_ω projection onto tangential plane
θ_ω	Angle between wind reference frame z_w and turning reference frame z_ω

ϱ Non-dimensional turning radius

ζ Power harvesting factor

Other Symbols

A Rotor area

a, b, c, d, e, c_1, c_2 Weight parameters (universal parametric equation of lemniscate)

a_ϕ Width parameter of class function

B Bernstein polynomial

b_β Height parameter of class function

C_D Drag coefficient

C_L Lift coefficient

C_p Coefficient of performance

C_R Aerodynamic force coefficient

$c_\phi,\ c_\beta$ Centre point coordinates of class function

$C_{D,t}$ Drag coefficient of tether

d_t Tether diameter

E Lift-to-drag ratio

f Reeling factor

f_x Non-dimensional downwind speed

K Point of the kite

M Median value

m Mass of the kite

N Shape function

P Power generated

p Polynomial

p Search direction of optimizer

P_r Power extracted by the rotor of turbine

P_w Power in the wind

q Dynamic wind pressure

R Turning radius

r Radius, often as tether length in QSM

R_{min} Minimal turning radius

S Path length

S Surface area of the wing

T Time

t	Completion rate between [0, 1] or time
w	Weight of polynomial
$\mathcal{L}$	Lagranian function

Vectors

$\mathbf{a}$	Vector with optimization parameters
$\mathbf{D}$	Drag force
$\mathbf{D}_t$	Tether drag
$\mathbf{F}_a$	Aerodynamic force
$\mathbf{F}_g$	Force of gravity
$\mathbf{F}_t$	Tether force
$\mathbf{F}_{i,\omega}$	Centrifugal force
$\mathbf{F}_i$	Inertial force
$\mathbf{L}$	Lift force
$\mathbf{L}_0$	Lift force projection onto $x_\omega y_\omega$-plane
$\mathbf{v}_a$	Apparent wind velocity
$\mathbf{v}_k$	Kite velocity
$\mathbf{v}_m$	Measured wind velocity
$\mathbf{v}_r$	Tether (radial) velocity
$\mathbf{v}_w$	Wind velocity
$\mathbf{v}_{a,\tau}$	Tangential component of apparent wind velocity
$\mathbf{v}_{a,r}$	Radial component of apparent wind velocity
$\mathbf{v}_{k,\omega}$	Circumferential velocity of the kite
$\mathbf{v}_{k,\tau}$	Tangential kite velocity
$\mathbf{v}_{k,r}$	Radial speed of the kite
$\mathbf{v}_{k,x}$	Kite speed in downwind direction

1 Introduction

The global primary energy demand exceeded a yearly consumption level of 173,000 TWh during the pre-pandemic era (2019) with an estimated growth of nearly 50% by the year of 2050 [5]. As the vast majority of energy is originating from fossil fuels, the Paris Agreement driven urge for green revolution is about to increase the share of renewables in the energy generation pool. Since the biggest green energy production method hydro power is limited by specific environmental constraints (e.g. the existence of natural water reservoir), a relevance for wind and solar technologies emerges.

The horizontal axis wind turbine (HAWT) is a commonly used system for harvesting energy in wind. It has a rotor installed on top of a tower and the energy is converted from spinning motion with a generator situated in a nacelle. Changes in rotor diameter increase the rotor area and consequently the accessible wind power for HAWT. However, there are several limitations to HAWT. For on, scaling up the rotor has economic limitations accompanied by structural complications associated with withstanding environmental conditions. Furthermore, wind speed has a cubic relation to the available power in moving air. Offshore wind farms ensure more stable wind conditions compared to onshore. Nevertheless, the logarithmically increased wind speeds at altitudes above 200 m remain unavailable to conventional wind turbines. Construction challenges of tall HAWT towers are the limiting factor here. Meanwhile, at heights above 200 m wind speeds reach higher velocities and remain more persistent. Therefore, it is desirable for humanity to attempt harvesting wind at higher altitudes. Consequently, alternative solutions which could operate above HAWT levels are of great interest in terms of improving wind generation in the future. One promising technology capable of operating at greater altitudes is airborne wind energy.

Airborne wind energy (AWE) harvests wind energy at increased altitudes using a tethered aircraft or a kite. The idea is to substitute the fastest moving and the most power-producing section of HAWT rotor blades, the tips, with a kite. Furthermore, the tower and inner blades are replaced by a tether as seen in Figure 1.1. Consequently, AWE could possibly have several advantages over HAWT, including reduced material costs, shorter set-up time, and consistently higher wind speeds at altitudes above the effective range of HAWTs. [20]

The AWE concept widely investigated at TU Delft and in its start-up Kitepower is defined more specifically as the pumping kite power system. As the name indicates, this concept operates in periodic pumping cycles, composed of reel-out (traction) and reel-in (retraction) phases. The kite is performing figure of eight maneuvers during the traction phase as the tether is reeled out. At this stage the kite flies between 70 to 90 km/h, generates traction force, and eventually electricity with the use of a generator situated on the ground. When the maximum tether length has been reached, the kite changes its angle of attack and goes into depowered flight mode, reducing the traction force by 80%. As such, the kite is reeled back in. This reeling in operation consumes a small amount of energy leading to a positive energy yield from the overall cycle. At minimal tether length the kite transitions to the start of the reel-out phase and the whole cycle is repeated. [9]

The concept of pumping kite power systems has also been implemented in a simulation tool at TU Delft to make realistic power estimations for the system of Kitepower. This tool is referred to as a quasi-steady model (QSM). Yet, a comparison between the measured power data of flying the kite and the QSM simulated power output has so far indicated inconsistencies in the model. This reduces

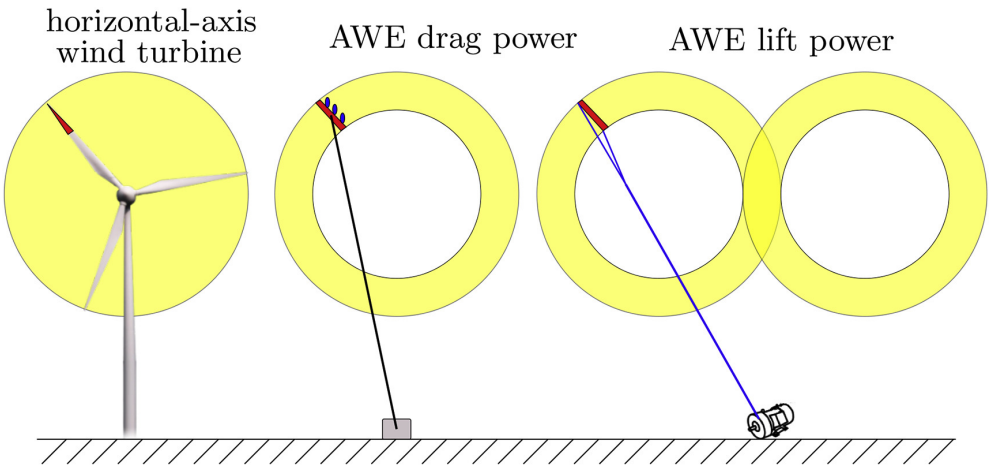

Figure 1.1: AWE systems replacing the tips of rotor blades [6]

the accuracy of energy yield calculations done using the model. It is estimated that the power error originates from the simplifications and assumptions made in the simulation tool in order to reduce computational complexity. The purpose of thesis is to evaluate and improve some of the simplifications made in the QSM about the reel-out phase concerning the maneuvering flight of the kite. **In particular, the aim is to improve QSM accuracy by including more details on the turning maneuvers of the kite.** In order to fulfil that aim, first the impact of inertia on the flight behavior is investigated. Thereafter, QSM accuracy is improved by making changes to the reel-out flight path representation in the model.

In the evaluation of inertial effects, the aim is to first analytically develop a set of equations which would solve the flight with inertial forces in a simplified simulation framework. These developed equations can be compared to the inertial force formulas proposed by previous authors. The impacts of inertial effects on the flight of the kite are then simulated and investigated in the same framework.

With the reel-out flight path representation topic the idea is to set up reference QSM simulations using the flight test measurements. The accuracy of the QSM tracking the flight path from a physical flight test could be fixed as a reference. Alternative reel-out flight paths and the QSM output received by flying them are compared to the reference simulations. The latter gives an indication about the accuracy of investigated flight paths.

The thesis is divided into three main body chapters. The state of research description in Chapter 2 brings out the context-important developments in the AWE field so far. The literature study is followed by the inertial force investigations in Chapter 3. This starts by formulating special flight frameworks of flying circles and helical paths. The inertial force equations are analytically developed for these frameworks using the free body diagrams. Later in the chapter the inertial effects are investigated from the perspective of QSM. The chapter ends with a helical flight example case. Chapter 4 introduces alternative reel-out flight paths and their impact on the accuracy of QSM. At the beginning of the chapter reference simulations are set up using QSM with minimal modifications. This is followed by an investigation of two alternative flight paths as QSM inputs. The first alternative considers finding a single azimuth-elevation combination which would simulate similar power results as time-averaged reel-out phase from the measurements. The second option tries to geometrically fit a figure to the measured path and fly the fitted figure in the QSM. In the end of this chapter an attempt for finding the most power-productive flight path is made. The latter is followed by Conclusions and Recommendations.

2

State of Research

This chapter gives a general description of AWE which is then narrowed down to a specific technology and a simulation tool investigated at TU Delft. The first section focuses on the variety of institutes active in the AWE field together with a description of various approaches to the concept. The scope is on AWE technology pumping kite power system. With the general working principles settled, the fundamental theory of flying tethered wings is presented. In chronological order the contributions to this theory by various authors are discussed. The finalized set of equations for solving the flight as series of steady-states is formed into a quasi-steady model. The latter is in the focus of this thesis. A validation of the quasi-steady model by previous authors is also discussed here which brings out the relevant issues for a research. The chapter ends by defining the research problem and questions based on it.

2.1. Airborne Wind Energy (AWE) in a Global Context

The Global Wind Energy Council (GWEC) emphasises in their latest ”Global Wind Report 2021” the installation relevance of new wind power plants. Despite the record-setting 93 GW of new capacity added in the field in 2020 the wind power growth must triple over the following decade to meet the global sustainability goal of net zero [4]. This worldwide urge for wind technology expansion undoubtedly opens up room for alternative form of wind power technologies, especially in locations where the installation of huge HAWT foundations may not be possible. This is an opportunity for AWE pioneers to build up a share in wind energy market.

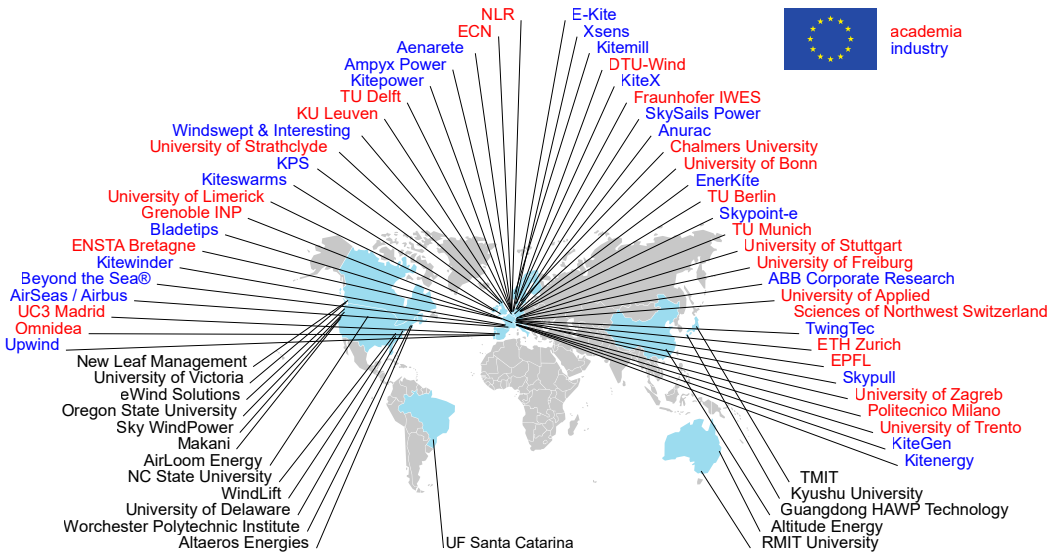

Figure 2.1: Institutions involved in AWE development (2018) [20]

Since from the 1970s, when Miles L. Loyd laid the foundation of analytical theory of AWE systems, the growth of AWE has been going by fits and starts but reached a steady increase phase by the beginning of the century. The early 2000s had only less than 10 developers in the field. Whereas, in today's date more than 60 institutions mostly in North-America and Europe are active in the AWE. Figure 2.1 brings out the most significant examples of these representatives, TU Delft being one of them. These companies and organisations are working hard to bring their AWE products to the market and many already have a fully-functioning prototype. With the rapidly growing investments the AWE could become considerable alternative to HAWT in the race for net zero emissions. [20]

2.1.1. AWE Concepts

A variety of AWE systems exists, which can be distinguished by the location of conversion from the mechanical into electrical energy. The ground-generator AWE systems (ground-gen) have a power generator situated on the ground and tethers transmit the aerodynamic forces from a kite towards the ground. Kitepower and Ampyx are TU Delft examples in that field. In fly-gen AWE systems the energy conversion is performed on a flying wing and at least one of the tethers is conductive and includes electrical cables. Makani is an example for that class. [3] The more detailed classification of AWE systems is shown in Figure 2.2.

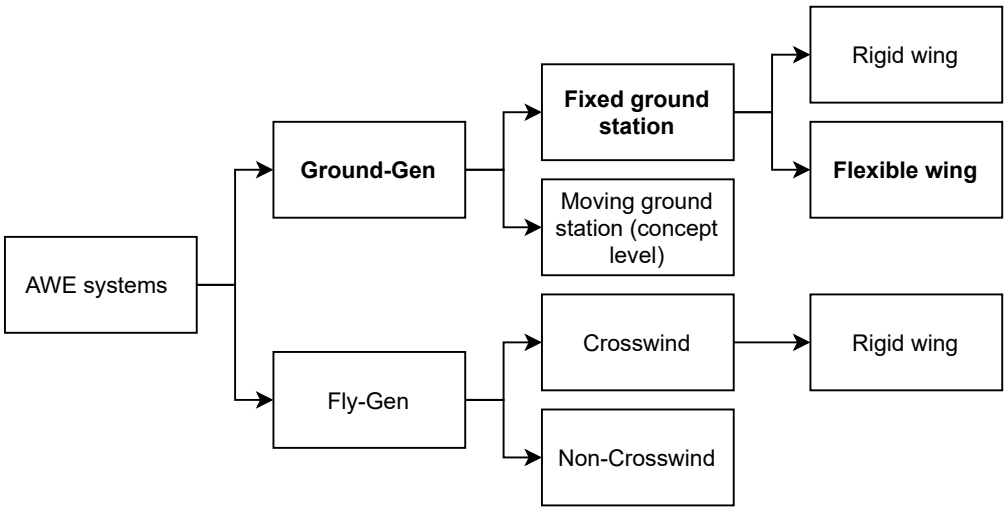

Figure 2.2: Classification of airborne wind energy systems [26]

Among the ground-gen AWE systems fixed ground station is the most actively studied by private companies. These systems work in pumping cycles, meaning the energy conversion is split at least into two phases: reel-out and reel-in. During the reel-out phase the most commonly used flying technique is the crosswind flight as the rigid or flexible wing aircraft/kite flies circular or eight-shaped figures. On contrary, moving ground station AWE system is only a hypothetical concept without a working prototype yet. The idea is to generate energy from the movement of ground station without winding the tether. This way always positive power flow would be possible and the connection to the grid could be simplified. However, the realisation of this system could be more complex due the movement of the ground station. [3]

In the fly-gen AWE systems both crosswind and non-crosswind flying techniques are used. For the crosswind flying manoeuvre the aircraft lifted by wings has turbines attached to it. This type of aircraft harvests relative wind speed as it flies through the air. The turbines of crosswind fly-gen AWE systems can operate at very high rotational speeds, meaning gearbox is made unnecessary and the shaft could directly be connected to the generator. This way the system is lighter and more reliable in terms of mechanical breakdowns. As opposed to, non-crosswind fly-gen AWE systems have bigger operational variability. Usually the power is generated by using a turbine. However, the aircraft itself is lifted by either using rotors and thrust or buoyancy effect from lighter-than-air-gas in the aerostats (e.g. balloon). [7, 3]

2.1.2. Rigid vs Flexible Wings

In ground-gen AWE systems both rigid and flexible wings are used, whereas for the fly-gen the choice is only for rigid wings. These two approaches differ not only in the structure of the wing but also in what forces act on it and how does it reflect in the flight path.

The rigid wings have a structure which maintains the shape no matter of ambient wind conditions but it has more mass for the surface area. They are designed to fly faster than flexible wings and have bigger lift-to-drag ratio. This feature makes them efficient in power generation but more influenced by the gravitational and inertial effects. Both of these forces increase with bigger mass. The inertial effects are also increased by the velocity of the kite and the latter tends to be large for rigid wing flight, meaning the system is influenced more by dynamic effects. [7]

The flexible wings, on the other hand, retain their shape only due airflow and the aerodynamic load distribution on wing. They weigh much less than rigid wings and are therefore safer to operate but do not develop as high velocity of the wing. Due these characteristics the gravity and inertial forces are also smaller in these systems. The flight of a flexible wing system is not driven by considerable dynamic effects and they happen in a shorter time span. This observation becomes crucial if the flight of the wing is simulated. The time period of dynamic effects is often approximated to be as short for flexible wings that relatively accurate results could be achieved with steady-state calculations. This is also a reason why the dynamic effects as inertia are often excluded from flexible wing simulations. [7, 25]

2.1.3. Pumping Kite Power System

The AWE concept widely investigated at TU Delft and in Kitepower belongs to a fixed ground generation and flexible wing class marked with bold text in Figure 2.2. The system runs in three phases: reel-out where the power is generated using traction force and the flight path resembles consecutive figures of eight, reel-in where the starting tether length is restored and transition phase where the depowered mode of the kite switches to powered flight. As can be seen in Figures 2.3 and 2.4 Kitepower pumping kite power system uses an inflatable kite which flies these three phases as pumping cycles. The kite is operated using a single tether and the heavy system components responsible for the energy conversion from traction force to electricity are situated on the ground. The idea of a single tether is to minimize the energy losses initiated from aerodynamic drag but at the same time making the kite uncontrollable from the ground. Therefore, remote-controlling is required, meaning the kite control unit (KCU) needs to be installed at the junction of a single tether and the bridle line system. The KCU forces the kite to fly on a well-defined crosswind trajectory maximizing the energy yield. To synchronize the whole pumping cycle, the KCU is exchanging data with the control centre and wind meter via wireless network. Both of the latter units are situated on the ground together with a drum/generator module, power electronics and a battery module, forming together the ground station. The presence of batteries is required to store the energy during the reel-out when the kite flies figures of eight and to provide only a fraction of stored energy for the reel-in process. The latter is possible due reduced traction force by aligning the kite with wind. [24]

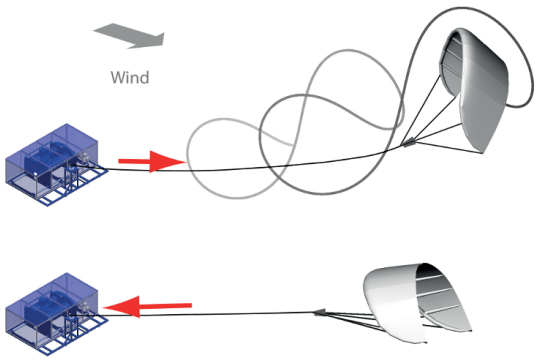

Figure 2.3: The pumping concept of Kitepower system [9]

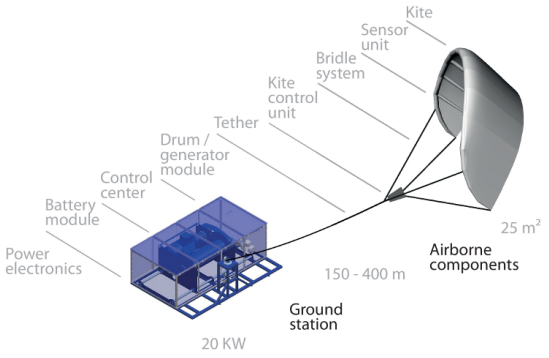

Figure 2.4: Kitepower system components [9]

2.2. Loyd's Theory

In 1980 Miles L. Loyd developed the fundamental relations in generating power with kites. In his paper "Crosswind kite power" Loyd provides equations for two types of kite flying techniques: non-maneuvering simple kite and maneuvering crosswind kite. As an assumption the weight of the kite is neglected in his work together with any impact the tether has on the system. [11]

A simple kite is facing into wind and the power is generated with an unwinding tether from a drum. The forces and velocities acting on this non-maneuvering kite are shown in Figure 2.5. Using the aerodynamic force definition

$$\mathbf{F}_a = \mathbf{L} + \mathbf{D}, \tag{2.1}$$

lift and drag force equations

$$L = \frac{1}{2}\rho C_L v_a^2 S \tag{2.2}$$

$$D = \frac{1}{2}\rho C_D v_a^2 S \tag{2.3}$$

and the relation $\mathbf{F}_t = -\mathbf{F}_a$ for a massless kite together with the apparent wind velocity definition

$$\mathbf{v}_a = \mathbf{v}_w - \mathbf{v}_k, \tag{2.4}$$

Loyd finds the following relation for normalized tether force

$$\frac{F_t}{qS} = C_R \frac{\left[\sqrt{1 + E^2(1 - f^2)} - f\right]^2}{1 + E^2}. \tag{2.5}$$

In Equation 2.5 q is the dynamic wind pressure, E lift-to-drag ratio and f reeling factor of the kite.

$$q = \frac{1}{2}\rho v_w^3 \tag{2.6}$$

$$E = \frac{L}{D} \tag{2.7}$$

$$f = \frac{v_t}{v_w} \tag{2.8}$$

The resultant aerodynamic force coefficient could be calculated from lift C_L and drag C_D coefficients with

$$C_R = \sqrt{C_L^2 + C_D^2} \tag{2.9}$$

but Loyd assumed the power generation to be dominated by the lift force, meaning the lift-to-drag ratio is large. This leads to $C_R \approx C_L$. The resultant aerodynamic coefficient C_R based on that assumption could be substituted with the lift coefficient C_L if one wants to simplify Equation 2.5. [11]

Loyd uses a non-dimensional power harvesting factor

$$\zeta = \frac{P}{P_w S} = f\frac{F_t}{qS}, \tag{2.10}$$

where power in wind is

$$P_w = \frac{1}{2}\rho v_w^3 \tag{2.11}$$

and Equation 2.5 expands into

$$\zeta = C_R \frac{f\left[\sqrt{1 + E^2(1 - f^2)} - f\right]^2}{1 + E^2}. \tag{2.12}$$

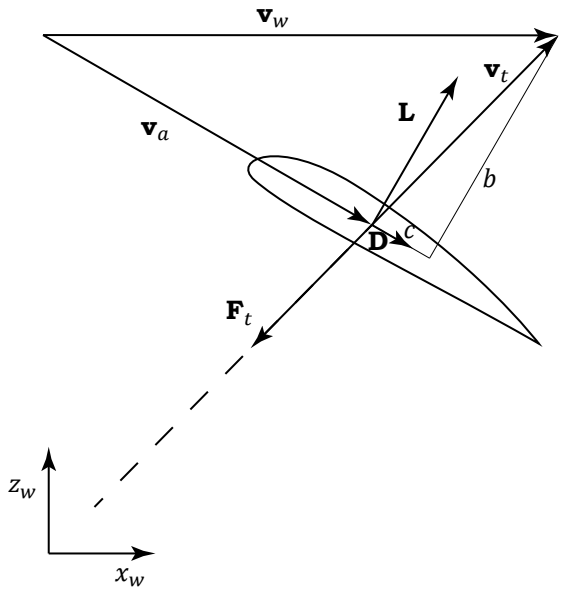

Figure 2.5: Forces and velocities on a weightless non-maneuvering simple kite [11]

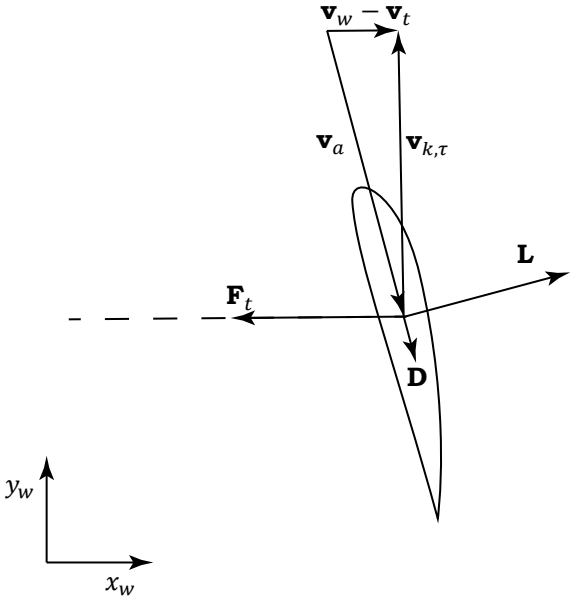

Figure 2.6: Forces and velocities on a weightless maneuvering crosswind kite [11]

Equation 2.12 is later used for a numerical comparison with the crosswind kite.

As a second type of flight Loyd investigates a maneuvering kite. When the kite flies to a position where the tether is aligned with wind direction the motion becomes crosswind. This crosswind flight together with forces and velocities is shown in Figure 2.6. Expanding the apparent wind velocity Equation 2.4 to

$$\mathbf{v}_a = \mathbf{v}_w - \mathbf{v}_t - \mathbf{v}_{k,\tau}, \tag{2.13}$$

where $\mathbf{v}_t$ is the tether velocity and $\mathbf{v}_{k,\tau}$ the tangential kite velocity, the non-dimensional tether force for the crosswind kite becomes

$$\frac{F_t}{qS} = C_R(1 + E^2)(1 - f)^2. \tag{2.14}$$

Again one could assume $E \gg 1$ and change C_R to C_L and $(1 + E^2)$ to E^2 if further simplification is required. Loyd writes the crosswind kite power harvesting factor as

$$\zeta = C_R(1 + E^2)f(1 - f)^2. \tag{2.15}$$

With the optimal reeling factor

$$f_{opt} = \frac{1}{3}, \tag{2.16}$$

Equation 2.15 becomes

$$\zeta_{opt} = \frac{4}{27} C_R \left(\frac{C_R}{C_D}\right)^2. \tag{2.17}$$

This also defines the upper limit for power one could harvest from wind using the crosswind kite. [11]

As a final part of his paper Loyd compares the simple (regular) kite with the crosswind kite. According to his results it is beneficial to fly the kite in crosswind motion since the power harvesting factor ξ is much higher for that case. One could also see that from Figure 2.7 where Loyd's equations are put into practice for a kite of the same size. These diagrams show that with the simple kite the power gain

is limited even if the lift-to-drag ratio approaches infinity. For the crosswind flight this is not the case as increased $\frac{C_L}{C_D}$ amplifies the power harvesting factor.

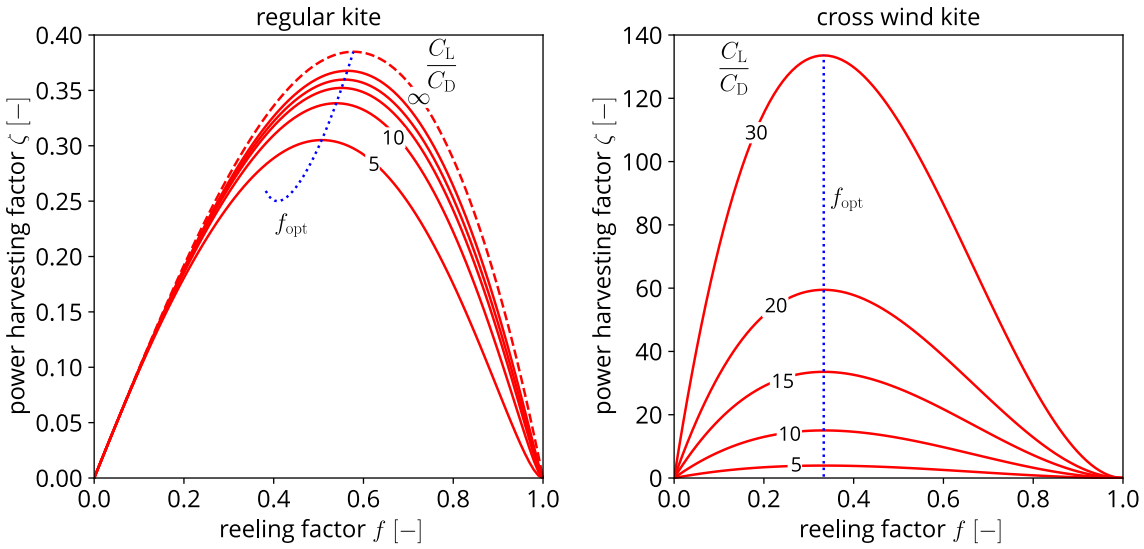

Figure 2.7: Power harvesting factor comparison: regular (simple) kite vs crosswind kite [20]

2.3. Introducing Spherical Coordinates

Loyd proved flying a maneuvering kite could give promising power harvesting results. For a representative of this flight technique: in a pumping kite power system the kite flies spherically around a fixed ground station. It would be more suitable to describe these kite maneuvers in spherical coordinates instead of Cartesian ones. The position of an object is given with three parameters in the spherical coordinates: (r, θ, ϕ). For a feasible flight these coordinates must be in certain ranges: e.g. the flight does not happen underneath the surface of the Earth or cannot leave the half sphere of downwind. These ranges together with an explanation of each coordinate are given in Table 2.1.

Coordinate	Name	Range	Definition
r	radius	$0 \leq r \leq \infty$	distance from the origin of axes
θ	inclination	$0 \leq \theta \leq \frac{\pi}{2}$	angle from the positive z-axis
ϕ	azimuth	$-\frac{\pi}{2} \leq \phi \leq \frac{\pi}{2}$	angle from the positive x-axis on x-y plane

Table 2.1: The explanation of spherical coordinates [28]

It is possible to switch between the Cartesian and spherical coordinates using certain relations. For that purpose Figure 2.8 shows how the two coordinate systems are connected to each other. One could calculate (r, θ, ϕ) values with Equations 2.18-2.20.

$$r = \sqrt{x^2 + y^2 + z^2} \tag{2.18}$$

$$\theta = \arctan \frac{\sqrt{x^2 + y^2}}{z} \tag{2.19}$$

$$\phi = \arctan \frac{y}{x} \tag{2.20}$$

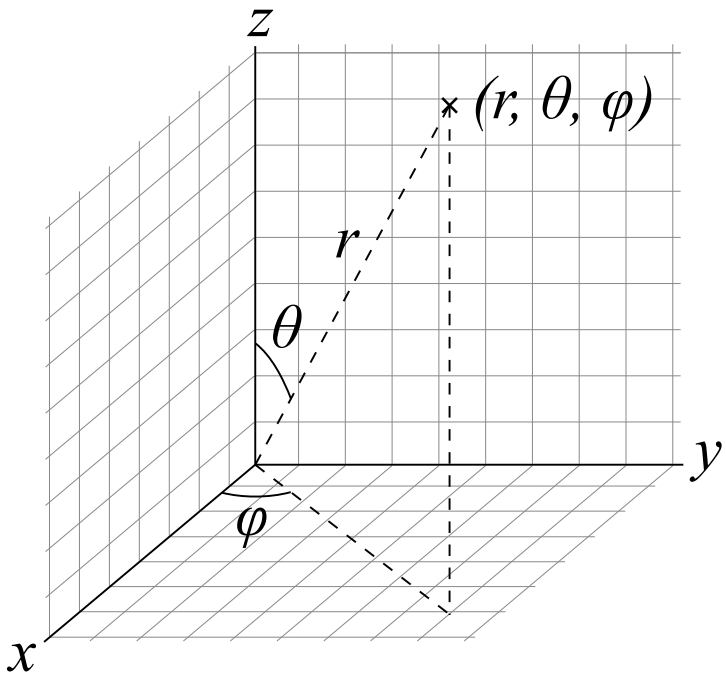

Figure 2.8: Spherical coordinate system [23]

2.3.1. Improvements by Argatov et al

Argatov et al introduced spherical coordinates in describing the flight of a kite. [1] They used Newton's law of motion as a fundamental equation for their analysis to investigate the total forces acting on the kite. These total forces are described as a sum of aerodynamic and gravitational force

$$\mathbf{F} = \mathbf{F}_g + \mathbf{F}_a, \tag{2.21}$$

where $\mathbf{F}_g$ of the kite is calculated as

$$\mathbf{F}_g = -mg(\cos\theta\mathbf{e}_r - \sin\theta\mathbf{e}_\theta). \tag{2.22}$$

In this equation m is the mass of the kite, g is the gravitational acceleration of the Earth and the basis vectors are denoted with $\mathbf{e}_r$ and $\mathbf{e}_\theta$. For the aerodynamic force $\mathbf{F}_a$ they expand the aerodynamic drag with the impact of the tether. This means the effective lift-to-drag ratio becomes

$$E = \frac{L}{D + D_t}, \tag{2.23}$$

where D_t stands for the tether drag force acting on the kite. One could calculate it with

$$D_t = \frac{1}{8}\rho d_t r C_{D,c} v_a^2. \tag{2.24}$$

In Equation 2.24 d_t is the tether diameter, r the length of the tether and $C_{D,c}$ marks the drag coefficient of a cylinder. Combining Equations 2.23 and 2.24 Argatov et al obtained effective lift-to-drag ratio as

$$E = \frac{C_L}{C_D + \frac{C_{D,t} r d_t}{4S}}. \tag{2.25}$$

Taking use of the new E the authors defined an equation for mechanical power of a kite wind generator. Considering all the forces acting on the kite in parallel to tether, the power harvesting factor is calculated as

$$\zeta = f\left(C_L E\sqrt{1+E^2}(\sin\theta\cos\phi - f)^2 + \frac{\sum F_\parallel}{qS}\right). \tag{2.26}$$

$F_{\parallel}$ denotes all the forces acting in radial direction. This includes the aerodynamic, gravitational and centrifugal components. The latter in radial direction is given as

$$F_{cf} = mr(\dot{\theta}^2 + \dot{\phi}^2 \sin^2 \theta). \tag{2.27}$$

By the end of their paper the authors conduct a numerical example which gives them only 0.8% correction when counting for the gravitational, centrifugal and friction forces compared to the exclusion of these impacts from the analysis. [1]

2.4. Solving Steady-States of Tethered Wings

In 2013 Schmehl et al developed a theory for solving the instantaneous stedy-states of a kite. [21] Their work is mostly built on the contributions of Loyd and Argatov et al and is focused on the pumping kite power system with the following assumptions.

- The kite has a relatively large surface-to-mass ratio, meaning the describable dynamic processes have a short timescale compared to a complete pumping cycle. According to this the flight manoeuvres could be described with a force balance between the aerodynamic, tether, gravitational and inertial forces.
- Tether is considered inelastic in this analysis without any sagging.
- The forces acting on a wing are condensed into a single point **K** which is a point mass representation of the kite.

The authors use similarly to Argatov et al spherical coordinate system (r, θ, ϕ) but introduce a tangential plane τ which is perpendicular to the tether. The course angle χ shows the direction of the flight on that local tangential plane by measuring the angle according to the right hand rule from the base vector $\mathbf{e}_\theta$. The framework used by the authors is illustrated in Figure 2.9.

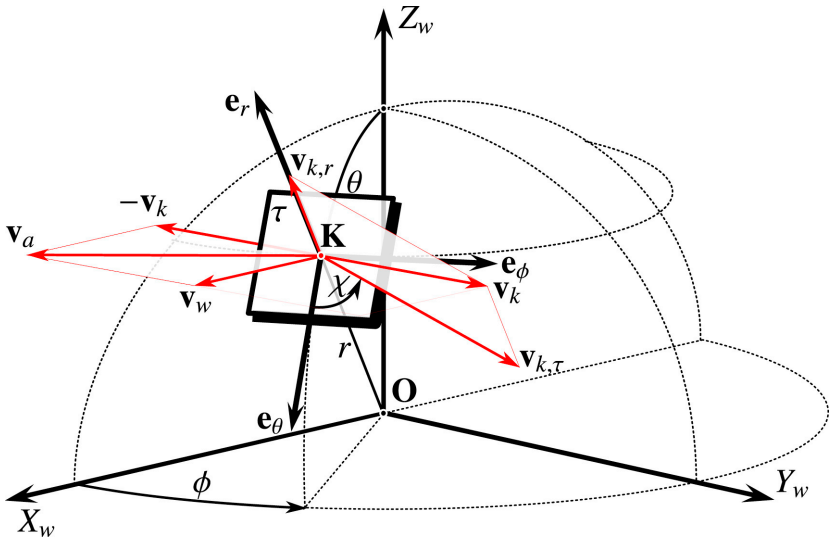

Figure 2.9: Wind reference frame (x_w, y_w, z_w) together with spherical coordinates (r, θ, ϕ), the decomposition of kite velocity v_k and apparent wind velocity $v_a = v_w - v_k$ [21]

According to the steady-state analysis the kite has a certain velocity at each instance of time which is composed of the reel-out speed (the radial component of velocity $\mathbf{v}_{k,r}$) and the velocity of the kite flying on the tangential plane (the tangential component $\mathbf{v}_{k,\tau}$).

$$\mathbf{v}_k = \mathbf{v}_{k,r} + \mathbf{v}_{k,\tau} \tag{2.28}$$

Using Equations 2.28 and 2.13 the authors obtain the apparent wind velocity experienced by the kite in spherical coordinates.

$$\mathbf{v}_a = \begin{bmatrix} \sin\theta\cos\phi \\ \cos\theta\cos\phi \\ -\sin\phi \end{bmatrix} v_w - \begin{bmatrix} 1 \\ 0 \\ 0 \end{bmatrix} v_{k,r} - \begin{bmatrix} 0 \\ \cos\chi \\ \sin\chi \end{bmatrix} v_{k,\tau} \tag{2.29}$$

With the reeling factor f definition from Equation 2.8 and defining the kite tangential velocity factor λ as

$$\lambda = \frac{v_{k,\tau}}{v_w}, \tag{2.30}$$

the finalized form of the apparent wind velocity could be written as

$$\mathbf{v}_a = \begin{bmatrix} \sin\theta\cos\phi - f \\ \cos\theta\cos\phi - \lambda\cos\chi \\ -\sin\phi - \lambda\sin\chi \end{bmatrix} v_w. \tag{2.31}$$

The apparent wind velocity Equation 2.31 and the definition of aerodynamic force Equation 2.1 give Schmehl et al the fundamentals for developing the non-dimensional tether force and the power equations in spherical coordinates first for the massless kite and then counting for the mass together with the effect of gravity and inertia.

2.4.1. Model with Negligible Effect of Gravity and Inertia

When the mass and the inertial contributions are negligible in the system the division of lift and drag force becomes a fundamental substitution for the kinematic ratio κ. This relation

$$\kappa = \frac{v_{a,\tau}}{v_{a,r}} = \frac{L}{D} \tag{2.32}$$

is derived from the geometric similarity shown in Figure 2.10 where $\mathbf{F}_a$ is aligned with $\mathbf{v}_{a,r}$ and $\mathbf{D}$ with the aerodynamic velocity $\mathbf{v}_a$ itself. These alignments give a justification for the geometric similarity. [21]

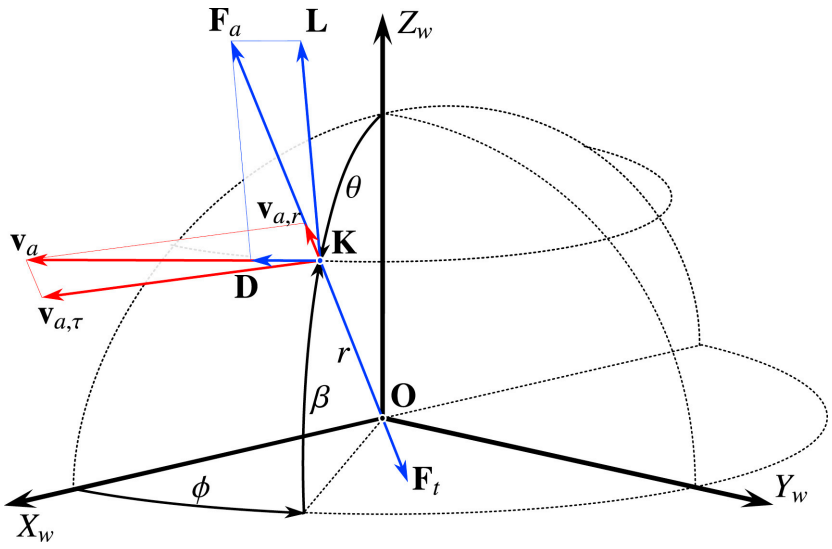

Figure 2.10: The geometric similarity of $\mathbf{v}_a$ and $\mathbf{F}_a$ [21]

From the apparent wind velocity Equation 2.29 Schmehl et al write an equation for the tangential components of the apparent wind velocity as

$$v_{a,\tau} = v_w\sqrt{(\cos\theta\cos\phi - \lambda\cos\chi)^2 + (\sin\phi + \lambda\sin\chi)^2}. \tag{2.33}$$

Another way of presenting $v_{a,\tau}$ could be obtained by combining the fundamental relation Equation 2.32 and the radial components of Equation 2.29 into

$$v_{a\tau} = (\sin\theta\cos\phi - f)v_w\frac{L}{D}. \tag{2.34}$$

Using both Equations 2.33 and 2.34 and solving for the tangential velocity factor λ the authors calculate

$$\lambda = a + \sqrt{a^2 + b^2 - 1 + \left(\frac{L}{D}\right)^2 (b - f)^2}, \tag{2.35}$$

where

$$a = \cos\theta\cos\phi\cos\chi - \sin\phi\sin\chi \tag{2.36}$$
$$b = \sin\theta\cos\phi. \tag{2.37}$$

The definition implies that this tangential velocity factor can only be positive. [21]

In the case of massless kite with no gravitational nor inertial effects the quasi-steady motion of a wing experiences a force balance between the tether force and the aerodynamic force

$$\mathbf{F}_t = -\mathbf{F}_a. \tag{2.38}$$

The authors modify Loyd's non-dimensional tether force Equation 2.14 with azimuth ϕ and inclination θ angle which enables solutions for cases when the tether is not perfectly aligned with wind direction. Together with Equations 2.6 and 2.9 the non-dimensional power equation becomes

$$\frac{F_t}{qS} = C_R\left[1 + E^2\right](\sin\theta\cos\phi - f)^2. \tag{2.39}$$

With the definition of power harvesting factor ζ from Equation 2.10 the authors write

$$\zeta = \frac{P}{P_w S} = C_R\left[1 + \left(\frac{L}{D}\right)^2\right] f(\sin\theta\cos\phi - f)^2 \tag{2.40}$$

for the massless maneuvering kite in spherical coordinates. For the maximum power of pumping kite power system the optimal reeling factor becomes

$$f_{opt} = \frac{1}{3}\sin\theta\cos\phi. \tag{2.41}$$

This is also a more universal version of Loyd's reeling factor given in Equation 2.16. [21]

2.4.2. Model with Gravity and Inertia

To improve the accuracy of steady-state calculations in spherical coordinates Schmehl et al use similarly to Argatov et al the gravitational and inertial force corrections to satisfy the force balance

$$\mathbf{F}_t = -\mathbf{F}_a - \mathbf{F}_g - \mathbf{F}_i. \tag{2.42}$$

The gravitational force is expressed as

$$\mathbf{F}_g = m\begin{bmatrix} -\cos\theta \\ \sin\theta \\ 0 \end{bmatrix} g, \tag{2.43}$$

where m is the mass and g the gravitational constant. For the inertial force the authors use Newton's law of motion and write

$$\mathbf{F}_i = -m\begin{bmatrix} \ddot{r} - r\dot{\theta}^2 - r\dot{\phi}^2\sin^2\theta \\ r\ddot{\theta} + 2\dot{r}\dot{\theta} - r\dot{\phi}^2\sin\theta\cos\theta \\ r\ddot{\phi}\sin\theta + 2\dot{r}\dot{\phi}\sin\theta + 2r\dot{\theta}\dot{\phi}\cos\theta \end{bmatrix}, \tag{2.44}$$

where the first derivatives are given as

$$\dot{r} = f v_w \tag{2.45}$$

$$\dot{\theta} = \frac{\lambda v_w}{r} \cos\chi \tag{2.46}$$

$$\dot{\phi} = \frac{\lambda v_w}{r} \frac{\sin\chi}{\sin\theta} \tag{2.47}$$

and the second derivatives as

$$\ddot{r} = 0 \tag{2.48}$$

$$\ddot{\theta} = -\dot{\theta}\left(\frac{\dot{r}}{r} + \dot{\chi}\tan\chi\right) \tag{2.49}$$

$$\ddot{\phi} = -\dot{\phi}\left(\frac{\dot{r}}{r} - \dot{\chi}\frac{1}{\tan\chi} + \dot{\theta}\frac{1}{\tan\theta}\right). \tag{2.50}$$

Dividing Equations 2.22 and 2.44 into vector components of spherical coordinates $(\mathbf{e}_r, \mathbf{e}_\theta, \mathbf{e}_\phi)$ the aerodynamic force becomes into

$$F_{a,\theta} = -F_{g,\theta} - F_{i,\theta} \tag{2.51}$$

$$F_{a,\phi} = -F_{i,\phi} \tag{2.52}$$

$$F_{a,r} = \sqrt{F_a^2 - F_{a,\theta}^2 - F_{a,\phi}^2}, \tag{2.53}$$

where the radial components of these forces are balanced by the tether force. [21]

Schmehl et al bring an attention to the fact that with the additional force components (gravitational and inertial forces) the geometric similarity in Equation 2.32 is not valid anymore for lift-to-drag substitution. The tangential velocity factor equation remains

$$\lambda = a + \sqrt{a^2 + b^2 - 1 + \left(\frac{v_{a,\tau}}{v_{a,r}}\right)^2 (b-f)^2} \tag{2.54}$$

and similarly it is not possible to directly calculate the non-dimensional tether force. Instead the apparent wind velocity calculation holds as

$$\frac{F_a}{qS} = C_R\left[1 + \left(\frac{v_{a,\tau}}{v_{a,r}}\right)^2\right](\sin\theta\cos\phi - f)^2. \tag{2.55}$$

The lift-to-drag ratio could be now found with

$$E = \sqrt{\left(\frac{F_a v_a}{\mathbf{F}_a \cdot \mathbf{v}_a}\right)^2 - 1}, \tag{2.56}$$

but this equation requires an iterative solution process where each new kinematic ratio κ_{i+1} originates from the difference of current E_i value and the target E^* value. The updated kinematic ratio is given as

$$\kappa_{i+1} = \kappa_i \sqrt{\frac{E^*}{E_i}}. \tag{2.57}$$

This iterative process becomes a core of quasi-steady solution in the pumping kite power system. [21, 25]

2.4.3. Flight Cycle in Quasi-Steady Model (QSM)

In 2018 van der Vlugt et al published an article about making power estimations for pumping kite power system using quasi-steady model (QSM). [25] This simulation tool is an implementation of theory developed by Schmehl et al discussed in Section 2.4 with an exception of excluding the inertial forces. The authors justify it with the small impact of inertial effects on soft-wing kites. The whole concept of QSM is based on solving steady-states for all three pumping phases separately with the phase-specific assumptions and then adding them together to form a unified pumping cycle one could observe in Figure 2.11. The following subsections describe their approach for each phase.

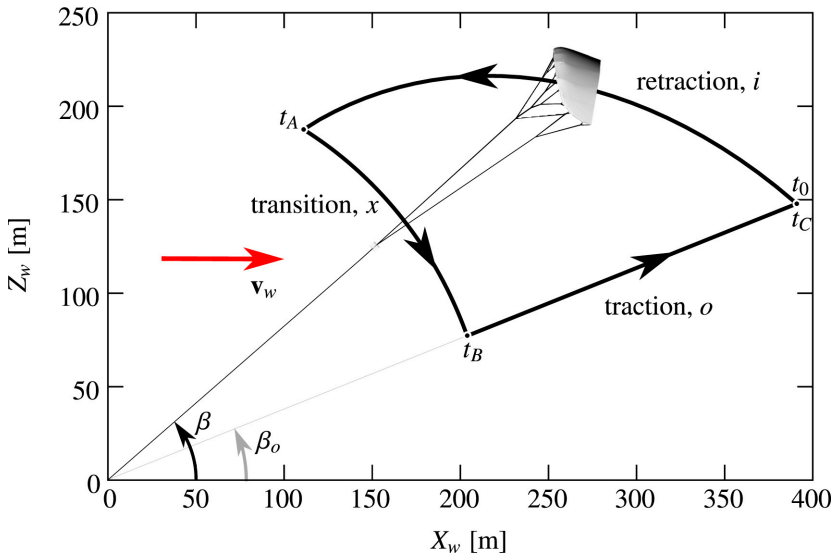

Figure 2.11: Three phases of pumping kite power system [25]

Retraction (Reel-In) Phase

The retraction phase serves an essential task of reeling in the kite after a successful reel-out operation. Since during this phase the energy is not generated but consumed the task in focus is to keep the energy loss minimal. This is achieved by reducing the angle of attack to align the kite with the direction of wind. The process starts at maximal tether length r_{max} and finishes at r_{min}, meantime the energy consumption being calculated with the instantaneous traction power P_i over the reel-in time Δt_i. [25]

The assumption made in the QSM fixes the values for aerodynamic lift C_L and drag C_D coefficient in depowered mode for the whole retraction phase. The kite is made to fly upwards with course angle value $\chi_i = 180°$ during the reeling in process. The kite trajectory in this phase goes along $\phi_i = 0°$ plane and the position of the kite is updated with

$$\mathbf{r}(t + \Delta\mathbf{t}) = \mathbf{r}(t) + \mathbf{v}_k(t)\Delta\mathbf{t}, \tag{2.58}$$

where Δt indicates the integration time step. [25]

Three possible control strategies could be used in the retraction phase to define the optimal reeling factor f. These are: force control, velocity control and power control. The constant tether force $F_{t,i}$ which has couple of benefits is used in this case. Firstly, the retraction time at given tensile strength is reduced due minimal sagging with the force control. Secondly, the net power output of the system is maximized since the reel-in phase with negative power is shortened. The reeling factor could be calculated in this case with

$$f = \sin\theta\cos\phi \pm \sqrt{\frac{F_{t,i}}{qSC_R\left[1 + \left(\frac{L}{D}\right)^2\right]}}, \tag{2.59}$$

where only the smaller value of reeling factor will be used, otherwise Equation 2.31 would calculate to a negative $v_{a,r}$ when $f \geq \sin\theta\cos\phi$ is valid. This again means the aerodynamic force F_a would point

towards the ground station which cannot be the case. The retraction phase comes to an end when r_{min} is reached and the kite moves to a transition phase. [25]

Transition Phase
The transition phase serves as a switch between the retraction phase settings and the start settings of the traction phase. During the transition the kite needs to fly from larger elevation angle β to lower target elevation β_0 used for the reel-out. Another essential transitioning parameter is the tether force F_t which needs to increase from the low reel-in value to the desired traction phase $F_{t,0}$. The latter is done by setting the aerodynamic coefficients C_L and C_D to power mode. In the transition phase the kite is flying downwards, meaning the course angle is $\chi = 0°$. All these changes are conducted by the kite control algorithm which aims to keep the tether tension between the feasible limits. This phase comes to an end when the starting position for the traction phase is reached. [25]

Traction (Reel-Out) Phase
In the traction phase the kite is made to fly in a crosswind motion, resulting in maximized traction force and mechanical power. In a real world pumping cycle, the kite is operated in figure of eight manoeuvres during the reel-out phase. For the simulation time reduction purposes as well as in an intention of keeping the model applicable for various crosswind manoeuvres, the position of the kite is different than it appears in the measurements in the current QSM.

A constant flight state is used during the whole reel-out phase in the simulation to represent the average power and the average traction force. This means the angular coordinates (θ and ϕ) and the course angle χ have constant values during the traction phase. The values for these angles are calculated using the time average of the experimental flight states. Since Equation 2.40 shows the power dependence of the cosine of these angles, according to the authors the average power could hypothetically be calculated using the time average of $\cos\theta$ (or elevation angle as $\cos\beta$) and $\cos\phi$. This could be presented as

$$\cos\phi_0 = \overline{\cos\phi} \tag{2.60}$$

and

$$\cos\beta_0 = \overline{\cos\beta}. \tag{2.61}$$

Using the average term the location of the reel-out representative point situates in the centre of one of the two figure of eight lobes. For course angle averaging the result is expected to be $\chi_0 \geq 90°$ since the kite is flying slower upwards than downwards due gravitational effect. It is worth mentioning, despite the constant angles the tether length is increased during the traction phase up to the point where r_{max} is reached. [25]

Complete Pumping Cycle
Adding the mechanical power produced or consumed in all of the three phases together, the mean mechanical power could be calculated as

$$P_m = \frac{\overline{P_o}\Delta t_o + \overline{P_i}\Delta t_i + \overline{P_x}\Delta t_x}{\Delta t_o + \Delta t_i + \Delta t_x}, \tag{2.62}$$

where o refers to traction, i to retraction and x to transition phase. The authors use the definition of power harvesting factor given in Equation 2.10 to calculate ζ for the whole pumping cycle. [25]

The QSM also has an option for varying wind conditions with altitude, making use of a logarithmic wind profile or a lookup table. However, for the validation of simulation concept itself, fixed average wind speed could be used as an input.

2.4.4. Simulations Using QSM

In 2020 Schelbergen and Schmehl wrote an article about the validation of QSM. They use a measurement set of pumping cycles provided by Kitepower B.V. and describe the wind speed reconstruction, the calculation of aerodynamic coefficients C_L & C_D and how the QSM kite velocity and power outputs relate to the measurements of the same parameters. This section provides a brief overview of their results which lay foundation for the research problem in the thesis. [19]

Wind Input
In the dataset provided by Kitepower the measured wind speed v_m is included. This parameter is received using Pitot tube attached to the kite system. The measured wind speed could be decomposed into apparent wind velocity in the measurement reference frame as

$$v_a^m = v_m \begin{bmatrix} -\cos\alpha_m \\ 0 \\ \sin\alpha_m \end{bmatrix}, \tag{2.63}$$

where α_m is the inflow angle if Pitot tube is aligned with x_m. The side slip angle in Equation 2.63 is assumed to be zero for simplicity since this parameter is not measured. However, this equation results in the apparent wind velocity in the measurement, not in the kite sensor reference frame where the orientation of the kite is given. They use a set of equations based on the geometrical properties of the kite to transform it from one into the other. Once this apparent wind velocity in the final form is known, wind velocity can be calculated with Equation 2.4 which turns into

$$\mathbf{v}_w = \mathbf{v}_a + \mathbf{v}_k, \tag{2.64}$$

where $\mathbf{v}_k$ is the velocity of the kite. This wind speed is used as an input for the QSM. [19]

Aerodynamic Coefficients
For the aerodynamic lift and drag coefficient computation they reverse the calculation process presented in Section 2.4.2. The measurements include the tether force $\mathbf{F}_t$. Based on the mass and properties of the system the force of gravity (both $\mathbf{F}_{g,k}$ for kite and $\mathbf{F}_{g,t}$ for tether) and the tether drag $\mathbf{F}_{D,t}$ could be found. This enables the aerodynamic force calculation as

$$\mathbf{F}_a = -\left(\mathbf{F}_{g,k} + \mathbf{F}_{g,t} + \mathbf{F}_{D,t} + \mathbf{F}_t\right). \tag{2.65}$$

The equation above is based on the assumption the tether force measured at the ground $\mathbf{F}_m$ has roughly the same magnitude as the aerodynamic force $\mathbf{F}_a$ and the latter is mostly responsible for the counterbalancement of the traction force. The aerodynamic coefficients C_L and C_D calculate from the aerodynamic force as

$$\begin{bmatrix} F_{a,x}^k \\ F_{a,z}^k \end{bmatrix} = \frac{1}{2}\rho {v_{a,xz}^k}^2 A \begin{bmatrix} \mathbf{e}_\perp^k & \mathbf{e}_\parallel^k \end{bmatrix} \begin{bmatrix} C_L \\ C_D \end{bmatrix}, \tag{2.66}$$

where superscript k indicates the kite sensor reference frame, $F_{a,x}^k$ and $F_{a,z}^k$ are the components of the aerodynamic force, ρ is the air density, $v_{a,xz}^k$ marks the projected apparent wind speed, A is the projected area of the kite and $\mathbf{e}_\perp^k$ & $\mathbf{e}_\parallel^k$ are the unit vectors perpendicular and parallel to the apparent wind speed vector. They use Equation 2.66 to define the aerodynamic coefficients for the QSM simulations. [19]

QSM Validation
The QSM validation is done by the authors in two parts. At first, they choose a good representative cycle for the measurement dataset. Cycle number 73 is selected here and all the QSM calculations are conducted for that cycle. Later they expand the calculations to the whole measurement set.

With Equations 2.63 and 2.64 the authors compute wind velocity for each point in data for the 73rd cycle. This is followed by aerodynamic coefficients calculations (Equation 2.66). They reach to average reel-out coefficients $C_{L,out} = 0.71$ & $C_{D,out} = 0.14$ and calculate $C_{L,in} = 0.39$ & $C_{D,in} = 0.07$ for the reel-in phase. These are also given in Table 2.2. Using the defined parameters, the system properties and the coordinates of the kite from the measurements Schelbergen and Schmehl find the tangential kite velocity $v_{k,\tau}$ output of the QSM to be in good agreement with the measurements. However, the reel-out speed relation is poor. The authors reason it with the stiff rod assumption for the tether. In reality, tether slacking and straightening motion is experienced and the direction of the tether force varies more than it occurs in the calculation. This also indicates the aerodynamic coefficients calculated using Equations 2.65 and 2.66 are probably not accurate. [19]

In expansion of the QSM calculations to the whole set of measurements they use the tuned version of aerodynamic coefficients calculated for the 73rd cycle. The authors keep the lift coefficients the same but adjust the drag coefficients in a way that the QSM with coordinates from the file would give accurate tether force for the 73rd cycle as it appears in the measurements. The new drag coefficients

Aerodynamic Coefficients for QSM Simulations		
	Reel-out	**Reel-in**
C_L	0.71	0.39
$C_{D,calc}$	0.14	0.07
$C_{D,tuned}$	0.18	0.12

Table 2.2: The aerodynamic coefficients for the QSM validation [19]

are $C_{D,out} = 0.18$ and $C_{D,in} = 0.12$. These values are exploited for all the measurement cycles. Now, the QSM uses a reel-out assumption made with Equations 2.60 and 2.61 where the azimuth-elevation pair is constant for the phase and only the radial distance changes. With the reeling-speed and tether length properties originating from the measurements they reach to the following results:

- the mean cycle duration experiences only -1.7% difference from the measurements;
- the calculated QSM mean power is deviating from the measured mean power by -26.4%.

These results indicate first that the modeling choices of the QSM need to be reassessed. This includes the assumption for time-averaging the reel-out coordinates of the kite. Additionally, the aerodynamic coefficients require tuning which means the direction of tether force is unclear with stiff rod assumption and the values found with Equation 2.66 do not reflect the reality due the misalignment of vector direction. [19]

2.4.5. Exclusion of Inertia from QSM

When realising the theory of solving the flight of the kite as series of steady-states van der Vlugt et al decided to exclude the inertial forces from the QSM (Section 2.4.3). This is in compliance with the general comparison of flexible and rigid wing in Section 2.1.2. The smaller the mass and the velocity of the kite the less impact the inertial forces have on the system. Due the current use of small flexible wings in the simulations the inertia is omitted from the calculations.

In Section 2.4.4 Schelbergen and Schmehl show the QSM mean power output is off from the measurements due the set of assumptions used. Even with the small expected impact the exclusion of inertia from the QSM has definitely a part in this power deviation. Roullier has written a thesis in 2020 where he discusses the impact of turning on the performance of the flexible kite using measurements and CFD. He claims that turning maneuvers could cause 5% decrease in the output performance of the system, explaining it with the roll of the kite. This shows from the perspective of increasing the QSM accuracy that the inertial effects should be included in the steady-state calculations. The relevance of inertial calculations increases even more when larger kites come into use in the pumping kite power system as bigger mass causes greater centrifugal force. The same goes for the expansion of QSM to rigid wings where currently the dynamic models are preferred due the longer time-scale of inertial effects. [18]

The inertial force Equations 2.44-2.50 provided by Schmehl et al are sophisticated and require knowledge about the turning speed of the kite. The latter is a parameter one could calculate knowing the tangential speed and the turning radius at the instantaneous moment. The turning radius is difficult to be estimated without any information about the next steady-state point in time series. This complication could also be a reason for the exclusion of inertial forces from the current QSM. One could overcome this problem with a known or controlled turning radius which may require testing with simplified model framework first to see how the QSM acts with the included inertial effects.

2.5. Problem Definition and Research Goals

The fundamental theory of pumping kite power system described in Section 2.4 brought up the possibility to solve a flight of a kite in series of steady-state force equilibriums. From the consecutive force balances and the respective traction power calculations, the energy production of a pumping kite system can be approximated. Accurate calculations using weather data and system parameters could

serve as a selling argument for the concept and prove the suitability of such a system to meet the demands of the electricity consumer.

Yet, the deviations in output power of the actual system and the current QSM have shown room for simulation tool improvements. This is described in Section 2.4.4. Two simplifications that may play a role in this inaccuracy of the QSM are the exclusion of inertial forces, mainly the centrifugal force, and the use of constant angles for the reel-out flight representation. The inertial forces for flexible wings are described to be small and happen in a very short time span. The time period is so small that the turning maneuvers are estimated to be irrelevant in the calculations and the flight of the kite becomes describable as series of steady-states. The constant angle logic develops this idea even further by stating the time-series of different angles the kite experiences when flying a figure of eight could be condensed to a single azimuth-elevation combination and still calculate the same time-averaged power as it appears in the measurements. The loss in power output accuracy by further distancing from describing the flight maneuvers in the simulation becomes of question. The relevance of this topic grows as the mass of the kite increases inducing bigger dynamic effects during the flight. Based on the previous train of thought the thesis has the following goal.

To improve the accuracy of QSM simulations by including more information about the turning maneuvers of the kite.

To have a structured approach for reaching the ultimate target, the thesis project is focused on the main research question, supported by various sub-questions divided into two categories. The main research question can be stated as:

How much accuracy in the QSM can be gained by including additional details on the turning maneuvers of the kite?

To respond to the main research question, two categories of sub-questions are addressed. Firstly, the impact of inertia on the flight behavior during turning maneuvers should be quantified. Secondly, improvements to the reel-out flight path representation in the QSM should be investigated. These topics are expanded by grouped sub-questions as follows:

1. How can the simulated reel-out turning maneuvers be resolved with inertial effects?
    - What information about the turning maneuvers is required to include the inertial effects in the simulations?
    - How can the inertial force equations proposed by previous authors be verified?
    - What modifications to the QSM are required to include the inertial effects in the steady-state solution?
    - How much does the accuracy of simulation improve by including inertia in the maneuvering flight of the kite?
2. Which representative reel-out flight path in the QSM simulations yields the most accurate power output?
    - How can the accuracy of QSM with alternative reel-out flight paths be quantified?
    - What is the accuracy of solving the reel-out flight path along a straight line with constant elevation and azimuth angle based on an average reel-out state of the kite?
    - What other parameterizations of reel-out figure of eight motions can be used and what impact do they have on the QSM power output accuracy?
    - Which figure of eight shape yields the maximal time-averaged power output?

3

Inertial Effects in a Modified Simulation Framework

The impact of inertial effects on soft wing kites is discussed previously in Section 2.4.5. The inertial effects are considered to be rather small on these type of wings and happen in a short timescale. This has been a reason for the exclusion of inertia from the QSM. However, as the mass of the kite increases or the QSM is expanded to a rigid wing flight the inertial effects become relevant. In this chapter the inclusion of inertial effects is investigated in a simplified simulation framework which could be expanded to a regular reel-out figure of eight in a follow-up study.

The chapter starts by setting up simulation frameworks of circular and helical flight. This is followed by an analytical development of tether force and power equations considering the inertial effects for these frameworks. The equations are presented in Cartesian coordinates. The implementation of inertial effects in spherical coordinates and in the QSM is presented in the second half of the chapter. In the end helical flight simulations are run using the QSM with inertia and the analytically developed set of equations. This is followed by a discussion of the results.

3.1. Circular and Helical Flight Frameworks

The inertial forces in the QSM and in spherical coordinate system combine a set of complex equations of motion (Equations 2.44-2.50). Furthermore, flying crosswind figure of eight maneuvers with a tethered wing introduces a new parameter of turning radius when calculating the impact of centrifugal force in the force balance of the kite. The necessity of this turning radius (R) parameter could be presented as centrifugal force equation

$$F_{i,\omega} = m\frac{v_{k,\omega}^2}{R}, \tag{3.1}$$

where m denotes the mass and $v_{k,\omega}$ the circumferential speed of the kite. This parameter R is unknown for asymmetric figures of eight. To overcome the absence of a known turning radius and to investigate the centrifugal force impact on tether force and power calculations the flight path is simplified to a helical flight with fixed R in Cartesian coordinates. This new framework is an extension of Loyd's fundamental theory of crosswind kite power with inertial effects and verifies the complex implementation of inertial forces in the context of QSM. [8]

Building a simplified flight test case starts by defining the geometric parameters. Two different flights are distinguished here: a circular flight with constant tether length and a flight on helical trajectory while tether is being reeled out. For both scenarios the tether sweeps a conical surface around axis coinciding with wind vector $\mathbf{v}_w$ and the turning radius R is kept constant throughout the simulation. The described cases can be seen in Figures 3.1 and 3.2 where the kite is shown as a point mass $\mathbf{K}$.

A new reference frame $(x_\omega, y_\omega, z_\omega)$ is introduced to describe this particular flight. It rotates around $\mathbf{v}_w$ with a constant angular speed ω. The x_ω of the new reference frame coincides with the direction of x_w of wind reference frame while the direction of z_ω is given with θ_ω from z_w according to the right hand rule when thumb is pointed in the wind direction. The parameters (x_k, y_k, z_k) define the position of the

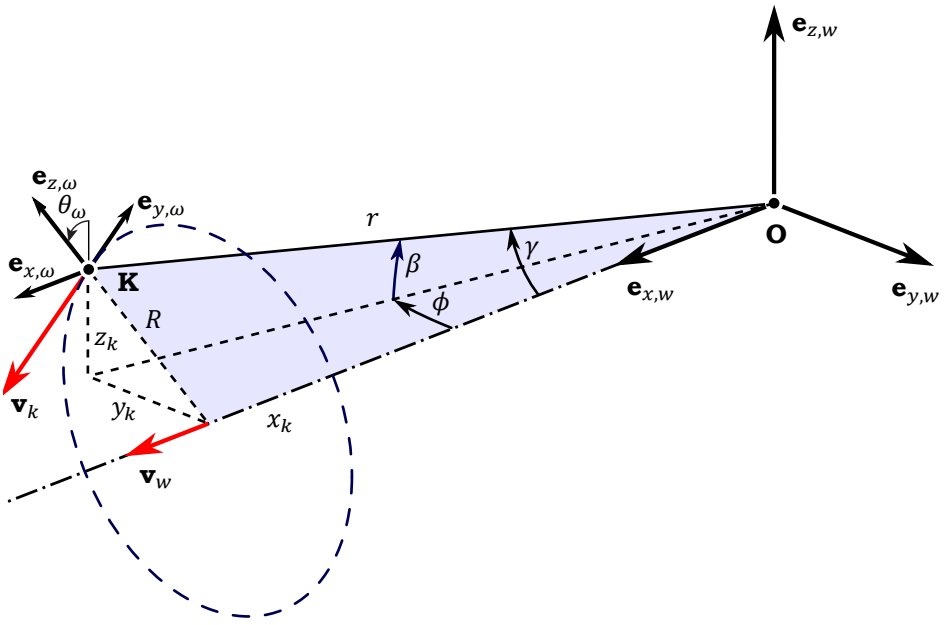

Figure 3.1: Geometric parameters of a circular flight path at constant tether length

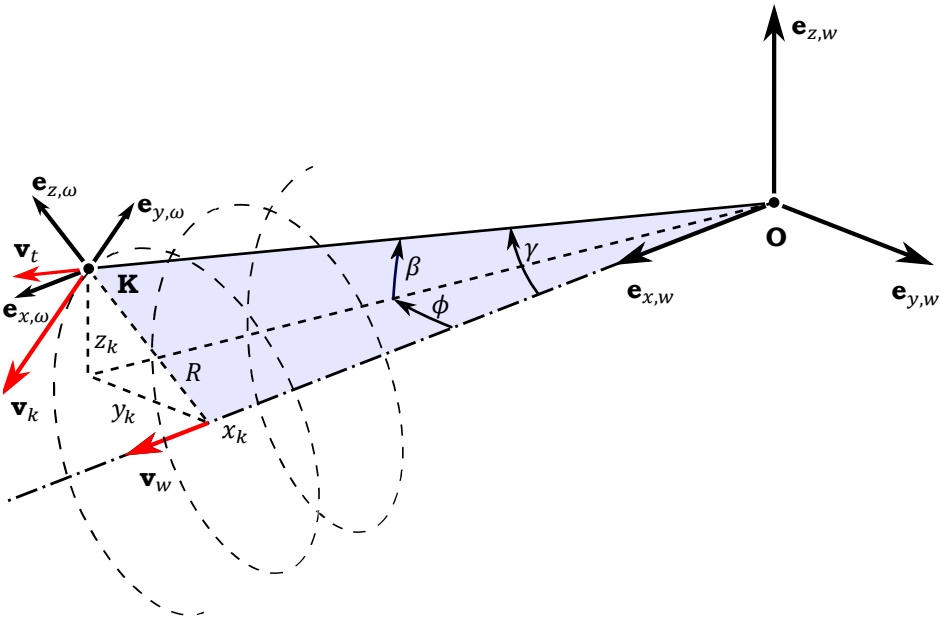

Figure 3.2: Geometric parameters of a helical trajectory flight with reeled out tether

kite in Cartesian coordinates in the wind reference frame. Using Equations 2.18 - 2.20 the values of these parameters are given as

$$x_k = r\cos\beta\cos\phi = r\cos\gamma, \tag{3.2}$$
$$y_k = r\cos\beta\sin\phi, \tag{3.3}$$
$$z_k = r\sin\beta, \tag{3.4}$$

from which the radius of the circular path or in other words the turning radius could be derived as

$$R = \sqrt{r^2 - {x_k}^2} = r\sqrt{1-\cos^2\beta\cos^2\phi} = r\sqrt{1-\cos^2\gamma}. \tag{3.5}$$

These geometrical relations and the framework of circular or helical path provide the fundamentals needed for extending the Loyd's theory in Section 3.2.

3.2. Analytical Extension of Loyd's Theory with Inertial Forces

The impact of inertial forces, especially the centrifugal force, on tether force and consequently on generated power is investigated as a free body diagram where the forces act on a point mass. For simplicity the kite is located at the highest point in z_w direction with angle $\theta_\omega = 0°$ in the following analysis. This means the kite is at the top of the circular or helical flight path and the directions of $(x_\omega, y_\omega, z_\omega)$ and (x_w, y_w, z_w) coincide. The force balance equations formulated from the free body diagram could be considered as a core for the following analytical framework. The equations are developed in two groups. First, the crosswind kite flight trajectory is a circle with constant tether length. The second group of equations are developed for the helical flight trajectory which adds the effect of reeling factor to the analysis. This part is investigated in Section 3.2.2. It is important to note only the inertial force impact is analysed in the framework without considering any gravitational effect. This simplifies the problem and makes the system changes caused by the inertial forces more perceptible.

3.2.1. Flying Perfect Downwind Circles

For this flight configuration the tether sweeps a conical surface with apex angle 2γ and both the tether length r and the turning radius R are constant. With constant γ the speed of the kite traveling the circle $v_{k,\omega}$ is equal to the tangential kite velocity $v_{k,\tau}$ known from the spherical coordinate framework. This equality is possible due the fact that both velocity vectors $(v_{k,\omega}$ & $v_{k,\tau})$ coincide with the intersection line of the kite tangential plane (perpendicular to tether in spherical coordinates) and the crosswind plane (perpendicular to wind vector). Therefore, the kite tangential velocity factor λ defined as

$$\lambda = \frac{v_{k,\tau}}{v_w} \tag{3.6}$$

and the circumferential velocity factor $\overline{\lambda}$ which one could calculate as

$$\overline{\lambda} = \frac{v_{k,\omega}}{v_w} \tag{3.7}$$

are also equal $(\lambda = \overline{\lambda})$ for this particular circular flight path. One could also substitute the tangential velocity factor or the circumferential velocity factor with a special case of lift-to-drag ratio as

$$\overline{\lambda} = \frac{v_{k,\omega}}{v_w} = \frac{L_0}{D}, \tag{3.8}$$

where L_0 is the lift force projection onto $x_\omega y_\omega$-plane. Both, the projected lift force vector $\mathbf{L}_0$ and the drag force vector $\mathbf{D}$ act also on $x_w y_w$-plane (when $\theta_\omega = 0°$ as here) in Figure 3.3. This figure is a top view diagram of the flight. The substitution in Equation 3.8 becomes possible due geometric similarity where drag force $\mathbf{D}$ is aligned with the apparent wind velocity $\mathbf{v}_a$. Equation 3.8 becomes a fundamental relation for further developing the circular flight path case.

The analysis is based on four different possibilities for γ all shown in Figure 3.4. These diagrams are the force projections on plane Π that can be seen in Figure 3.3. The particular plane Π is formed by $\mathbf{L_0}$ and the centrifugal force vector. The drag force vector $\mathbf{D}$ is perpendicular to that plane. The projection of tether force vector $\mathbf{F}_t$ onto plane Π is ($\mathbf{F}_t$ + $\mathbf{D}$) which originates from the basic principle of vector summation and the definition of projection. One needs to pay attention the sub-figures differ between γ values but the angle is not marked in the diagrams since it is measured on $x_\omega z_\omega$-plane instead as shown in Figures 3.1 and 3.2 but not on the special plane Π. The kite is pictured as a point mass (black dot) in the free body diagrams.

The sub-figure A in Figure 3.4 depicts the hypothetical flight situation developed by Luchsinger (2013) with tether aligned with wind and the centrifugal force being perpendicular to the tether. This Luchsinger flight situation is also presented in a 3D view in Figure 3.5. In his framework the tether sweeps a cylindrical path instead of conical, meaning the point where the tether is attached to follows a similar circular path as the kite itself. The lift force vector $\mathbf{L}$ is rolled towards the centre of the circle with an angle ψ_R to keep the kite in a circular movement and he develops a hypothetical minimal turning radius R_{min} the kite can fly if $\psi_R = 90°$. This R_{min} is defined as

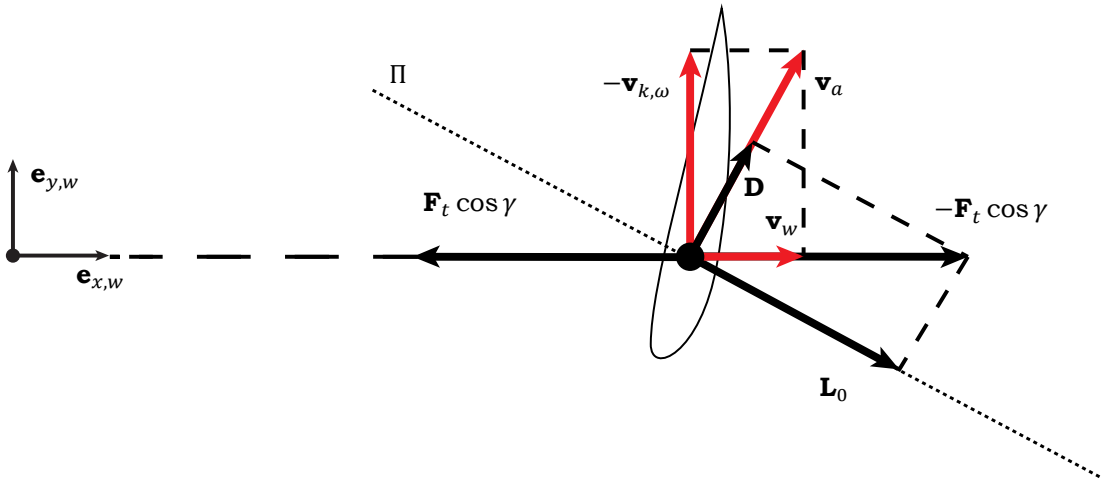

Figure 3.3: Top view of a circular flight. The kite is positioned at the highest point in z_w direction on the circular path and θ_ω = 0°. Π is a plane formed by the centrifugal force vector (pointing towards the viewer) and $\mathbf{L}_0$. That plane is perpendicular to $\mathbf{D}$.

$$R_{min} = \frac{2m}{\rho S C_L} \tag{3.9}$$

and becomes useful for nondimensionalizing the circular flight path equations in the following paragraphs. [13]

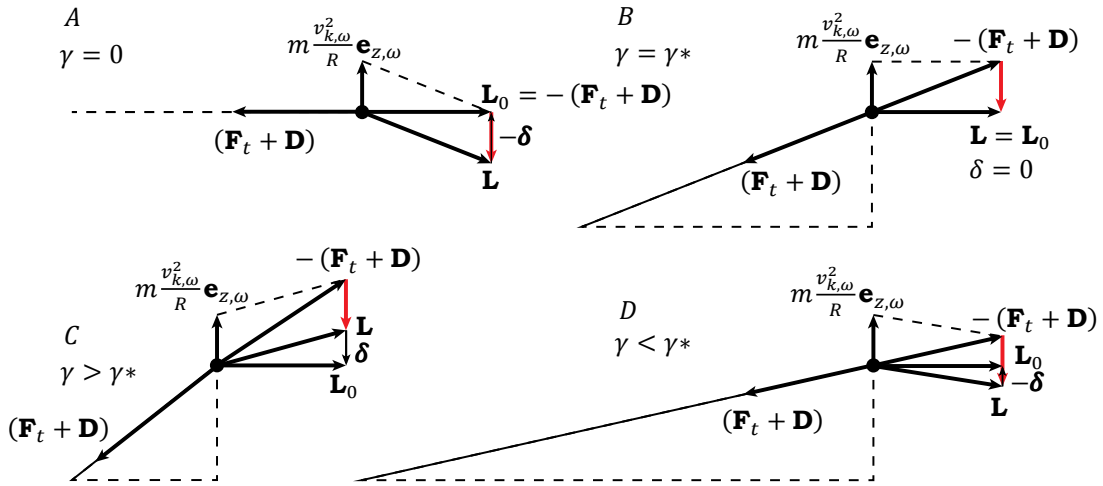

Figure 3.4: Circular flight Π-plane view. Case distinction of centrifugal force impact at different γ values.

In sub-figure B of Figure 3.4 another special case is shown where induced roll shifts $\mathbf{L}$ as much from $-(\mathbf{F}_t + \mathbf{D})$ alignment that $\mathbf{L}$ becomes equal to $\mathbf{L}_0$. That means for the case B where $\mathbf{L} = \mathbf{L}_0$ the circumferential velocity factor Equation 3.8 could be expanded to

$$\overline{\lambda} = \frac{v_{k,\omega}}{v_w} = \frac{L_0}{D} = \frac{L}{D} = E, \tag{3.10}$$

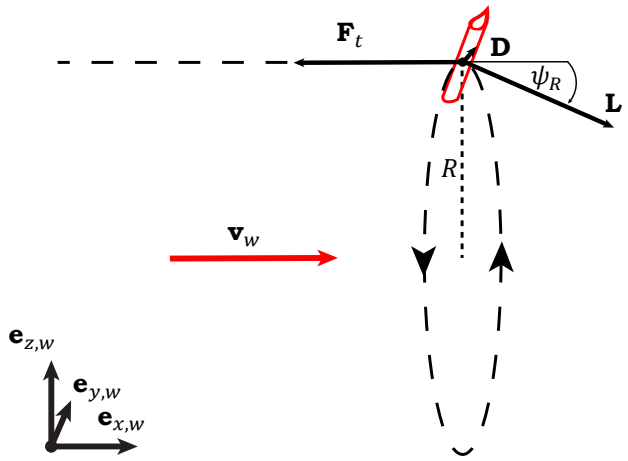

Figure 3.5: Kite flying a circle. The hypothetical case of tether aligned with wind developed by Luschsinger (2013). The kite is rolled towards the centre of the circle with an angle ψ_R. [13]

where E is a nondimensional lift-to-drag (L/D) ratio. The angle γ where this special case becomes possible is denoted as $\gamma*$. To calculate the latter a brief digression from Π-plane is required to $x_\omega z_\omega$-plane (or $x_w z_w$-plane due $\theta_\omega = 0°$) where γ is measured. The centrifugal force already acts on the plane under scope but $\mathbf{L_0}$ projection from Π to $x_w z_w$-plane becomes $\mathbf{L}_0 + \mathbf{D}$. One can observe from the top view Figure 3.3 that these $\mathbf{L}_0$ and $\mathbf{D}$ vectors form a right-angled triangle and Pythagorean theorem can be used to calculate the magnitude of that projection. On $x_w z_w$-plane the projection of the special lift force and the centrifugal force combine a new right-angled triangle and the tangent function property of opposite and adjacent side division can be used to calculate $\gamma*$ as

$$\begin{aligned}\tan\gamma^* &= \frac{m v_{k,\omega}^2}{R\sqrt{L_0^2 + D^2}} = \frac{2mE\bar{\lambda}^{-2}}{\rho S C_L R\sqrt{\left(\frac{L_0}{D}\right)^2 + 1}}\left(\frac{v_w}{v_a}\right)^2 \\ &= E\frac{R_{min}}{R}\frac{\bar{\lambda}^{-2}}{\sqrt{\bar{\lambda}^{-2} + 1}\left(\bar{\lambda}^{-2} + 1\right)^2} = \frac{R_{min}}{R}\left(\frac{E}{\sqrt{E^2 + 1}}\right)^3,\end{aligned} \tag{3.11}$$

where Equation 3.10, the definition of lift force (Equation 2.2) and R_{min} (Equation 3.9) are used together with $\left(\frac{v_w}{v_a}\right)^2$ substitution as

$$v_a^2 = v_{k,\omega}^2 + v_w^2 \tag{3.12}$$

$$\left(\frac{v_a}{v_w}\right)^2 = \bar{\lambda}^{-2} + 1. \tag{3.13}$$

The angle $\gamma*$ is necessary to distinguish between the sub-figures C and D.

Heading back to Π-plane and Figure 3.4, in the case of C the angle γ is larger than $\gamma*$, whereas for the case D it is the opposite. This distinction is necessary for the creation of force balance. Here vector $\boldsymbol{\delta}$ is used which shows the difference between $\mathbf{L}$ and $\mathbf{L}_0$ and has a positive direction pointing downwards. Vector $\boldsymbol{\delta}$ needs to be added to the centripetal force (red vector) to form a right-angled triangle together with $-(\mathbf{F}_t + \mathbf{D})$ and $\mathbf{L}_0$ in the case of C. For small angles of γ (case D) $\boldsymbol{\delta}$ changes direction by becoming $-\boldsymbol{\delta}$ and needs to be subtracted from the centripetal force for a similar right-angled triangle to be present. The centripetal force has the same magnitude as the centrifugal force. Using

case-dependent relations and the fact that the length of $-(\mathbf{F}_t + \mathbf{D})$ vector on Π-plane can be calculated with Pythagorean theorem as $F_t^2 - D^2$ the following force balances could be written

$$L_0^2 + \left(m\frac{v_{k,\omega}^2}{R} - \delta\right)^2 = F_t^2 - D^2, \text{ for } \gamma < \gamma* \tag{3.14}$$

$$L_0^2 + \left(m\frac{v_{k,\omega}^2}{R} + \delta\right)^2 = F_t^2 - D^2, \text{ for } \gamma > \gamma*. \tag{3.15}$$

In a combination with the top view diagram (Figure 3.3) additional relations using the Pythagorean theorem are defined

$$L_0^2 + \delta^2 = L^2 \tag{3.16}$$

$$L_0^2 + D^2 = F_t^2 \cos^2\gamma. \tag{3.17}$$

Combining all these four Equations 3.14-3.17 together the final force balance becomes

$$L_0^2 + \left(m\frac{v_{k,\omega}^2}{R} \pm \sqrt{L^2 - L_0^2}\right)^2 = \frac{L_0^2 + D^2}{\cos^2\gamma} - D^2. \tag{3.18}$$

Equation 3.18 is solved as

$$\begin{aligned}
L_0^2 + \left(m\frac{v_{k,\omega}^2}{R} \pm \sqrt{L^2 - L_0^2}\right)^2 &= \frac{L_0^2 + D^2}{\cos^2\gamma} - D^2 \\
\left(m\frac{v_{k,\omega}^2}{R} \pm \sqrt{L^2 - L_0^2}\right)^2 &= \frac{L_0^2 + (1 - \cos^2\gamma)D^2}{\cos^2\gamma} \\
\left(m\frac{v_{k,\omega}^2}{R} \pm \sqrt{L^2 - L_0^2}\right)^2 &= \frac{1 - \cos^2\gamma}{\cos^2\gamma}\left(L_0^2 + D^2\right) \\
\frac{mv_{k,\omega}^2}{DR} \pm \sqrt{\left(\frac{L}{D}\right)^2 - \left(\frac{L_0}{D}\right)^2} &= \frac{\sin\gamma}{\cos\gamma}\sqrt{\left(\frac{L_0}{D}\right)^2 + 1} \\
\bar{\lambda}^{-2}\frac{mv_w^2}{DR} \pm \sqrt{E^2 - \bar{\lambda}^{-2}} &= \tan\gamma\sqrt{\bar{\lambda}^{-2} + 1},
\end{aligned} \tag{3.19}$$

where Equation 3.8 (not to confuse with Equation 3.10 which is valid only for $\gamma = \gamma*$) and the nondimensial lift-to-drag ratio $E = \frac{L}{D}$ are taken of use. Using the relation where the drag force definition (Equation 2.3) and Equation 3.13 are used

$$\frac{v_w^2}{D} = \frac{v_w^2}{\frac{1}{2}\rho S C_D v_a^2} = \frac{2}{\rho S C_D\left(\bar{\lambda}^{-2} + 1\right)} = \frac{2E}{\rho S C_L\left(\bar{\lambda}^{-2} + 1\right)}, \tag{3.20}$$

the force balance Equation 3.19 becomes

$$\frac{\bar{\lambda}^{-2}}{\bar{\lambda}^{-2} + 1}\frac{2mE}{\rho S C_L R} \pm \sqrt{E^2 - \bar{\lambda}^{-2}} = \tan\gamma\sqrt{\bar{\lambda}^{-2} + 1}. \tag{3.21}$$

With the definition of R_{min} (Equation 3.9) this can also be written as

$$\begin{aligned}\frac{\bar{\lambda}^2}{\left(1+\bar{\lambda}^2\right)^{\frac{3}{2}}}E\frac{2m}{\rho SC_L}\frac{1}{R}\pm\left(\frac{E^2-\bar{\lambda}^2}{1+\bar{\lambda}^2}\right)^{\frac{1}{2}}&=\tan\gamma\\ \frac{\bar{\lambda}^2}{\left(1+\bar{\lambda}^2\right)^{\frac{3}{2}}}E\frac{R_{min}}{R}\pm\left(\frac{E^2-\bar{\lambda}^2}{1+\bar{\lambda}^2}\right)^{\frac{1}{2}}&=\tan\gamma.\end{aligned} \tag{3.22}$$

Equation 3.22 could be considered as the final nondimensional form of a circular flight force balance and can be used to find $\bar{\lambda}$ through iterations at given E, R, R_{min} and γ. With further approximations about the flight framework one could simplify the Equation 3.22 to eliminate the iterative technique from the solution process. These approximations are investigated in Section 3.2.3.

Once the circumferential velocity factor becomes a known variable for the circular flight simulation, tether force could be calculated. But developing an equation for the tether force requires first some modification to the drag force definition (Equation 2.3) which makes the usage of Equation 3.13 later possible. The drag force becomes

$$D=\frac{1}{2}\rho SC_D v_a^2=\frac{1}{2}\rho S\frac{C_L}{E}v_w^2\left(\frac{v_a}{v_w}\right)^2, \tag{3.23}$$

where lift-to-drag ratio as $E=\frac{C_L}{C_D}$ is implemented. With Equations 3.23 and 3.17, the latter being taken directly from the top view diagram of Figure 3.3, the step-by-step buildup of the tether force equation could be written as

$$\begin{aligned}F_t&=\frac{\sqrt{L_0^2+D^2}}{\cos\gamma}=\frac{D}{\cos\gamma}\sqrt{\left(\frac{L_0}{D}\right)^2+1}=\frac{1}{\cos\gamma}\frac{\rho SC_L}{2E}v_w^2\left(\frac{v_a}{v_w}\right)^2\sqrt{\bar{\lambda}^2+1}\\ &=\frac{1}{\cos\gamma}\frac{\rho SC_L}{2E}v_w^2\left(\bar{\lambda}^2+1\right)\sqrt{\bar{\lambda}^2+1}=\frac{1}{\cos\gamma}\frac{\rho SC_L}{2E}v_w^2\left(\bar{\lambda}^2+1\right)^{\frac{3}{2}}.\end{aligned} \tag{3.24}$$

By substituting some of the parameters with the dynamic wind pressure

$$q=\frac{1}{2}\rho v_w^2 \tag{3.25}$$

the non-dimensional form of the tether force becomes

$$\frac{F_t}{qS}=\frac{C_L}{E\cos\gamma}\left(\bar{\lambda}^2+1\right)^{\frac{3}{2}}. \tag{3.26}$$

Since the power generation requires tether to be reeled out and this is not the case for the simple circular flight the particular framework is just limited to tether force. The power equations are presented in the following section describing the helical flight.

3.2.2. Flying Downwind Helical Trajectory

In this flight configuration the tether sweeps a conical surface around the wind vector $\mathbf{v}_w$ and R is kept constant similarly to the circular flight situation with the exception the tether is now reeled out. This leads to a helical flight trajectory and changing angle γ. For simplicity the speed in downwind direction $v_{k,x}$ is kept constant. The latter is a new parameter which could be calculated with

$$v_{k,x}=f_x v_w, \tag{3.27}$$

where f_x is a constant non-dimensional downwind speed (not to confuse with the reeling factor f). However, $v_{k,x}$ is not the only new velocity component in this helical trajectory path. A small velocity

vector is also induced by the changing γ value in this type of flight. This is supported by the reel-out speed of the tether. The relation between these three new velocities is shown in Figure 3.6 which is now the side view of the flight and not showing Π-plane. For simplicity the kite is still positioned at the top of the flight path ($\theta_\omega = 0°$) and the directions of (x_w, y_w, z_w) and $(x_\omega, y_\omega, z_\omega)$ coincide, meaning the three velocities act on both $x_w z_w$-plane and $x_\omega z_\omega$-plane in this diagram.

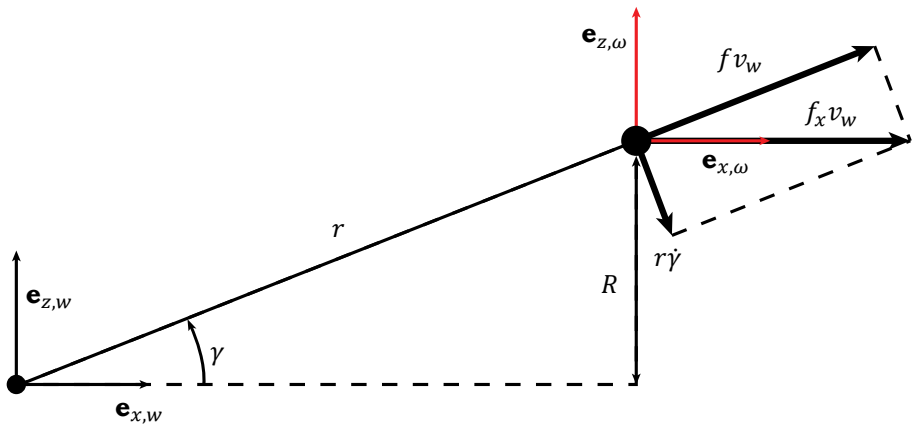

Figure 3.6: Helical flight side view with tether reeling out, decreasing γ and constant R

Based on Figure 3.6 one could write $v_{k,x}$ using the Pythagorean theorem as

$$v_{k,x}^2 = (fv_w)^2 + (r\dot{\gamma})^2. \tag{3.28}$$

To keep the R constant the velocity in z_ω (and here as well in z_w) direction needs to be zero. The velocity in downwind direction is perpendicular to z_ω and does not have any impact on it. The same goes for the circumferential velocity $v_{k,\omega}$. Using the other velocity components the following relation becomes present

$$\begin{aligned} v_{k,z} = 0 &= fv_w \sin\gamma + r\dot{\gamma}\cos\gamma \\ 0 &= fv_w \tan\gamma + r\dot{\gamma} \\ r\dot{\gamma} &= -fv_w \tan\gamma \\ \dot{\gamma} &= -f\frac{v_w}{r}\tan\gamma. \end{aligned} \tag{3.29}$$

With Equations 3.28 and 3.29 a connection between the non-dimensional downwind speed f_x and the reeling factor f could be drawn as

$$\begin{aligned} v_{k,x}^2 &= (fv_w)^2 + (fv_w)^2 \tan^2\gamma \\ v_{k,x}^2 &= (1+\tan^2\gamma)(fv_w)^2 \\ v_{k,x} &= \sqrt{1+\tan^2\gamma}(fv_w) \\ v_{k,x} &= \frac{f}{\cos\gamma}v_w, \end{aligned} \tag{3.30}$$

where

$$f_x = \frac{f}{\cos\gamma}. \tag{3.31}$$

In the helical trajectory flight with additional velocity components Equations 3.8, 3.12 and 3.13 do not hold anymore. Therefore, to expand the force balance equations in the helical flight these relations need

to be redefined. With $v_{k,x}$ acting in the direction of wind and using Equation 3.31 the circumferential velocity factor $\bar{\lambda}$ could be written as

$$\begin{aligned} \frac{v_{k,\omega}}{v_w - v_{k,x}} &= \frac{L_0}{D} \\ v_{k,\omega} &= \frac{L_0}{D}(v_w - v_{k,x}) \\ \bar{\lambda} &= \frac{L_0}{D}\left(1 - \frac{v_{k,x}}{v_w}\right) \\ \bar{\lambda} &= \frac{L_0}{D}\,(1 - f_x)\,. \end{aligned} \tag{3.32}$$

The Equations 3.12 and 3.13 become

$$v_a^2 = v_{k,\omega}^2 + (v_w - v_{k,x})^2 \tag{3.33}$$

$$\left(\frac{v_a}{v_w}\right)^2 = \bar{\lambda}^2 + (1 - f_x)^2. \tag{3.34}$$

These Equations 3.32 and 3.34 together with the definitions of R_{min} (Equation 3.9) and lift (Equation 2.2) could be used in the force balance Equation 3.19 to adjust for the helical flight trajectory in the following way:

$$\begin{aligned} \frac{m v_{k,\omega}^2}{DR} \pm \sqrt{\left(\frac{L}{D}\right)^2 - \left(\frac{L_0}{D}\right)^2} &= \tan\gamma \sqrt{\left(\frac{L_0}{D}\right)^2 + 1} \\ \bar{\lambda}^2 \frac{m v_w^2}{DR} \pm \sqrt{E^2 - \left(\frac{\bar{\lambda}}{1 - f_x}\right)^2} &= \tan\gamma \sqrt{\left(\frac{\bar{\lambda}}{1 - f_x}\right)^2 + 1} \\ \bar{\lambda}^2 E \frac{2m}{\rho S C_L} \frac{1}{R} \left(\frac{v_w}{v_a}\right)^2 \pm \sqrt{E^2 - \left(\frac{\bar{\lambda}}{1 - f_x}\right)^2} &= \tan\gamma \sqrt{\left(\frac{\bar{\lambda}}{1 - f_x}\right)^2 + 1} \\ \frac{\bar{\lambda}^2}{\bar{\lambda}^2 + (1 - f_x)^2} E \frac{R_{min}}{R} \pm \sqrt{E^2 - \bar{\lambda}^2 \left(\frac{1}{1 - f_x}\right)^2} &= \tan\gamma \sqrt{\bar{\lambda}^2 \left(\frac{1}{1 - f_x}\right)^2 + 1}. \end{aligned} \tag{3.35}$$

Equation 3.35 describes the force balance of the kite flying helical trajectory and could be used to iteratively solve for the circumferential velocity factor $\bar{\lambda}$. However, this equation can be simplified further by introducing another non-dimensional parameter μ which is a relation of $\bar{\lambda}$ and f_x:

$$\mu = \frac{\bar{\lambda}}{1 - f_x}. \tag{3.36}$$

With μ Equation 3.35 becomes

$$\begin{aligned} \frac{1}{1 + \left(\frac{1 - f_x}{\bar{\lambda}}\right)^2} E \frac{R_{min}}{R} \pm \sqrt{E^2 - \left(\frac{\bar{\lambda}}{1 - f_x}\right)^2} &= \tan\gamma \sqrt{\left(\frac{\bar{\lambda}}{1 - f_x}\right)^2 + 1} \\ \frac{\mu^2}{\mu^2 + 1} E \frac{R_{min}}{R} \pm \sqrt{E^2 - \mu^2} &= \tan\gamma \sqrt{\mu^2 + 1}, \end{aligned} \tag{3.37}$$

which is the final non-dimensional form of the force balance. For $\gamma < \gamma*$ one uses negative sign in front of the left hand side square root and for $\gamma > \gamma*$ the positive sign becomes relevant. Equation 3.37 will be used in Section 3.4 for a iterative solution example in the helical trajectory flight.

The tether force equation for this framework is developed similarly to the circular flight. The difference originates from $\frac{L_0}{D}$ and $\left(\frac{v_a}{v_w}\right)^2$ which according to Equations 3.32 and 3.34 have an additional component of f_x. Using Equations 3.23 and 3.17 the tether force can be written as

$$\begin{aligned} F_t &= \frac{\sqrt{L_0^2 + D}}{\cos\gamma} = \frac{D}{\cos\gamma}\sqrt{\left(\frac{L_0}{D}\right)^2 + 1} = \frac{1}{\cos\gamma}\frac{\rho S C_L}{2E} v_w^2 \left(\frac{v_a}{v_w}\right)^2 \sqrt{\left(\frac{L_0}{D}\right)^2 + 1} \\ &= \frac{1}{\cos\gamma}\frac{\rho S C_L}{2E} v_w^2 \left[\bar{\lambda}^{-2} + (1 - f_x)^2\right] \sqrt{\left(\frac{\bar{\lambda}}{1 - f_x}\right)^2 + 1} \\ &= \frac{1}{\cos\gamma}\frac{\rho S C_L}{2E} v_w^2 \left[\bar{\lambda}^{-2} + (1 - f_x)^2\right] \sqrt{\frac{1}{(1 - f_x)^2}\left[\bar{\lambda}^{-2} + (1 - f_x)^2\right]} \\ &= \frac{1}{(1 - f_x)\cos\gamma}\frac{\rho S C_L}{2E} v_w^2 \left[\bar{\lambda}^{-2} + (1 - f_x)^2\right]^{\frac{3}{2}}. \end{aligned} \tag{3.38}$$

With Equation 3.25 the non-dimensional form of the tether force for the helical flight is

$$\frac{F_t}{qS} = \frac{1}{(1 - f_x)\cos\gamma}\frac{C_L}{E}\left[\bar{\lambda}^{-2} + (1 - f_x)^2\right]^{\frac{3}{2}}. \tag{3.39}$$

The power generation with the kite flying helical trajectory becomes possible since tether experiences reel-out velocity v_t. This velocity given by $f v_w$ is changing with the angle γ to keep the constant speed $v_{k,x}$ in the downwind direction. The power is calculated as a multiplication of this tether velocity v_t and the tether force F_t. With the help of Equations 3.38 and 3.31 the power equation is expanded as

$$\begin{aligned} P &= F_t v_t \\ &= \frac{1}{(1 - f_x)\cos\gamma}\frac{\rho S C_L}{2E} v_w^2 \left[\bar{\lambda}^{-2} + (1 - f_x)^2\right]^{\frac{3}{2}} f v_w \\ &= \frac{f}{(1 - f_x)\cos\gamma}\frac{\rho S C_L}{2E} v_w^3 \left[\bar{\lambda}^{-2} + (1 - f_x)^2\right]^{\frac{3}{2}} \\ &= \frac{f_x}{(1 - f_x)}\frac{\rho S C_L}{2E} v_w^3 \left[\bar{\lambda}^{-2} + (1 - f_x)^2\right]^{\frac{3}{2}}. \end{aligned} \tag{3.40}$$

The power density in wind is computable with

$$P_w = \frac{1}{2}\rho v_w^3 \tag{3.41}$$

and by using that equation one can give a non-dimensional fraction of power being harvested with the given kite setup and flight trajectory. This finalized power equation is

$$\zeta = \frac{P}{P_w S} = \frac{f_x}{1 - f_x}\frac{C_L}{E}\left[\bar{\lambda}^{-2} + (1 - f_x)^2\right]^{\frac{3}{2}}. \tag{3.42}$$

3.2.3. Approximations for Analytical Simplifications

Section 3.2 extended Loyd's fundamental flight theory with centrifugal acceleration and Equations 3.21 and 3.37 were developed for finding $\bar{\lambda}$ and μ using the iterative process. These values could be used

for the non-dimensional tether force calculations in Equations 3.26 and 3.39 and for the helical flight power estimation in Equation 3.42. However, with further approximations for special cases of flight one could remove the iterative technique from the solution finding process, making it much simpler. Additionally, some of these approximations could tie the non-dimensional power Equation 3.42 to theory developed by Luchsinger (2013) where tether is always aligned with wind (shown in Figure 3.5). The approximations are presented in two groups: first for the circular flight and then followed by the flight on helical trajectory.

Approximations for Circular Downwind Flight
The first approximation is made for the fast-flying kites on the circular path. This means the circumferential kite velocity is much larger than the kite-experienced wind velocity: $v_{k,\omega} \gg v_w$. That leads to

$$v_a \approx v_{k,\omega} \tag{3.43}$$

$$\overline{\lambda} \gg 1 \text{ and } \overline{\lambda}^2 + 1 \approx \overline{\lambda}^2. \tag{3.44}$$

Equation 3.21 could be written with these simplifications as

$$\frac{ER_{min}}{R} \pm \sqrt{E^2 - \overline{\lambda}^2} = \overline{\lambda} \tan\gamma. \tag{3.45}$$

By defining terms a and b

$$a = \frac{ER_{min}}{R} \tag{3.46}$$

$$b = \tan\gamma \tag{3.47}$$

the equation becomes

$$a - b\overline{\lambda} \pm \sqrt{E^2 - \overline{\lambda}^2} = 0. \tag{3.48}$$

Equation 3.48 is a quadratic equation and could be solved analytically. To keep the solution mathematically feasible $E \geq \overline{\lambda}$ all the time. The maximum $\overline{\lambda}_{max} = E$ is also Loyd's solution for $f = 0$.

The second approximation goes for aligning tether with wind. This gets closer to the theoretical solution provided by Luchsinger. When $\gamma = 0$ the following relations are present

$$\tan\gamma = 0 \tag{3.49}$$

$$\gamma < \gamma*, \text{ only "-" used in the force balance.} \tag{3.50}$$

Equation 3.45 reduces further to

$$\begin{aligned} &\frac{ER_{min}}{E} - \sqrt{E^2 - \overline{\lambda}^2} = 0 \\ &E^2 - \overline{\lambda}^2 = \left(\frac{ER_{min}}{R}\right)^2 \\ &\overline{\lambda}^2 = E^2\left[1 - \left(\frac{R_{min}}{R}\right)^2\right] \\ &\overline{\lambda} = E\sqrt{1 - \left(\frac{R_{min}}{R}\right)^2}, \end{aligned} \tag{3.51}$$

which provides a solution for $\overline{\lambda}$ without the use of any quadratic equation solving techniques.

Approximations for Helical Downwind Flight

The first approximation in helical downwind flight is similarly to circular flight made for the fast-flying kites. If μ is considered to be $\mu \gg 1$ then Equation 3.37 could be written as

$$E\frac{R_{min}}{R} \pm \sqrt{E^2-\mu^2} = \mu \tan\gamma. \tag{3.52}$$

This means $E \geq \mu$ for a real solution and consequently from the definition of μ (Equation 3.36)

$$E \geq \frac{\overline{\lambda}}{1-f_x}. \tag{3.53}$$

If $f_x = 0$ and the kite flies circles then $\overline{\lambda}_{max} = E$. For any $f_x > 0$ the value of $\overline{\lambda}_{max} = E(1-f_x)$.

The second approximation aligns tether with wind, meaning Assumptions 3.49 and 3.50 are valid again. This makes Equation 3.52 into

$$\begin{aligned}
E\frac{R_{min}}{R} - \sqrt{E^2-\mu^2} &= 0 \\
E^2-\mu^2 &= E^2\left(\frac{R_{min}}{R}\right)^2 \\
\mu^2 &= E^2\left[1-\left(\frac{R_{min}}{R}\right)^2\right] \\
\mu &= E\sqrt{1-\left(\frac{R_{min}}{R}\right)^2} \\
\frac{\overline{\lambda}}{1-f} &= E\sqrt{1-\left(\frac{R_{min}}{R}\right)^2} \\
\overline{\lambda} &= E(1-f)\sqrt{1-\left(\frac{R_{min}}{R}\right)^2}.
\end{aligned} \tag{3.54}$$

By using the non-dimensional power Equation 3.42, the newly defined Equation 3.54 for $\overline{\lambda}$, the assumption of fast flying kite $\overline{\lambda} \gg 1-f_x$ and tether being aligned with wind $f = f_x$ one could find similar power equation to Luchsinger:

$$\begin{aligned}
\frac{P}{P_w S} &= \overline{\lambda}^3 \frac{f}{1-f}\frac{C_L}{E} \\
&= E^3(1-f)^3\left[1-\left(\frac{R_{min}}{R}\right)^2\right]^{\frac{3}{2}} \frac{f}{1-f}\frac{C_L}{E} \\
&= C_L E^2 f(1-f)^2\left[1-\left(\frac{R_{min}}{R}\right)^2\right]^{\frac{3}{2}}.
\end{aligned} \tag{3.55}$$

Using optimal reeling factor $f = \frac{1}{3}$ the equation becomes

$$\frac{P}{P_w S}_{opt} = \frac{4}{27}C_L E^2\left[1-\left(\frac{R_{min}}{R}\right)^2\right]^{\frac{3}{2}}, \tag{3.56}$$

which corresponds to Luchsinger (2013) Equation 3.53 from [13]. This also verifies the theory and the assumptions made in the analytical framework so far.

3.3. Inertial Forces in QSM

The previous Section 3.2 developed analytically the equations for including the inertial force impact in the steady-states of the kite. The circular or helical flight framework was given in Cartesian coordinates. In the QSM, however, the centrifugal acceleration and the other inertial forces act in the spherical coordinates. In this coordinate system the inertial forces are given with Equation 2.44. The kite velocity is decomposed into three components in Equations 2.45-2.47. These are the projections of $\mathbf{v}_k$ in three directions: (r, θ, ϕ). The corresponding accelerations in Equations 2.49 and 2.50 are the time-derivatives of $\dot{\theta}$ and $\dot{\phi}$. Considering that the time-derivatives of the tangential kite velocity $v_{k,\tau}$ and the radial kite velocity $v_{k,r}$ are small due steady-state simulation, meaning

$$\dot{v}_{k_\tau} \approx 0 \tag{3.57}$$

$$\dot{v}_{k,r} \approx 0, \tag{3.58}$$

one could find the accelerations in $\mathbf{e}_\theta$ and $\mathbf{e}_\phi$ directions in the following way:

$$\begin{aligned}\ddot{\theta} &= \frac{d\dot{\theta}}{dt} = \frac{d}{dt}\left(\frac{v_{k,\tau}}{r}\cos\chi\right) = \frac{-\dot{r}v_{k,\tau}\cos\chi + r\left(\dot{v}_{k,\tau}\cos\chi - v_{k,\tau}\dot{\chi}\sin\chi\right)}{r^2} \\ &= \frac{-\dot{r}v_{k,\tau}\cos\chi - rv_{k,\tau}\dot{\chi}\sin\chi}{r^2} = -\frac{\dot{r}v_{k,\tau}\cos\chi}{r^2} - \frac{rv_{k,\tau}\dot{\chi}\sin\chi}{r^2} \\ &= -\frac{v_{k,\tau}\cos\chi}{r}\left(\frac{\dot{r}}{r} + \dot{\chi}\tan\chi\right) = -\frac{\lambda v_w}{r}\cos\chi\left(\frac{\dot{r}}{r} + \dot{\chi}\tan\chi\right) = -\dot{\theta}\left(\frac{\dot{r}}{r} + \dot{\chi}\tan\chi\right)\end{aligned} \tag{3.59}$$

and

$$\begin{aligned}\ddot{\phi} &= \frac{d\dot{\phi}}{dt} = \frac{d}{dt}\left(\frac{v_{k,\tau}}{r}\frac{\sin\chi}{\sin\theta}\right) \\ &= \frac{-v_{k,\tau}\sin\chi(\dot{r}\sin\theta + r\dot{\theta}\cos\theta) + r\sin\theta(\dot{v}_{k,\tau}\sin\chi + v_{k,\tau}\dot{\chi}\cos\chi)}{r^2\sin^2\theta} \\ &= \frac{-\dot{r}v_{k,\tau}\sin\theta\sin\chi - rv_{k,\tau}\dot{\theta}\sin\chi\cos\theta + rv_{k,\tau}\dot{\chi}\sin\theta\cos\chi}{r^2\sin^2\theta} \\ &= -\frac{\dot{r}v_{k,\tau}\sin\chi}{r^2\sin\theta} + \frac{v_{k,\tau}\dot{\chi}\cos\chi}{r\sin\theta} - \frac{v_{k,\tau}\dot{\theta}\sin\chi\cos\theta}{r\sin^2\theta} = -\frac{v_{k,\tau}}{r}\frac{\sin\chi}{\sin\theta}\left(\frac{\dot{r}}{r} - \dot{\chi}\frac{1}{\tan\chi} + \dot{\theta}\frac{1}{\tan\theta}\right) \\ &= -\frac{\lambda v_w}{r}\frac{\sin\chi}{\sin\theta}\left(\frac{\dot{r}}{r} - \dot{\chi}\frac{1}{\tan\chi} + \dot{\theta}\frac{1}{\tan\theta}\right) = -\dot{\phi}\left(\frac{\dot{r}}{r} - \dot{\chi}\frac{1}{\tan\chi} + \dot{\theta}\frac{1}{\tan\theta}\right).\end{aligned} \tag{3.60}$$

The Equations 3.59 and 3.60 are equal to Equations 2.49 and 2.50, respectively, which are provided by Schmehl et al.

It can be observed from the spherical coordinate inertial equations and the steady-state model description presented in Section 2.4 that all the other parameters except $\dot{\chi}$ are already used in the QSM iterative algorithm. This single undefined variable $\dot{\chi}$, named course rate, shows at what speed the kite tangential velocity $v_{k,\tau}$ changes its direction on the tangential plane. The course rate has a similar purpose to the angular velocity ω acting on the crosswind plane in the circular/helical flight. The positive direction for both ω and $\dot{\chi}$ is defined with the right-hand rule when thumb is pointing in the direction of wind. This is symbolized in Figures 3.7 and 3.8 where the connection between the crosswind and the kite tangential plane in circular/helical flight framework is shown. In circular flight the velocity component caused by the changing γ value is nonexistent since the tether is not reeled out and γ is kept constant.

In order to perform the force balance calculations in the circular or helical flight case with the QSM it is essential to first link the positional arguments of the kite between the Cartesian and the spherical coordinates. With Equations 2.18-2.20 (r, θ, ϕ) values could be acquired. For course angle χ and θ_ω the connection becomes much more difficult since it is dependent on the direction of the circular movement. Additionally, these angles are measured on different planes: χ on tangential plane τ (perpendicular to

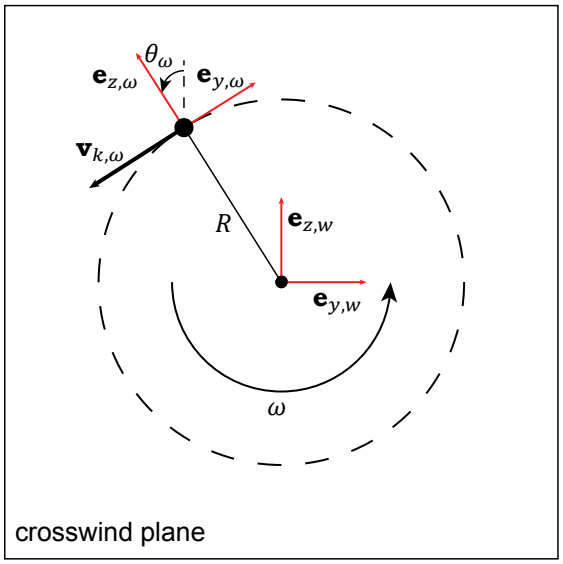

Figure 3.7: Crosswind plane in helical flight. Looking into upwind direction ($\mathbf{e}_{x,w}$ pointing towards the viewer).

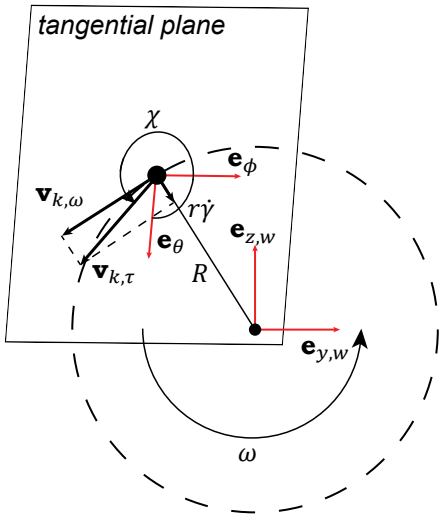

Figure 3.8: Tangential plane in helical flight. Looking into upwind direction ($\mathbf{e}_{x,w}$ pointing towards the viewer).

tether) and θ_ω on crosswind plane C (perpendicular to wind). As the kite rotates the angles between these two planes change. The following provides a description on how to link θ_ω and χ. After that equations for course rate $\dot{\chi}$ are presented.

The course angle χ is measured on τ plane from the positive direction of $\mathbf{e}_\theta$ to vector $\mathbf{v}_{k,\tau}$. The angle θ_ω shows the directional difference between the wind reference frame unit vector $\mathbf{e}_{z,w}$ and the kite reference frame vector $\mathbf{e}_{z,\omega}$ on plane C. The connection between the two angles in scope has four components and their required projections from one plane to another. These start from the vector $\mathbf{e}_\theta$ and end with $\mathbf{v}_{k,\tau}$ which give the value for χ. The four steps are presented in form of a list and followed by a longer description of each element.

- Find the measured angle from $\mathbf{e}_\theta$ to the projection of $\mathbf{e}_{z,w}$ on plane τ.
- Investigate the change in angle θ_ω when the latter is projected onto τ and becomes $\theta_{\omega,\tau}$. This defines the angles between the projected $\mathbf{e}_{z,w}$ and $\mathbf{e}_{z,\omega}$.
- Look how the angle measured from $\mathbf{e}_{z,\omega}$ to $\mathbf{v}_{k,\omega}$ may change due C-τ projection.
- Geometrically acquire the angular difference between $\mathbf{v}_{k,\omega}$ and $\mathbf{v}_{k,\tau}$ that could be observed from Figure 3.8.

The vector $\mathbf{e}_\theta$ shows the direction of elevation/inclination change in spherical coordinates and is pointing downwards on plane τ. In Cartesian coordinates z_w has somewhat similar purpose with a difference the unit vector $\mathbf{e}_{z,w}$ is pointing in the increasing direction of elevation. Figure 3.9 shows that the vector $\mathbf{e}_{z,w}$ can be projected onto tangential plane with the elevation angle β. The projection on τ becomes $\mathbf{e}_{z,w}\cos\beta$ and aligns with $\mathbf{e}_\theta$ but in the opposite direction. Hence, the difference between the two vectors, $\mathbf{e}_{z,w}\cos\beta$ and $\mathbf{e}_\theta$, is π.

To investigate the change of θ_ω, when the latter is projected onto tangential plane as $\theta_{\omega,\tau}$, an additional projection of vector $\mathbf{e}_{z,\omega}$ is required. Since this vector acts on the same plane where angle γ is measured on, the projection becomes $\mathbf{e}_{z,\omega}\cos\gamma$. As one could see from Figure 3.9 the vectors $\mathbf{e}_{z,w}$ and $\mathbf{e}_{z,\omega}$ and their projections on plane τ formulate an oblique pyramid. This geometric shape could be used to define the angle $\theta_{\omega,\tau}$ between $\mathbf{e}_{z,w}\cos\beta$ and $\mathbf{e}_{z,\omega}\cos\gamma$.

Figure 3.10 shows the base of the formed pyramid. One needs to calculate the edge x which is necessary for the triangle plotted in Figure 3.11. The latter is the lateral face of the pyramid on tangential

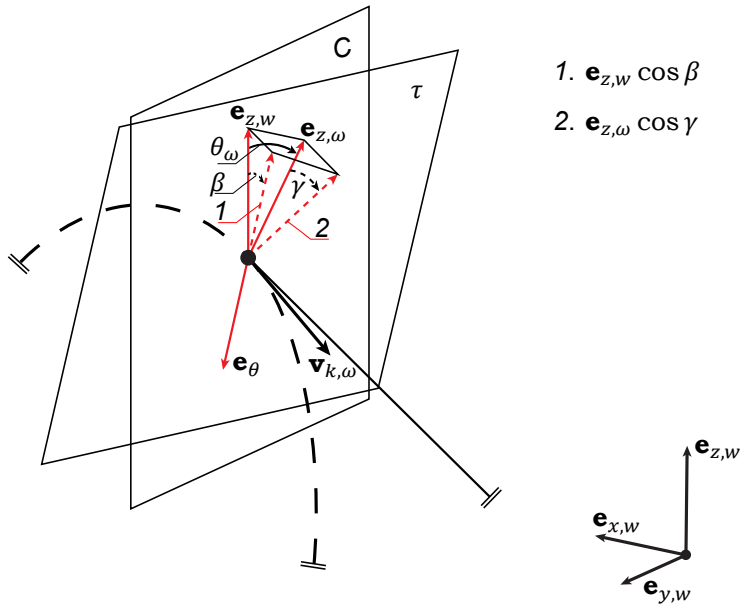

Figure 3.9: Intersection of crosswind plane C and tangential plane τ. Vectors with solid lines act on the original planes: $\mathbf{e}_{z,w}$ and $\mathbf{e}_{z,\omega}$ on plane C and $\mathbf{e}_\theta$ on plane τ. The vectors with dashed lines indicate the projections of unit vectors from crosswind C to tangential plane τ. Together with the original vectors they form a pyramid.

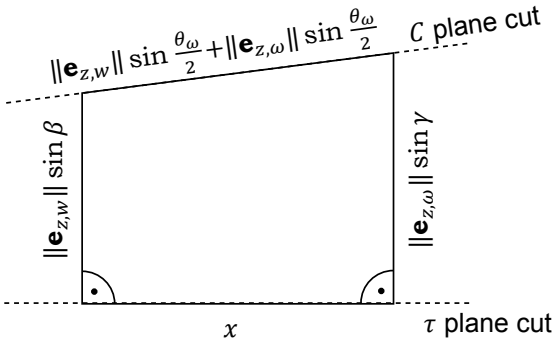

Figure 3.10: Base of the pyramid formed by vectors $\mathbf{e}_{z,w}$ and $\mathbf{e}_{z,\omega}$ and their projections $\mathbf{e}_{z,w} \cos\beta$ and $\mathbf{e}_{z,\omega} \cos\gamma$ onto tangential plane τ

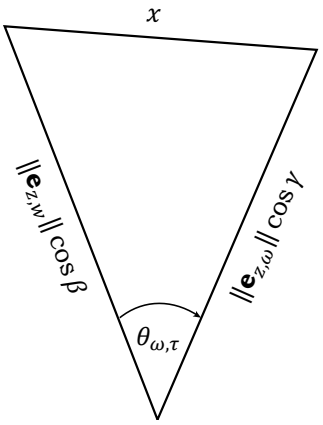

Figure 3.11: Lateral face of the pyramid shown in Figure 3.9. This triangle has the projection of θ_ω onto tangential plane: $\theta_{\omega,\tau}$.

plane and has $\theta_{\omega,\tau}$ as apex angle. The edges of the base (Figure 3.10) can be calculated with the projections of unit vectors. Here the vector notation is dropped and the edges are given as scalar values. From the same angles β and γ one could find two sides for the base by using trigonometric functions. The side that acts on plane C is also the base for isosceles triangle formed by $\mathbf{e}_{z,w}$, $\mathbf{e}_{z,\omega}$ and the angle θ_ω between them. The property that the unit vectors are the same length and the height of the triangle splits angle θ_ω into two is taken of use. Two right-handed triangles each with a side of $\sin\frac{\theta_\omega}{2}$ are formed. The sides are summed together to find the third edge for the base of the pyramid. Since the unit vectors $\mathbf{e}$ have a scalar value of 1, the missing side x is simply calculable with the Pythagorean theorem as

$$x = \sqrt{\left(2\sin\frac{\theta_\omega}{2}\right)^2 - (\sin\gamma - \sin\beta)^2}. \tag{3.61}$$

Now all the sides of the triangle shown in Figure 3.11 are known and one cold calculate the value

of $\theta_{\omega,\tau}$ by using

$$A = \arccos\left(\frac{b^2 + c^2 - a^2}{2bc}\right), \tag{3.62}$$

where A denotes the angle (here $\theta_{\omega,\tau}$) and $a,\ b,\ c$ are the sides, a being opposite to A. [2] From this formula the value for $\theta_{\omega,\tau}$ becomes

$$\theta_{\omega,\tau} = \arccos\left(\frac{1 - 2\sin^2\frac{\theta_\omega}{2} - \sin\beta\sin\gamma}{\cos\beta\cos\gamma}\right). \tag{3.63}$$

The third step in the search for χ equation would be to look at the angle formed between the projection $\mathbf{e}_{z,\omega}\cos\gamma$ and $\mathbf{v}_{k,\omega}$ on the tangential plane. The circumferential velocity acts on the intersection line between the planes C and τ. The original vector $\mathbf{e}_{z,\omega}$ is perpendicular to the velocity vector. Due these properties the unit vector would be rotated around the velocity vector with an angle γ. This means the projected vector $\mathbf{e}_{z,\omega}\cos\gamma$ retains the perpendicularity to $\mathbf{v}_{k,\omega}$ and one could mark the angle between them as $\frac{\pi}{2}$.

The last missing angle to compose χ is between the two kite velocities ($\mathbf{v}_{k,\tau}$, $\mathbf{v}_{k,\omega}$) on plane τ. Looking at Figure 3.8 these two vectors form a right-angled triangle with the small velocity component caused by the changing angle γ due reel-out. This enables the use of a trigonometric function in the calculation of angle between $\mathbf{v}_{k,\tau}$ and $\mathbf{v}_{k,\omega}$. The small velocity component of changing γ can be calculated with

$$r\dot{\gamma} = -f v_w \tan\gamma, \tag{3.64}$$

which originates from Equation 3.29. One should note since in helical flight the value of $\dot{\gamma}$ is negative due decreasing γ value in the reel-out process, a negative sign should be in front of the term to use it in the calculations.

Four different angles ($\pi,\ \theta_{\omega,\tau},\ \frac{\pi}{2}$, and the angle from the trigonometric function) set the value for χ from $\mathbf{e}_\theta$ to $\mathbf{v}_{k,\tau}$ in the helical flight framework when the kite is moving in the positive direction of ω (or χ). As the circumferential kite velocity direction is flipped (flight opposite to the right hand rule) the course angle becomes smaller by π and the value from the trigonometric function should be subtracted as well. The latter can be explained by the shift from $\mathbf{v}_{k,\omega}$ to $\mathbf{v}_{k,\tau}$ which happens in that case in the negative direction of χ. By composing the four step analysis into two cases for course angle, dependent on the direction of the circular movement, the following χ equations could be defined

$$\chi = \left(\theta_{\omega,\tau} + \frac{3\pi}{2}\right) + \arcsin\left(\frac{-r\dot{\gamma}}{v_{k,\tau}}\right), \text{ dir. according to right hand rule} \tag{3.65}$$

$$\chi = \left(\theta_{\omega,\tau} + \frac{\pi}{2}\right) - \arcsin\left(\frac{-r\dot{\gamma}}{v_{k,\tau}}\right), \text{ dir. opposite to right hand rule (left hand rule),} \tag{3.66}$$

where $\theta_{\omega,\tau}$ (Equation 3.63) is the projection of θ_ω on τ and $r\dot{\gamma}$ is the velocity caused by the changing cone angle (Equation 3.64). The calculated course angle can be used in the inertial Equations 2.44-2.50.

The next step would be to define the angular speed on the tangential plane which is the course rate $\dot{\chi}$. Since the angular velocity ω is a division of the kite velocity component acting on the crosswind plane and the turning radius being perpendicular to that velocity vector

$$\omega = \frac{v_{k,\omega}}{R}, \tag{3.67}$$

one could find the course rate using a similar logic. This means the calculation components need to be projected from the crosswind to the tangential plane. The circumferential kite velocity $v_{k,\omega}$ becomes the tangential kite velocity $v_{k,\tau}$ and the velocity-perpendicular component of R is used. Again two cases are set as the positive direction of course rate is defined with the right hand rule. The course rate could be written as

$$\dot{\chi} = \frac{v_{k,\tau}}{R_\perp} = \frac{v_{k,\tau}}{R\cos\gamma\sqrt{1-\left(\frac{r\dot{\gamma}}{v_{k,\tau}}\right)^2}}, \text{ dir. according to right hand rule} \tag{3.68}$$

$$\dot{\chi} = -\frac{v_{k,\tau}}{R_\perp} = -\frac{v_{k,\tau}}{R\cos\gamma\sqrt{1-\left(\frac{r\dot{\gamma}}{v_{k,\tau}}\right)^2}}, \text{ dir. opposite to right hand rule (left hand rule),} \tag{3.69}$$

where R is the constant turning radius of the circular/helical path and $R_\perp$ is the projection of that radius from the crosswind to the tangential plane ($R\cos\gamma$) and then the perpendicular component to $v_{k,\tau}$ taken from that projection.

These course angle and course rate calculations with Equations 3.65, 3.66, 3.68 and 3.69 are only valid for that particular circular or helical flight framework investigated in this chapter. If more general course rate calculation for solving the figures of eight becomes of interest one needs to find the turning radius in different ways as described in Section 3.4.1. The defined equations for linking the analytical approach coordinates and velocities to the QSM framework provide all the necessary parameters to calculate the inertial force with Equation 2.44 and add it to the force balance Equation 2.42 to solve the steady-states of the kite in a simplified simulation framework.

3.4. Numerical Example of a Helical Trajectory Flight with Inertial Effects

The numerical example of the helical trajectory flight has a twofold purpose. First of all, the simulation example provides a validation for the analytically developed force balance with the inertial equations (hereafter analytical approach) in Section 3.2 specifically tailored for this type of simulation problem. Similarly, the example includes the adjusted QSM with the inertial forces. Since the only difference between these approaches is the used coordinate system the output results are expected to be identical. Secondly, the helical trajectory flight example serves as a powerful tool for observing the impact of inertial forces on the kite and compare the massless kite flight situation with the one with inertial forces.

Both approaches for the flight problem follow the corresponding theory presented in Sections 3.2 and 3.3. To make the comparison between the two methods simpler the effect of gravity is eliminated similarly to the analytical approach from the QSM force balance. The latter enables another simplification in the simulation: angle θ_ω and the projection onto $\theta_{\omega,\tau}$ can be kept constantly zero throughout the example. This is based on the following logic.

- The gravity could have a boosting or decreasing effect on the output of the simulation which is dependent on the orientation of the kite velocity vector $\mathbf{v}_k$.
- The inertial effects have the same impact on the kite no matter in which point of the helical/circular path the kite is located. The centrifugal force is always pointing outwards from the centre of the flight path.
- Without the effect of gravity in uniform flight conditions the simulation could be carried out in a way that the kite is always located in a point where $\theta_\omega = 0°$. Only the radial coordinates of the kite change due the reel-out speed.
- This assumption simplifies the Equations 3.65 and 3.66 which can be used without $\theta_{\omega,\tau}$ in them.

The analytical approach starts by μ calculation through iterations. The initial guess for μ_1 could be $\mu_1 = 0$. To find the value for μ_{i+1} one could square Equation 3.37. It is important to note this mathematical operation of squaring simplifies the problem by eliminating the sign distinction from the analytical approach. The equation for μ_{i+1} could be written as

$$\mu_{i+1} = \sqrt{E^2 - \left(\tan\gamma\sqrt{\mu_i^2+1} - \frac{\mu_i^2}{\mu_i^2+1}E\frac{R_{min}}{R}\right)^2}, \text{ for } i = 1, \ldots, n. \tag{3.70}$$

where for the first iteration the position of μ_i is filled by μ_1. For the consecutive iterations the value for μ_i becomes μ_{i+1} calculated in the last cycle up to the point where $\mu_{i+1} \approx \mu_i$. With the calculated μ value the circumferential velocity factor $\overline{\lambda}$, the non-dimensional tether force and the power can be found by using Equations 3.36, 3.39 and 3.42.

In the QSM the inertial force given with Equation 2.44 is added to the force balance. This simulation tool has an iterative solving mechanism built around the kinematic ratio. That parameter is missing from the analytical approach but could be calculated by writing the apparent wind components in the helical flight framework as

$$v_{a,\tau} = \sqrt{v_{k,\omega}^2 + (v_w - v_{k,x})^2 \sin^2 \gamma} \tag{3.71}$$

$$v_{a,r} = (v_w - v_{k,x}) \cos \gamma. \tag{3.72}$$

From the kinematic ratio Definition 2.32 and Equation 3.32 this leads to

$$\begin{aligned} \kappa &= \sqrt{\frac{v_{k,\omega}^2 + (v_w - v_{k,x})^2 \sin^2 \gamma}{(v_w - v_{k,x})^2 \cos^2 \gamma}} = \sqrt{\left[\frac{v_{k,\omega}}{(v_w - v_{k,x}) \cos \gamma}\right]^2 + \tan^2 \gamma} \\ &= \tan \gamma \sqrt{\left[\frac{\overline{\lambda}}{(1 - f_x) \sin \gamma}\right]^2 + 1}. \end{aligned} \tag{3.73}$$

Therefore, the kinematic ratio becomes suitable for the comparison of two approaches.

In the QSM the tangential kite velocity factor λ is the key output parameter for describing the flight of the kite. In the analytical approach it is substituted with the kite circumferential velocity factor $\overline{\lambda}$. To define how $\overline{\lambda}$ relates to λ Equation 3.64 is used. When the kite flies the helical trajectory the circumferential velocity factor can be written as

$$\overline{\lambda} = \sqrt{\lambda^2 - f^2 \tan^2 \gamma} = \sqrt{\lambda^2 - f_x^2 \sin^2 \gamma}. \tag{3.74}$$

With the linked parameters of kinematic ratio and circumferential velocity factor all the necessary tools for the two approach comparison are defined. In this example Kitepower 20 kW pumping kite power system is used. The properties for the chosen kite are presented in Table 3.1. It is relevant to mention since the analytical approach considers only the inertial effects on the kite and the impact of tether is eliminated from the framework the same is done for the QSM. This means the tether has only length but no drag nor mass in the simulation.

20 kW Pumping Kite Power System Properties					
Kite projected area	19.75 m^2	C_L for powered flight*	≈0.60	Tether drag** $C_{D,t}$	1.1
Kite mass	22.8 kg	C_D for powered flight*	≈0.13	Min tether force limit	300 N
Tether diameter**	0.01 m	C_L for depowered flight*	≈0.36	Max tether force limit	5000 N
Tether density**	724 $\frac{\text{kg}}{\text{m}^3}$	C_D for depowered flight*	≈0.12	Min reeling speed	0 $\frac{\text{m}}{\text{s}}$
				Max reeling speed	10 $\frac{\text{m}}{\text{s}}$

Table 3.1: The properties of 20 kW Kitepower system. [28] The aerodynamic coefficients marked with one asterisk (*) are the results of an optimization described in Section 4.1.2. The tether parameters marked with two asterisks (**) are excluded from this simulation. Only the tether length is considered.

In this example the kite is made to fly a helical path in uniform downwind conditions with constant speed in the downwind direction. The setup is similar to what could be observed from Figure 3.2 with an exception $\theta_\omega = 0°$ throughout the simulation. The R is kept constant meaning if the kite reels out the

Helical Flight Properties			
Wind speed	8.5 $\frac{m}{s}$	Helix radius R	30 m
Air density ρ	1.225 $\frac{kg}{m^3}$	Starting tether length r_{start}	150 m
Downwind speed factor f_x	0.37	Ending tether length r_{end}	700 m

Table 3.2: Helical flight properties for the example simulation

cone angle 2γ decreases. For the start and stop tether length, values which show the relevant case distinction points in graphs are selected. The flight parameters can be seen in Table 3.2.

The simulations are run in two sets. First, the kite has the mass property defined and the inertial forces have impact on the simulation outputs. As was already mentioned, the effect of gravity is excluded from the simulation. In the second set of simulations the kite is considered to be massless. This means only the aerodynamic and tether force act in the force balance equation. The results are compared in circumferential velocity factor $\overline{\lambda}$, kinematic ratio κ, non-dimensional tether force and non-dimensional power. These output parameters are plotted in Figures 3.12-3.15 and discussed in Section 3.4.1.

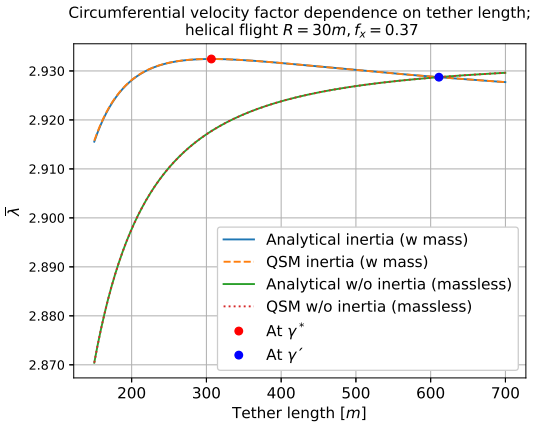

Figure 3.12: Circumferential velocity factor $\overline{\lambda}$ difference between the QSM and the analytical approach at helical flight

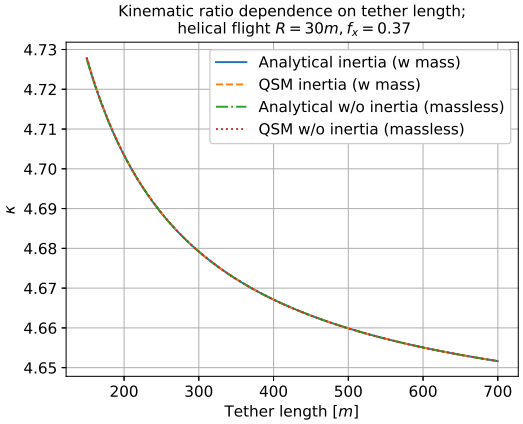

Figure 3.13: Kinematic ratio κ difference between the QSM and the analytical approach at helical flight

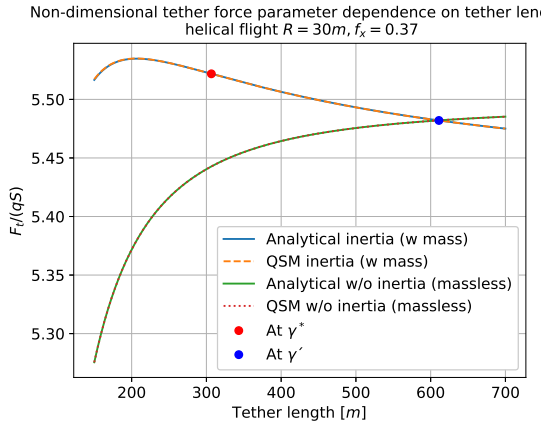

Figure 3.14: $\frac{F_t}{qs}$ difference between the QSM and the analytical approach at helical flight

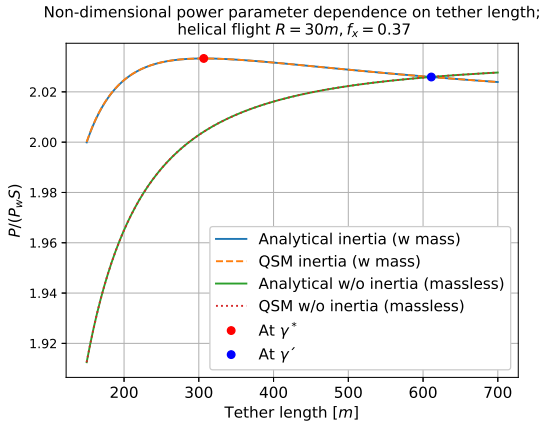

Figure 3.15: $\frac{P}{P_w S}$ difference between the QSM and the analytical approach at helical flight

In addition to comparative parameters two relevant points are marked in the figures as red and blue dots. The red marker shows the tether length which in triangular formulation with R would give γ^*.

This angle is calculated with Equation 3.11 and symbolizes the point between the case distinction in Equations 3.14 and 3.15. The other blue marker shows the point where the inertial forces when going to either direction in tether length could increase the tether force (shorter tether lengths) or decrease that parameter (longer tether lengths). The representative angle for this distinction is γ'. The simulation is at γ' when on plane Π the vectors $-(\mathbf{F}_t + \mathbf{D})$ and $\mathbf{L}$ are symmetrically set around $\mathbf{L}_0$, the projection of lift force on $x_\omega y_\omega$-plane. Both vectors $-(\mathbf{F}_t + \mathbf{D})$ and $\mathbf{L}$ have also an equal magnitude at this angle. Figure 3.16 shows the special case for $\gamma = \gamma'$.

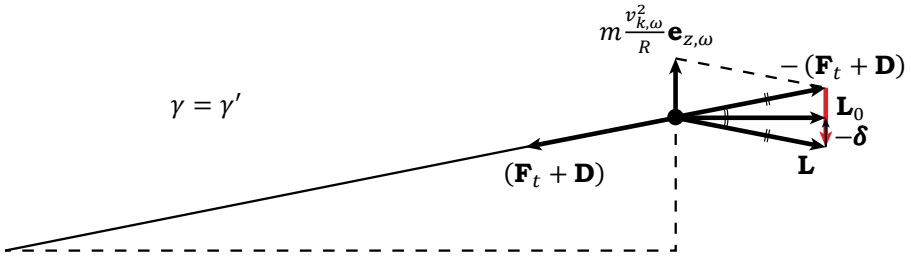

Figure 3.16: Helical/circular flight Π-plane view. The special case of $\gamma = \gamma'$. For larger γ values the centrifugal force contributes to the tether force. For smaller γ the centrifugal force reduces the tether force.

One could calculate this γ' by knowing the value for $\gamma*$ and using formula

$$\tan\gamma' = \frac{\tan\gamma^*}{2}, \tag{3.75}$$

which originates from the geometric similarity. The values for these angles in the particular example case are given in Table 3.3.

Case Distinction Angles	
Sign distinction parameter $\gamma*$	5.61°
Tether force increase/decrease distinction parameter γ'	2.81°

Table 3.3: Case distinction angles in helical flight example

3.4.1. Discussions About Helical Flight Example

The observations and discussions in this section are mainly based on Figures 3.12-3.15 which provide an overview for both approaches to the helical flight problem as well as bring out the unique properties of inertial force impact dependence on cone angle. The following remarks could be drawn.

- All the figures show a perfect overlap in results received with both methods. This means the analytical approach validates the inertial equations provided by Schmehl et al and vice versa.
- The maximum value of parameter μ_{max} is lift-to-drag ratio E. Since the downwind speed factor f_x is kept constant and $\bar{\lambda}$ and μ are tied together via Equation 3.36 the maximum circumferential velocity factor under these example conditions cannot exceed the value of 2.932. This is marked with the red dot in Figure 3.12. That observation also means the maximum power with inertial force flight is reached at the very same spot according to Figure 3.15. From the power generation perspective it is beneficial to fly turns which together with the turning radius R and the tether length r would form the angle γ^*. Although, the power increase caused by the inertia in this example from the massless flight is only 1.45% at the red marker position.
- The tether force does not peak at $\gamma = \gamma*$ but has bigger values at certain points where $\gamma > \gamma*$. The justification for that kind of behavior originates from Equation 3.39 where $\cos\gamma$ is in

the denominator and division with smaller numbers occurs at larger γ values. The $\overline{\lambda}$ does not experience sudden drop close to the red marker which could diminish the effect caused by $\cos\gamma$.

- The inertial force could also have a decreasing effect on the kite circumferential velocity $\overline{\lambda}$, tether force and power compared to the massless situation. That happens at angles $\gamma < \gamma'$, meaning the turning radius R is very small in relation to tether length. Keeping in mind the principle of power maximization then these small value of R & big value of r combinations should be avoided. However, further distancing from the perfect downwind position with bigger flight path shapes and R values could have the opposite effect on these three output parameters ($\overline{\lambda}$, tether force and power). A follow-up study is required here.
- Despite the small change in $\overline{\lambda}$ the kinematic ratio κ remains similar for both the massless and the inertial cases. This can be justified by the dampening effect of these $\overline{\lambda}$ changes by mathematical operations performed in Equation 3.73.

The helical flight at the perfect downwind conditions, without the effect of gravity and constant speed $v_{k,x}$ is an idealized flight situation. For further studies a step towards more realistic reel-out flight paths (e.g. figures of eight) flown at azimuth-elevation combinations close to the measurement values would be recommended. The value for turning radius R could be problematic in these cases. Three possible ways to set R in these situations are listed.

- Make R a simulation control parameter.
- Use turning radius from the measurements. For instance, the average R of figure or phase could be used as a constant.
- Include the coordinates of the previous or the following steady-state in the instantaneous steady-state calculations. By observing the change in course angle the course rate can be estimated.

4

Modeling Pumping Operation

The certain level of deviation in the QSM power output from the measurements has been presented in Section 2.4.4. This inaccuracy is considered to be caused by a set of simplifications and assumptions in the QSM. One of these simplifications is the reel-out flight path used in the model. This chapter is investigating different approaches to generate the flight path in the QSM during the reel-out phase. The accuracy of these methods from an output power perspective is quantified. An attempt to optimize the flight path for the output power maximization is also made.

The chapter starts by setting up reference QSM simulations. The idea is to compare the QSM power output when flying different reel-out flight paths to the reference case. The first attempt for the reference simulations is made by using the default QSM with the aerodynamic coefficients proposed in Section 2.4.4. This is followed by a tuning of C_L and C_D as an optimization problem which sets the reference simulations. The accuracy of a constant azimuth-elevation combination is investigated next. The second half of the chapter focuses on finding a method for reel-out figure of eight parameterization and the QSM power accuracy is estimated by flying fitted figures with the least geometrical deviation from the measurement flight paths. The chapter ends with an optimization for power-maximizing figure of eight.

4.1. Setting Up Reference QSM Simulations

The QSM calculates the instantaneous output power of a pumping kite power system by assuming a force balance between tether, aerodynamic, gravitational and/or inertial forces. The model is built on several assumptions described in Section 2.4. If the evaluation and improvement of some of these assumptions becomes of interest one needs to have a fixed reference simulation case. Further changes to the model would be compared to these fixed values. The objective is to provide reference simulations using a set of measurement data and adjust the QSM inputs for that particular dataset.

The measurement data used for setting up the basis QSM simulations is provided by Kitepower B.V. [9] With their 20 kW pumping kite power system Kitepower run 87 pumping cycles on 8 October 2019 in Valkenburg (the Netherlands). 86 of these cycles have a complete set of measurements together with instantaneous and phase-averaged wind data. The latter has been transformed and reconstructed into correct reference frame by Schelbergen and Schmehl as described in Section 2.4.4. For the QSM simulations based on the data only some parts of the measurements are relevant. The following list brings out these key parameters.

- Time [s] tells when each measurement is taken. The points are measured with 0.1 s interval.
- Coordinates of the kite. These are given in Cartesian coordinates in [m] but could be converted into spherical coordinates. The coordinates include course angle χ.
- Wind speed [m/s]. Both, the instantaneous and average wind for each phase in the correct reference frame are provided by previous authors (Section 2.4.4).
- Reel-out speed of the kite [m/s].

- Tether force [N].
- Radial distance from the ground station to the kite [m]. This is considered as the tether length in the QSM.
- Phase and pattern description. That indicates in which phase the kite is running in at the particular time instance and which figure of eight is in action. The kite completes three figures of eight during the reel-out.

The idea is to take the environmental properties, the coordinates of the kite together with the radial distance from the measurements and based on the phase description calculate the reel-in or reel-out power with the QSM. The target power originates directly from the measurements as the multiplication of reel-out speed and tether force. For the reference simulation case the mean (or median) QSM error from the simulations is fixed. Then for instance by implementing the simplification of substituting the measurement coordinates with the time-averaged values using Equations 2.60 and 2.61 one could calculate the new power deviation from the measurements and compare the results to the reference simulation. This gives an estimation about the accuracy of an implemented change. To set up the reference simulations with minimal error a suitable set of aerodynamic coefficients could be used as QSM inputs.

4.1.1. Quantifying the Default QSM Accuracy

The accuracy of QSM is presented in Section 2.4.4 where Schelbergen and Schmehl run the QSM simulations for the same set of measurements used in this section. They calculate the aerodynamic coefficients as simulation inputs using Equation 2.66. However, the authors discuss these calculated parameters do not reflect the reality due a stiff rod assumption for the tether. Based on that discovery they tune the generic aerodynamic coefficients and run the QSM for all the measurement cycles. Combining the retraction, transition and traction power they find the QSM to underestimate the power with -26.4% in comparison to measured results.

In the context of estimating the accuracy of aerodynamic coefficients for setting up a reference simulation reel-in and reel-out phases are the most relevant. The transition phase is much more complicated in that sense the switching instance from the depowered flight parameters to the powered ones may differ between the cycles. This makes it problematic to correctly calculate C_L and C_D. Therefore, the QSM simulations are done here for the traction and retraction phase using as an input:

- tuned aerodynamic coefficients proposed in Table 2.2;
- system properties (except C_L and C_D) from Table 3.1;
- exact kite coordinates from the measurements, including the radial distance;
- reel-out speed from the measurements;
- average wind input for each phase.

The result is compared to the measurement power $P_m(t)$ of the same time instance t calculated with

$$P_m(t) = F_t(t)v_t(t), \tag{4.1}$$

where $F_t(t)$ is the tether force of the same measurement point and $v_t(t)$ the reel-out speed. One arrives at relative power difference [%] with

$$P_e(t) = \frac{P_{QSM}(t) - P_m(t)}{P_m(t)} \times 100, \tag{4.2}$$

where $P_{QSM}(t)$ is the QSM calculated power for that measurement instance, $P_m(t)$ the measured power and $P_e(t)$ the power error. Equation 4.2 is used for the reel-out relative power difference calculation. For the reel-in phase $P_{QSM}(t)$ and $P_m(t)$ switch positions in the numerator due negative power values during the reel-in. That way a QSM negative error in relative power difference from the measurements would be an indication the QSM output power is also more negative than what is measured. This means in the model more energy would be consumed during the reel-in when compared to the reality. Positive error would show the opposite.

This type of simulation quantifies the default QSM accuracy as it is proposed by previous authors. The reel-in and reel-out relative power difference between the QSM and the measurements can be seen in Figures 4.1 and 4.2 where the averaged QSM output error is showed with red line, median error with orange and the light blue line represents the target measurement value at 0% relative difference. The calculation is done for all the measurement points in the phase for 86 cycles and the QSM relative error is divided into 5% bins.

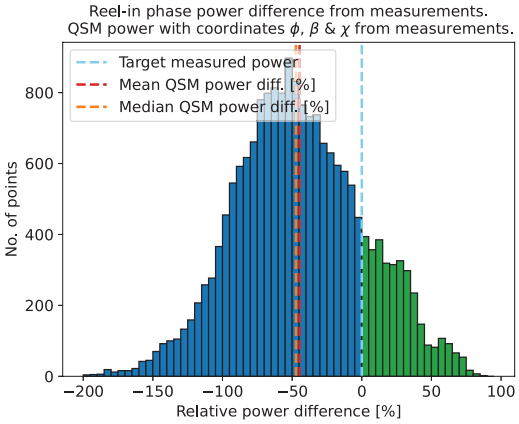

Figure 4.1: Reel-in phase QSM relative power difference from measurements. The used aerodynamic coefficients are proposed in Table 2.2

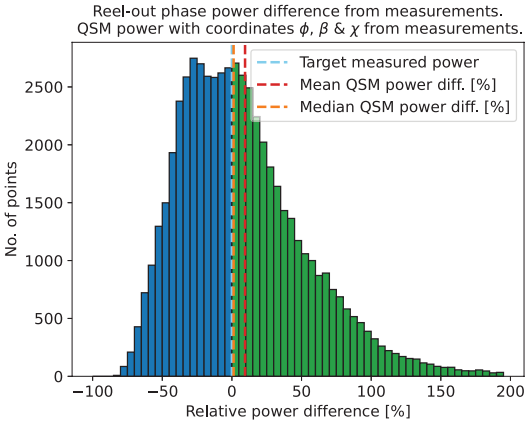

Figure 4.2: Reel-out phase QSM relative power difference from measurements. The used aerodynamic coefficients are proposed in Table 2.2

Reel-In and Reel-Out Phase Default QSM Power Relative Difference from Measurements			
Parameter	**Method**	**Reel-in**	**Reel-out**
Power	Median	-47.274%	1.219%
	Mean	-44.670%	9.441%

Table 4.1: Reel-in and reel-out phase default QSM power output relative difference from the measurements. These numbers are achieved by running the simulation over 86 cycles

Table 4.1 where the median and mean comparison results between the QSM power output and the measured power are written brings the attention to a substantial error in the reel-in power accuracy. The negative error is an indication the QSM on average or in median calculates to a bigger power usage by absolute value than it appears in the measurements. The large negative error also shows that even with the slightly tuned aerodynamic coefficients from the calculated values the misalignment of tether force in reality is much different than assumed in the calculations. The overall QSM power underestimation with the tuned aerodynamic coordinates presented by Schelbergen and Schmehl is consequently mainly driven by the reel-in phase. The exact ratio of reel-in negative and reel-out positive error for the overall cycle error depends on the duty cycle of these phases.

The results received in the reel-out phase have in contrary a marginal error. The median power deviates from the measurements only by 1.2%. However, this result presents the accuracy of flying measurement coordinates for the reference simulation. The error one gets representing the reel-out flight path in the simulation differently than it appears in the measurements is currently unknown but investigated in the later sections of this chapter.

Based on the observations of running the QSM with measurement inputs and C_L & C_D values provided by previous authors the aerodynamic coefficients require further tuning to minimize the error between the QSM outputs and the measurements. The error is significantly large in the reel-in phase which should be in the focus of that process. Additionally, the same tuning methods could be applied to the reel-out phase as well to eliminate even the smallest errors from the reference simulations.

4.1.2. Aerodynamic Coefficients Optimization

To set up a reference QSM simulation which does not deviate in relevant results (power, kite velocity) from the measurements, a new tuning for finding C_L and C_D is conducted. The aerodynamic coefficients for the reel-in and reel-out phase are optimized using the best fit principle for the given Kitepower measurement dataset. Since power is the ultimate output parameter of the QSM that is of interest for the client-user of pumping kite power system the optimizer is set up for fitting the QSM output power to the measurement power. To avoid the possibility of faulty measurements for some time instances in any of the dataset parameters having a substantial impact on average power the median power difference between the QSM calculations and the measurements is minimized instead. Since the median splits the error distribution in half the error bin spread in both sides of the target value is expected to be more homogeneous.

Yet, the power cannot be the only parameter used in the search for the best combination of lift and drag coefficients. By looking at the non-dimensional power Equation 2.40 the ratio of lift and drag is relevant for the power calculation. However, the same E could be achieved with various sets of C_L and C_D. Therefore, there is no particular answer for the exact values of aerodynamic coefficients. For two optimization variables two equations to find the best fit for are required. The other parameter used for fitting could be the velocity of the kite v_k.

The total kite velocity is given with Equation 2.28 and consists of the radial $v_{k,r}$ and the tangential kite velocities $v_{k,\tau}$. In optimization, $v_{k,r}$ can be imported directly from the measurements as the reel-out speed of the kite. For $v_{k,\tau}$ the tangential kite velocity factor λ is calculated with QSM using Equation 2.54 which also directly depends on the values of C_L and C_D. One could observe that by looking at the gravity-excluded version of λ Equation 2.35 where the lift-to-drag ratio is included. Similarly to power error Equation 4.2 the kite velocity error $v_{k,e}$ [%] becomes

$$v_{k,e}(t) = \frac{v_{k,QSM}(t) - v_{k,m}(t)}{v_{k,m}(t)} \times 100, \tag{4.3}$$

where $v_{k,m}(t)$ is the measured and $v_{k,QSM}$ the calculated kite velocity for that time instance. With the velocity of the kite and power two relevant target and QSM output parameters exist for the aerodynamic coefficients optimization.

To set up the optimization problem the Sequential Least Squares Programming (SLSQP) and the least square fitting technique are used. These terms are opened more in a form of a brief discussion in Appendix A. Two different cases of optimization problems are distinguished here. The first optimization finds C_L and C_D for the reel-in phase. The second optimization calculates these coefficients for the reel-out phase. Both cases are similar in structure but differ in measurement data inputs and optimization variable boundaries set.

Reel-In Phase Aerodynamic Coefficients Optimization

The aim of the reel-in phase is to restore the starting tether length for the reel-out phase. Since this process consumes energy the perspective is to minimize the losses by aligning the kite with the direction of wind. Hence, the lift and drag coefficients are reduced in comparison to the reel-out phase coefficients. To find these specific and justified $C_{L,in}$ and $C_{D,in}$ values for the measurement set the optimizer requires boundaries. The work of Arthur Roullier presented in [18] provides relevant lift and drag coefficient measurements to set up these boundaries. In his work the soft-wing kite measurement points for $C_{L,in}$ fall between [0.18, 0.4] and for $C_{D,in}$ between [0.05, 0.18]. It is necessary to mention since his work excluded the KCU from the calculations the drag of the pumping kite power system could be underestimated. Here, the kite drag coefficient is optimized counting for all the flying parts of the system except the tether which has its separate drag coefficient implemented. Using the boundaries and basing on the SLQSP optimization theory the optimization problem for the reel-in aerodynamic coefficients becomes

$$\min \left[M_{P,e}(C_{L,in}, C_{D,in}, \mathbf{a})^2 + M_{v,e}(C_{L,in}, C_{D,in}, \mathbf{a})^2 \right] \tag{4.4}$$

$$\text{subject to } C_{L,in} \in [0.18, 0.4]\,,\ C_{D,in} \in [0.05, 0.18]\,, \tag{4.5}$$

where $M_{P,e}$ and $M_{v,e}$ denote the QSM output median power and the median kite velocity error from the measurement values. The error is calculated with Equations 4.2 and 4.3. The vector $\mathbf{a}$ includes all the

relevant arguments for the optimizer to find the solution. The arguments include the system properties, the environmental parameters, the reel-in speed of the kite and the exact coordinates (r, β, ϕ) & χ of the kite from measurements. The same inputs are used here as provided in the list in Section 4.1.1 with the exception aerodynamic coefficients are made optimization variables. The optimization is carried out using all the reel-in measurement points from 86 cycles. The aerodynamic coefficients obtained for the reel-in phase are shown in Table 4.2.

The Optimized Aerodynamic Coefficients			
$C_{L,in}$	0.355	$C_{L,out}$	0.597
$C_{D,in}$	0.118	$C_{D,out}$	0.128

Table 4.2: The optimized aerodynamic coefficients for the measurement data provided by Kitepower

Running the simulations again for the reel-in phases now with the optimized $C_{L,in}$ and $C_{D,in}$ the point-wise comparison between the measured power and kite velocity values and the QSM calculated parameters indicates very little median deviation. These results are shown as Figures 4.3 and 4.4. The target measurement values are given as light blue lines and the median and mean error values of the QSM outputs for the 86 reel-in phases as orange and red lines. According to Table 4.3 the median power difference is only 7.764e-5% and the respective number for kite velocity is -1.726%. These numbers set a reference case for the point-wise comparison.

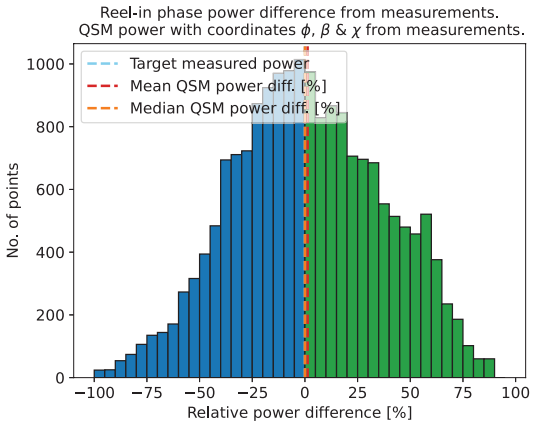

Figure 4.3: Reel-in phase QSM relative power difference from measurements. The optimization is done for aerodynamic coefficients using all the measurement points.

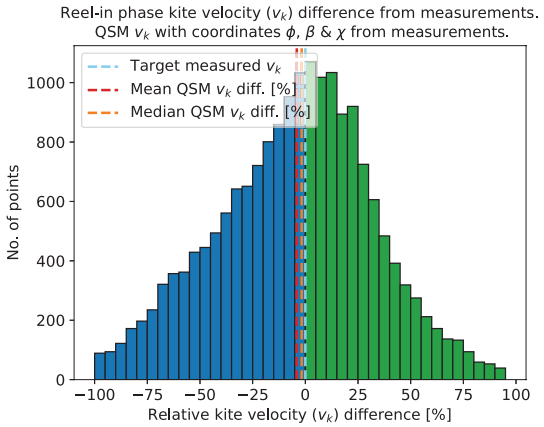

Figure 4.4: Reel-in phase QSM relative v_k difference from measurements. The optimization is done for aerodynamic coefficients using all the measurement points.

Optimizing using each data point from the measurements finds the best fit between the QSM outputs and the measurements. However, several assumptions about the flight path could change the number of steady-state points QSM calculates the power output for. In other words, with fewer calculations in the QSM the power and the kite velocity estimations for the whole phase are attempted. This makes the point-wise comparison between the QSM and the measurements difficult. For that reason a reference case for the average phase values is needed. This means the particular parameter is time-averaged first for the phase in both measurements and QSM outputs and the averaged values are compared instead. The power averaging goes by equation

$$P_{avg} = \frac{1}{T_{end} - T_{start}} \int_{T_{start}}^{T_{end}} P(t)dt, \tag{4.6}$$

where T_{start} and T_{end} are the start and the end time instances of the phase. $P(t)$ denotes either measured power $P_m(t)$ or calculated power $P_{QSM}(t)$ at time t depending on whether the calculation goes for the measurement or the QSM output time-average calculation. For the time-averaged kite velocity similar equation could be written as

$$v_{k,avg} = \frac{1}{T_{end} - T_{start}} \int_{T_{start}}^{T_{end}} v_k(t)dt, \tag{4.7}$$

with the difference of including $v_k(t)$ in the calculation instead.

Using the same point-wise optimized $C_{L,in}$ and $C_{D,in}$ the reference case for the phase-averaged values is given here as Figures 4.5 and 4.6 and in Table 4.3. Since the coefficients are not optimized for the usage of averaged phase values the results are more off. However, this could still be used as a case for comparison after modifications to the QSM are made.

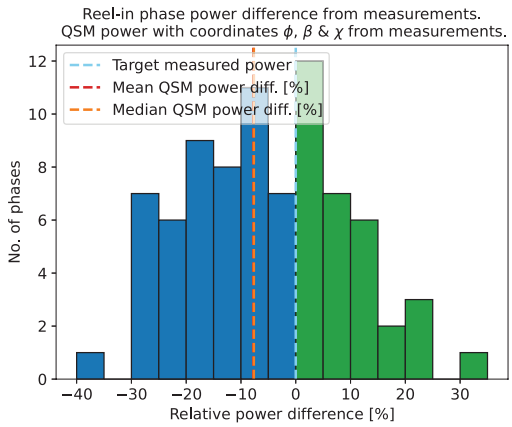

Figure 4.5: Reel-in phase QSM relative power difference from measurements. The same aerodynamic coefficients are used as the results of the optimization for the points.

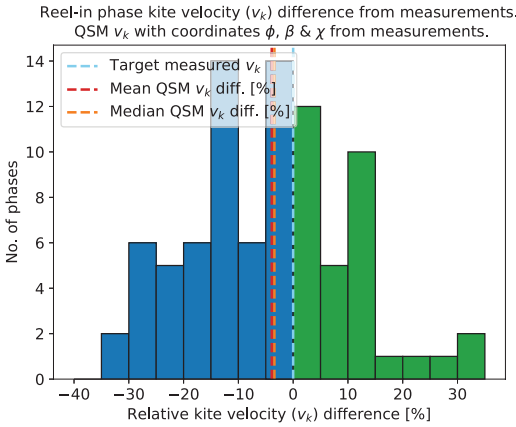

Figure 4.6: Reel-in phase QSM relative v_k difference from measurements. The same aerodynamic coefficients are used as the results of the optimization for the points.

Reel-In Phase QSM Output Relative Difference from Measurements			
Parameter	**Method**	**All measurement points**	**Time-averaged phases**
Power	Median	7.764e-5%	-7.656%
	Mean	1.270%	-7.735%
Kite velocity	Median	-1.726%	-3.422%
	Mean	-4.064%	-3.911%

Table 4.3: Reel-in phase QSM output relative difference from the measurements. These numbers are achieved by running the simulation over 86 reel-in phases

Reel-Out Phase Aerodynamic Coefficients Optimization

Similarly to the reel-in phase the measurement point-wise QSM modification is done for the reel-out phase. The list of QSM inputs presented in Section 4.1.1 is still valid here. The search for the most suitable $C_{L,out}$ and $C_{D,out}$ for the given measurement set starts by defining the optimization boundaries. In the work of Roullier the $C_{L,out}$ measurements fall between [0.4, 0.8] and for $C_{D,out}$ in [0.1, 0.4]. [18] Using these bounds the optimization problem could be set up as

$$\min \left[M_{P,e}(C_{L,out}, C_{D,out}, \mathbf{a})^2 + M_{v,e}(C_{L,out}, C_{D,out}, \mathbf{a})^2\right] \tag{4.8}$$

$$\text{subject to } C_{L,out} \in [0.4, 0.8]\,,\ C_{D,out} \in [0.1, 0.4]\,. \tag{4.9}$$

The coefficient results for the reel-out phase point-wise optimization are shown together with the reel-in phase respective coefficients in Table 4.2.

Using the optimized coefficients in the QSM reel-out phase simulation it could be observed from Table 4.4 the median accuracy over 86 cycles is comparable to the reel-in simulation in power but

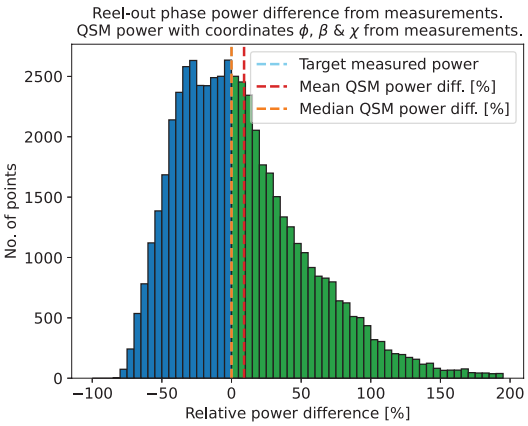

Figure 4.7: Reel-out phase QSM relative power difference from measurements. The optimization is done for aerodynamic coefficients using all the measurement points.

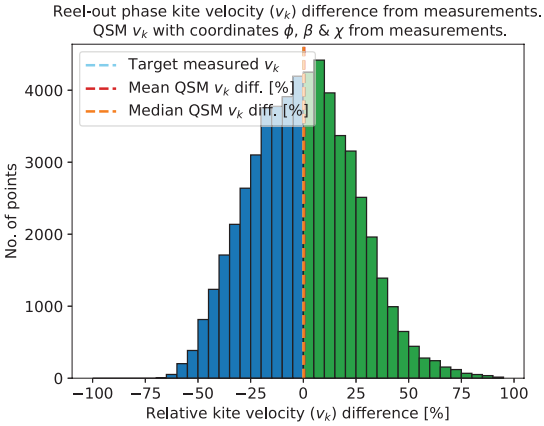

Figure 4.8: Reel-out phase QSM relative v_k difference from measurements. The optimization is done for aerodynamic coefficients using all the measurement points.

better in kite velocity for the reel-out phase in comparison to the reel-in phase. This can be explained by looking at Figures 4.4 and 4.8. For the reel-out phase the kite velocity v_k has a more uniform error and the deviations bigger than 75% from the measurement target are rare. Whereas for the reel-in phase v_k error up to 100% is common. In the QSM tether is considered inelastic without sagging. However, sagging is a usual phenomenon during the reel-in when the tether experiences less tension compared to the reel-out phase. It has a direct impact on the reel-in speed. This is one reason for bigger inaccuracy between the measurement and the QSM calculated v_k.

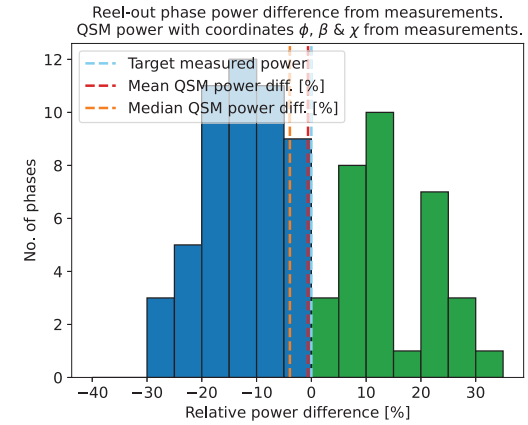

Figure 4.9: Reel-out phase QSM relative power difference from measurements. The same aerodynamic coefficients are used as the results of the optimization for the points.

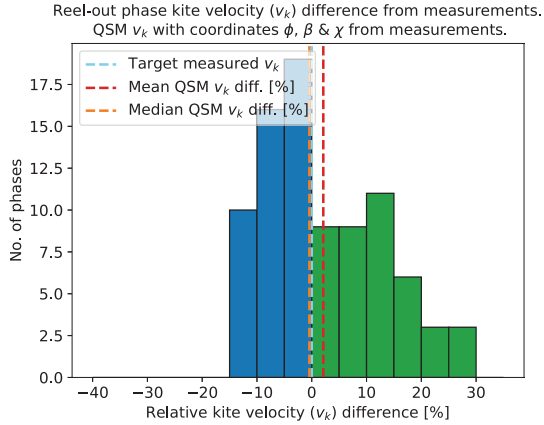

Figure 4.10: Reel-out phase QSM relative v_k difference from measurements. The same aerodynamic coefficients are used as the results of the optimization for the points.

The reel-out flight path simplification and analysis on the accuracy of this assumption needs a reference reel-out phase simulation using the averaged phase values. These are calculated again with Equations 4.6 and 4.7. The simulation results using the point-wise optimization coefficients for the time-averaged phase values are presented in Figures 4.9 and 4.10. The most significant error in this type of simulation is experienced in median power (-3.923%) but at the same time mean power gives more accurate results (-0.606%) according to Table 4.4. The latter serves as one of the most important reference values since the reel-out phase flight path is investigated in the following sections and the impact on average power is the key value in comparison between different approaches.

Reel-Out Phase QSM Output Relative Difference from Measurements			
Parameter	**Method**	**All measurement points**	**Time-averaged phases**
Power	Median	0.002%	-3.923%
	Mean	9.022%	-0.606%
Kite velocity	Median	0.125%	-0.435%
	Mean	0.390%	2.107%

Table 4.4: Reel-out phase QSM output relative difference from the measurements. These numbers are achieved by running the simulation over 86 reel-out phases.

4.2. Reel-Out Flight Path Representation

Reel-out phase is responsible for the majority of energy production in pumping kite power system. Therefore, it is essential to resolve the sequential steady-states during this phase with the highest accuracy to measurements. It is observed from Section 4.1.2 that QSM gives relatively good power and kite velocity estimation on average (or in median) when the aerodynamic coefficients are optimized and the steady-states are calculated with kite coordinates originating from the measurements. Using the measurement (r, β, ϕ) & χ eliminates any deviations in simulation flight path from reality. However, that type of approach cannot be adapted for future power estimations which do not have the measurement data available. The same goes for locations which have comprehensive weather data but no flight test results. In both cases a simple flight model derived from the experimental data but with the capabilities of reproducing the flight path based on environment and kite properties is required.

Two different approaches are investigated in this section together with a comparison to reference case set in Section 4.1.2. The first simplified reel-out phase representation is theoretically introduced in Section 2.4.3. The constant azimuth and elevation combination for the whole reel-out phase is employed in the current QSM. The second approach is to describe the reel-out with a generalized equation for figure of eight and modify it to have a better geometrical fit to the actual flight path. This is described in Section 4.2.2.

4.2.1. Reel-Out Flight with Constant Angles

Constant azimuth and elevation angle combination for the whole traction phase is based on the logic there exist certain angles which as an input for the steady-state calculations would result in the same time-average traction force and power as flying the actual figures of eight with the kite coordinates originating from measurements.

This angle combination is hypothesized to be calculated taking the time-average of trigonometric functions of ϕ and β as could be seen from Equations 2.60 and 2.61. Following the same logic the average course angle would be

$$\cos \chi_0 = \overline{\cos \chi}. \tag{4.10}$$

The latter is essential for the apparent wind velocity decomposition (Equation 2.31) and the tangential kite velocity factor λ calculation (Equation 2.54) having impact on power production. As shown by Schmehl et al when course angle χ approaches $180°$ the power production decreases and increases when the angle approaches $0°$. This concept becomes relevant in the following sections.

Single Figure of Eight

In order to give an example how this time-averaging theory finds a representative combination of angles, a flight test case together with the measurement data by Kitepower is used. [9] This dataset of 86 cycles is introduced in Section 4.1. The 56th pumping cycle is chosen here for the reference cycle since no anomalies are experienced in the wind conditions nor in the operation of system.

Figure 4.11 shows the third figure of eight from the reel-out phase of the 56th cycle. Applying Equations 2.60, 2.61 and 4.10 an example representative point for this particular figure together with the course angle is found. The latter is measured on tangential plane from unit vector $\mathbf{e}_\theta$ as shown in Figure 2.9.

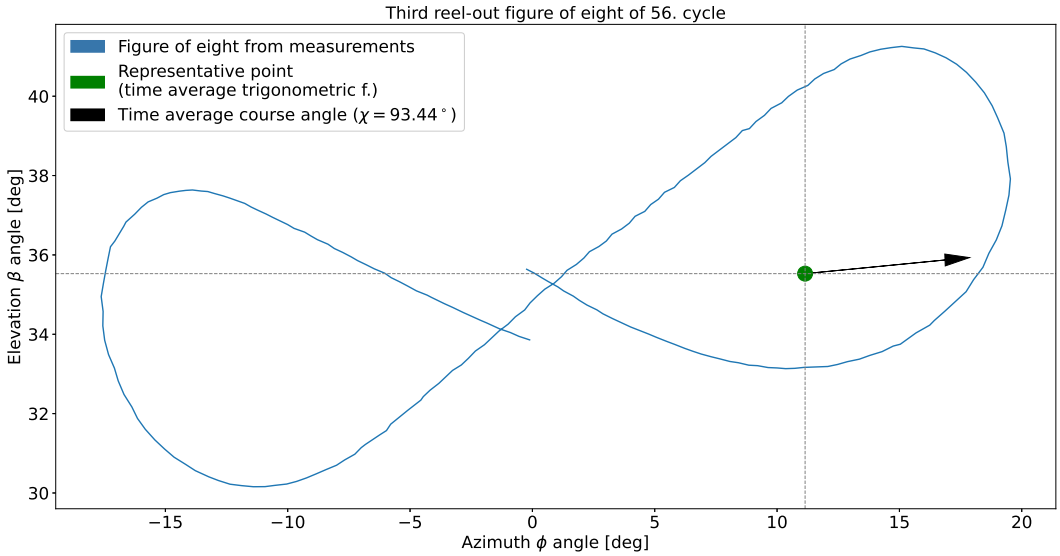

Figure 4.11: The third figure of eight of reel-out phase of the 56th cycle. Green point is received by taking the time average of trigonometric functions $\overline{\cos\phi}$ and $\overline{\cos\beta}$. Arrow shows the direction of tangential kite velocity with a course angle from $\overline{\cos\chi}$.

To estimate the accuracy of such a combination of fixed angles three different ways of calculating the average power are used. The first method finds power with measured tether force and reel-out speed of the kite. In this case the average power is calculated with Equation 4.6 with the difference T_{start} and T_{end} are the start and end time instances of figure of eight and $P(t)$ (Equation 4.1) is a multiplication of measured tether force $F_{t,m}(t)$ and measured reel-out speed $v_{t,m}(t)$. Equation 4.6 is also used for the second approach with the difference now $P_{QSM}(t)$ is calculated with the QSM using all the measured coordinates from data. The third method takes use of time-averaged trigonometric functions of measured coordinates and the power is calculated with a single representative point for the whole figure of eight. For this case it is essential to mention several other parameters in addition to kite coordinates are also the time averages of measurement data: the reel-out speed and the radial distance. Using these parameters the single point QSM average power is calculated with a steady-state iterative algorithm described in Section 2.4. The results for three calculation approaches are shown in Table 4.5.

Third Figure of Eight from 56. Reel-Out Phase: QSM vs Measurement Data	
Measured average power	3405 W
QSM average power (measured coordinates)	2756 W
QSM average power (averaged coordinates)	2640 W

Table 4.5: The time average power output from the measured data and from the QSM using measured coordinates and constant angles for the third figure of eight of the 56th cycle

The QSM underestimates the average power in both cases. Comparing the results of QSM with coordinates directly originating from measurements to Figure 4.9 it can be hypothesized the selected figure of eight might belong to a reel-out phase with a lower end of power accuracy. Averaging the coordinates reduces the accuracy for that figure of eight even more. To investigate whether latter is an usual trend or not requires expansion of the method to all 86 reel-out phases. This expansion is looked into in the end of this section.

In parallel it is investigated how this constant azimuth-elevation-course angle set could be improved to increase the accuracy of power output. If the angles calculated by time-averaging the trigonometric functions give a result which underestimates the average power, there may exist another azimuth-

elevation-course angle combination which would result in an accurate steady-state power instead. For this reason Figure 4.12 is plotted as the result of an optimization problem

$$\min \left[P_{QSM}(\phi, \mathbf{a}) - P_{avg,m}\right]^2 \tag{4.11}$$

$$\text{subject to } \phi \in [0, 90°], \tag{4.12}$$

where $P_{avg,m}$ is the measured time average power for the figure and P_{QSM} is the QSM calculated value. Vector $\mathbf{a}$ includes a fixed set of course angles χ close to what is calculated with Equation 4.10 and elevation $\beta \in [0, 90°]$ values are passed to the optimizer. Indeed, different course angles χ have various azimuth-elevation pairs that would result in the target measured average power. These azimuth-elevation points are situated on the curves.

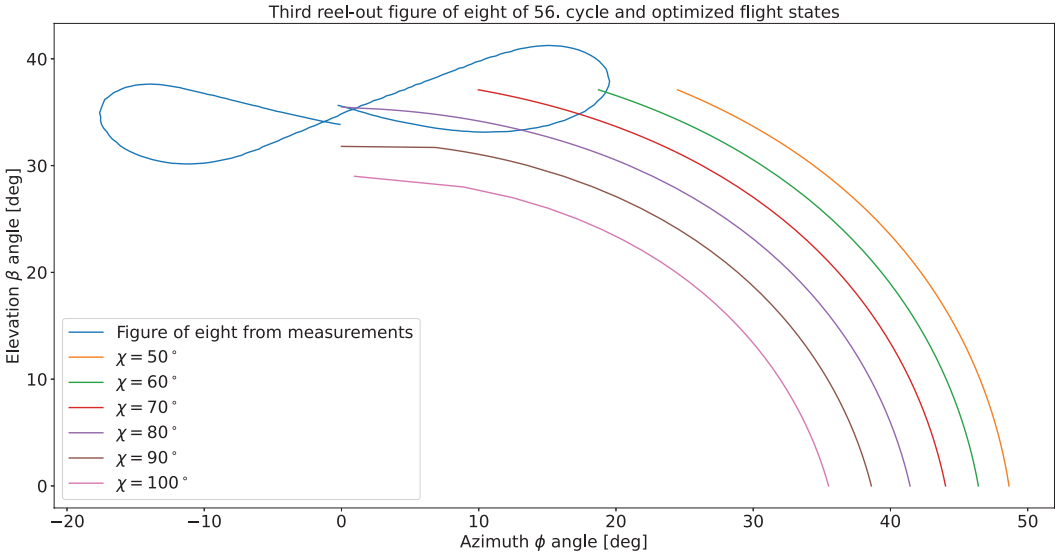

Figure 4.12: For various course angles there exist multiple azimuth-elevation combinations that as a QSM steady-state calculation would result in the same power output as the time average from the measurement data. These azimuth-elevation points are situated on the curve of the corresponding course angle.

Similarly, for a fixed azimuth-elevation combination there should be a course angle that would result in desired target power output from the steady-state calculations. This statement is valid if the power belongs to a certain region: power cannot be indefinitely adjusted with the change in a single angle parameter. Even though such angle modification is not justified, meaning the kite has specific angles during the reel-out and artificially introducing angle combination that is e.g. not an average representation of these angles but more of a compensation of inaccuracy in other steady-state inputs is not correct, then this solution is investigated as a mathematical exercise.

Keeping that in mind, two graphs as Figure 4.13 and 4.14 are shown. These contour plots indicate regions of azimuth and elevation combinations at a fixed course angle. The course angle chosen is the time average of trigonometric function (Equation 4.10) of the third figure of eight of the 56th cycle. The colors in Figure 4.13 show how much the QSM calculated power using these particular three angles would deviate from the measurement time average power. The Figure 4.14 has a similar principle but here instead of power difference, the generated power values are given. It can be observed more power is generated as the kite situates closer to the perfect downwind position $(0°, 0°)$. The black dot indicates the coordinates of the point calculated in Figure 4.11. The graphs show that indeed there exist azimuth and elevation angles that would result in the target measurement power with the course angle received from $\overline{\cos \chi}$.

Expanding the Simplification to the Whole Phase

Before the theory of time-averaging the trigonometric functions of relevant angles and other essential input parameters could be adapted to the whole reel-out phase, the error of such an expansion should

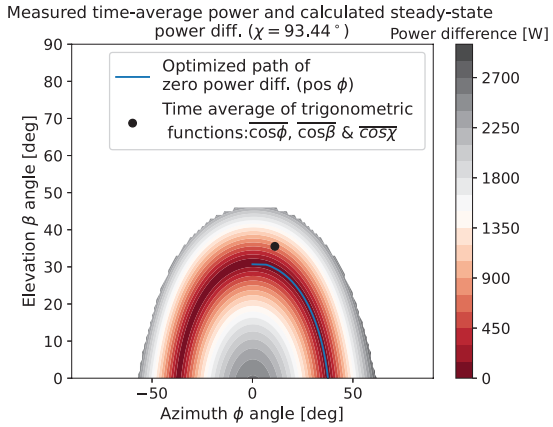

Figure 4.13: With fixed course angle the difference from measured time-average power various azimuth-elevation combinations would give for the third figure of the 56th cycle. The black dot is the time-averaged combination of angles.

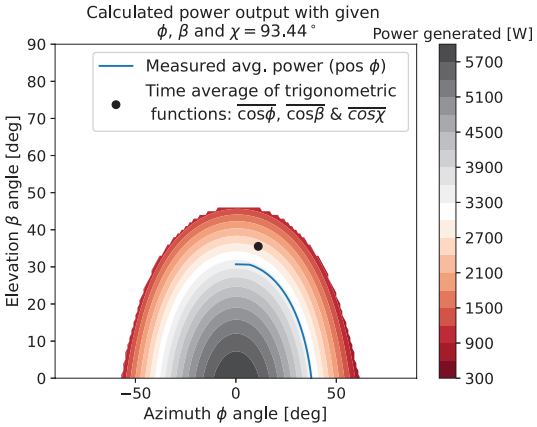

Figure 4.14: Different QSM output powers various azimuth-elevation combinations would give with fixed course angle. The black dot is the time-averaged combination of angles used for calculating the result in Table 4.5

be investigated. Whether only one point in the mid-radial distance of the reel-out phase, two points (one at the starting tether length, second at the ending tether length) or more radial locations should be used for power calculations is of interest. It is important to mention the angles at each radial distance are the same, only the tether length varies. This is shown in Figures 4.15 and 4.16.

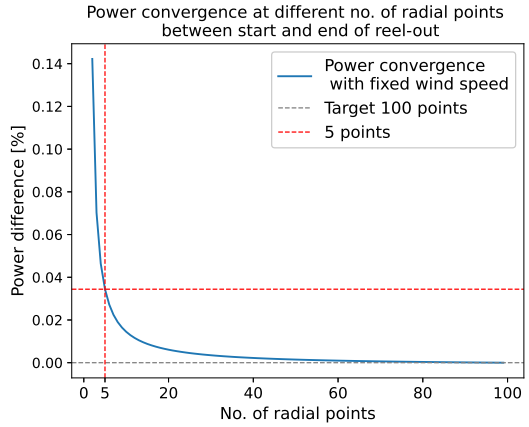

Figure 4.15: Power convergence with constant wind for heights between the start and the end of the reel-out phase. 5 radial points for the reel-out representation is enough and gives an average power accuracy of more than 99.9%

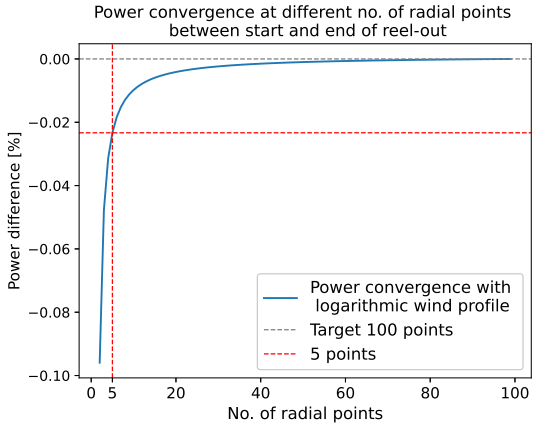

Figure 4.16: Power convergence with logarithmic wind for heights between the start and the end of the reel-out phase. 5 radial points for the reel-out representation is enough and gives an average power accuracy of more than 99.9%

Both of these graphs indicate how much the output power accuracy varies when a certain number of radial points are used for the calculation. 100 points are considered to give an absolute power value and fewer points give a power deviation from that threshold. In Figure 4.15 constant wind speed is kept for the altitudes between the start and the end of the reel-out phase. Figure 4.16 has logarithmically changing wind conditions with the altitude. From both graphs it could be noted the percentage wise difference is very small at already minimal radial points. 5 radial distances ensure the accuracy of power calculations at height-varying wind speeds is more than 99.9%. Therefore, this number is used for future calculations considering the whole reel-out phase.

By implementing the specified number of 5 radial distances and using the time-averaged measurement parameters as QSM inputs, the calculations are done for all the 86 reel-out phases. All the other QSM inputs are kept the same as introduced for the reference case in Section 4.1. The only differences are the use of a constant angle combination (Equations 2.60, 2.61 and 4.10) and an average reel-out speed for the whole phase. The QSM calculates output with the given set of 5 radial points and the

results are then averaged to a single power value. This value is compared to the time average power of the given phase received from the measurements using Equation 4.6. The results are plotted as Figure 4.17 and Table 4.6.

It turns out time-averaging the key QSM input parameters has a very little impact on the accuracy of power calculations. With kite flying the figure of eight from measurements the QSM has a small power underestimation on average (-0.6%) and in median (-3.9%). These values come from the reference simulation Table 4.4. Now with the averaged parameters the small underestimation has turned into a small overestimation of power. The median and average power have experienced 4-5% positive shift. Yet, the differences are marginal and the small positive trend should be validated with an alternative set of data.

Similar comparison between the QSM and the measurements can be made in the kite velocity calculated with

$$v_k = \sqrt{v_{k,\tau}^2 + v_{k,r}^2}, \tag{4.13}$$

where $v_{k,\tau}$ is the tangential kite velocity and $v_{k,r}$ the reel-out speed of the kite. Figure 4.18 and Table 4.6 present the results for that case. In v_k the QSM is showing underestimation compared to the measurements. A negative shift in the same parameter is experienced in comparison to the reference simulation as well. Since the reel-out velocity $v_{k,r}$ is the same in Figure 4.18 and 4.10 QSM cases where the phase average kite velocity is calculated the difference could originate only from $v_{k,\tau}$. This is calculated through λ and dependent on course angle χ. Apparently $\overline{\cos\chi}$ estimated $\chi \geq 90°$ calculates the kite to fly slower on tangential plane than it actually on average does. This χ is compensated by ϕ and β values which as a result of $\overline{\cos\phi}$ and $\overline{\cos\beta}$ are close to a downwind position. Only this way the generated power can increase while the kite velocity goes down. This observation should also be checked with an alternative set of measurements.

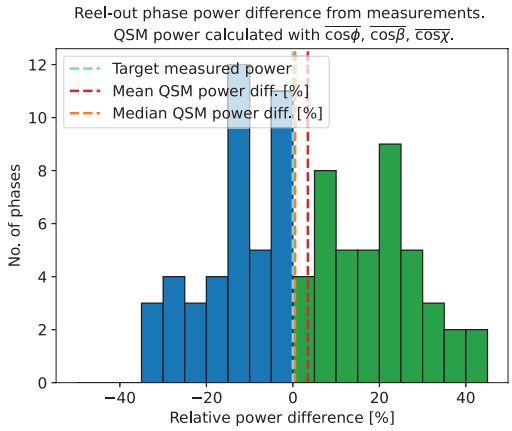

Figure 4.17: Relative power difference of measurement time-averaged reel-out power per phase vs steady-state power calculated using the QSM and the angles from time-averaged trigonometric functions $\overline{\cos(\phi)}$, $\overline{\cos(\beta)}$ and $\overline{\cos(\chi)}$ as an input.

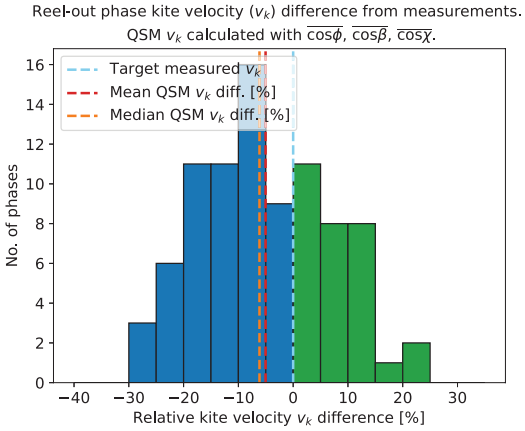

Figure 4.18: Relative kite velocity difference of measurement time-averaged reel-out v_k per phase vs steady-state v_k calculated using the QSM and the angles from time-averaged trigonometric functions $\overline{\cos(\phi)}$, $\overline{\cos(\beta)}$ and $\overline{\cos(\chi)}$ as an input

The same kite position vs speed of the kite idea is described with Figures 4.12 - 4.14. Applying this mathematical exercise here the QSM power accuracy of every single phase is improved. Keeping ϕ and β as given with Equations 2.60 and 2.61 but taking χ as an optimization variable is one way to do it. The optimization problem becomes

$$\min \left[P_{QSM}(\chi, \mathbf{a}) - P_{avg,m}\right]^2 \tag{4.14}$$

$$\text{subject to } \chi \in [-180°, 180°], \tag{4.15}$$

where $P_{avg,m}$ and P_{QSM} are the time-averaged power from the measurements and the power calculated with the QSM. The vector $\mathbf{a}$ includes fixed ϕ and β angles. Running this optimization for all the 86 cycles

Reel-Out Phase QSM Output Relative Diffreence from Meaurements Using Time-Averaged Coordinate Angles in QSM		
Parameter	**Method**	**Time-averaged phases**
Power	Median	0.516%
	Mean	3.470%
Kite velocity	Median	-6.150%
	Mean	-5.037%

Table 4.6: Power and kite velocity difference on average over all 86 reel-out phases between the measurements and using QSM with fixed angle combination for each of the reel-out phase.

the optimizer tends to increase the course angle as plotted in Figure 4.19. This can be explained with the following logic.

1. The kite generates the least power when flying upwards. The tangential kite velocity also goes down.

2. While keeping the other parameters fixed the smallest possible power production is reached therefore at course angle $\chi = 180°$.

3. Small power overestimation is experienced when all the angles originate from time-averaging the trigonometric functions of measurement coordinates.

4. By increasing the course angle this power overestimation could be reduced to zero.

Therefore, in Figure 4.19 the course angle difference by subtracting the previous time-averaged χ value from the optimized χ tends to be positive. The color bar in Figure 4.19 has more positive differences since the distribution of power overestimated reel-out phases is wider than for the underestimated phases. This is observed from Figure 4.17 where the overestimation green bars reach 45% whereas the underestimation blue bars have a maximum at 35%.

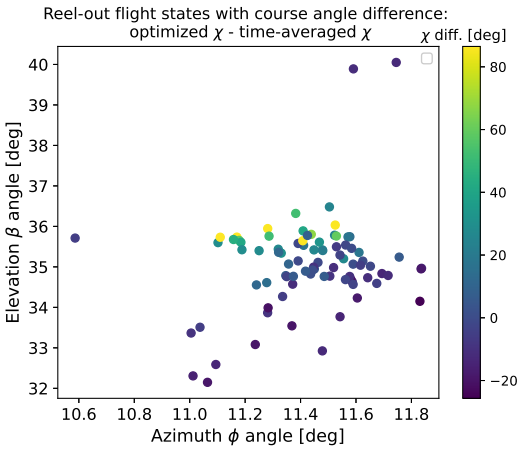

Figure 4.19: Reel-out flight states of azimuth and elevation angle calculated using the time-averaged trigonometric functions $\overline{\cos\phi}$ and $\overline{\cos\beta}$. The color bar shows the difference in course angle when the latter is calculated using $\overline{\cos\chi}$ or optimized for reaching the target power output. Positive difference shows $\overline{\cos\chi}$ results in overestimation of output power. Therefore, if average reel-out power from measurements becomes the target value the optimizer increases course angle to reduce the steady-state power and vice versa.

Based on the optimization and the concept of using a fixed combination of angles in the QSM calculation various observations and conclusions could be drawn.

- The concept does not have significant impact on the mean output power accuracy compared to the reference simulation (+4.1%). This rule applies on average power. The statement should be checked with an alternative set of measurements.
- The small deviations in accuracy result in increased output power but decreased velocity of the kite when substituting the measurement coordinates with a fixed angle combination in the QSM. This is possible if the kite flies slower but is positioned closer to the downwind direction.
- By fixing the azimuth and elevation angles and optimizing the course angle for zero power difference from the target measurement time average power one could get the same power results with the QSM. However, this type of modification of χ is not justified for the future power estimations with the QSM since it compensates the inaccuracy of other QSM inputs without solving the incorrect simplifications themselves.
- The approach requires existing measurements where the calculations could be based on.

4.2.2. Parameterizing Reel-Out Figure of Eight

An alternative way of describing the traction phase to what is used in Section 4.2.1 is to fly the reel-out figures of eight. However, the measured figures are asymmetrical and different from each other without any equation describing them. This makes it difficult to reproduce these figures for future power estimations. A solution would be to select a general case of figure of eight which could be plotted using a mathematical equation and modify it with certain parameters to have a better match with the shapes from the measurements. This way connections between the environmental conditions and these modifying parameters could be drawn and the base shape of figure of eight, given by an equation, can be used for future energy yield predictions. The accuracy of such results, based on artificially reproduced figures, solely depends on how good is the fit to an actual flight path. In other words, the modifying parameters must be optimal, meaning the number of parameters should be enough to describe the asymmetric shape but minimal to keep the figure relatively simple and time-saving from the perspective of computations.

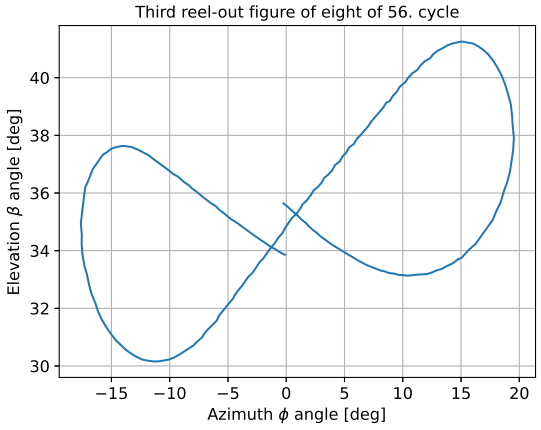

Figure 4.20: Measured third figure of eight from the 56th reel-out phase

For this purpose, two different approaches for flight data fitting are introduced here. The target measurement figure of eight is plotted in Figure 4.20. Both of these fitting methods are based on the general shape of figure of eight called the lemniscate. The concept is to place a symmetric figure of eight to a measured shape and introduce the asymmetries to lemnsicate with an attempt of reducing the geometrical azimuth and elevation difference between the two figures.

The first fitting approach tries to modify the lemniscate shape directly using constant parameters. These parameters are included in the general equation of lemniscate and could be found via optimization.

The second approach introduces a shape function in the fitting process. The lemniscate is considered as a general class function which defines the symmetric figure of eight. The shape function adds

the asymmetric properties to the figure. The multiplication of the shape and class function leads to a fitted figure of eight. In this case the optimization variables are the shape function parameters.

Optimizing the Parametric Equation of Generalized Lemniscate
In mathematics the eight curve is also known as lemniscate of Gerono. This symmetric shape could be given in a generalized form as

$$x^4 = a^2(x^2 - y^2) \tag{4.16}$$

in Cartesian coordinates or be presented as parametric equations

$$x = a \sin t \tag{4.17}$$
$$y = a \sin t \cos t \tag{4.18}$$

where $t \in [0, 2\pi]$. [27] If $a = 1$ Equation 4.16 becomes

$$x^4 - x^2 + y^2 = 0 \tag{4.19}$$

and the initial form of lemniscate of Gerono could be plotted as in Figure 4.21.

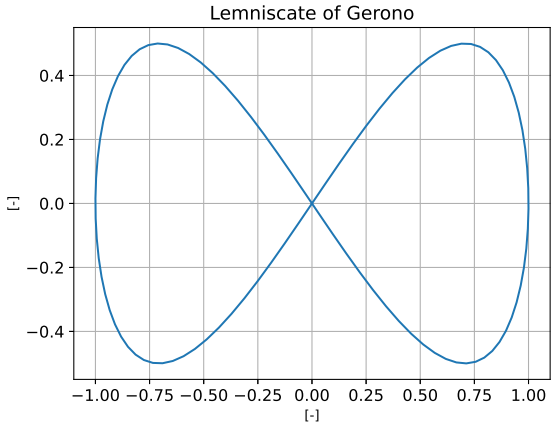

Figure 4.21: Lemniscate of Gerono

This figure of eight can be easily reproduced and x-y coordinates passed to the steady-state calculations as azimuth ϕ and elevation β in radians. However, this simple figure is off by size when compared to the measurement geometry in Figure 4.20 and does not reflect the asymmetric properties (e.g. not skewed). Therefore, the original Equation 4.16 requires additional parameters to make it a more generalized case of lemniscate suitable for fitting purposes.

To tilt the figure another xy term is introduced. Additionally, by looking at Figure 4.20 the left and the right lobe of the measurement shape are not the same by size. To apply for this asymmetric property x^3 term is required. In a symmetric and regular lemniscate both of these new terms would be equal to zero ($xy = 0$ and $x^3 = 0$). Weights different than initial symmetric conditions have a shape-changing impact. The more the weight deviates from the initial condition the more dominantly is the figure influenced by this particular term. The expanded lemniscate equation together with the weights looks as follows:

$$ax^4 - bx^2 + cy^2 + dxy + ex^3 = 0. \tag{4.20}$$

This equation has the right amount of flexibility for figure of eight fitting. The shape could be changed in size in horizontal and vertical axis, be tilted and have one lobe larger than the other. As the last addition the centre point coordinates of lemniscate are adjusted. The new form of Equation 4.20 may mimic the shape of figure of eight but around the origin point of axes (O), meanwhile in reality the kite flies figures in the sky around centre with different azimuth and elevation coordinates. This means the horizontal

centre point adjusting coefficient c_1 and the vertical adjusting coefficient c_2 are added to Equation 4.20. The finalized form becomes

$$a(x-c_1)^4 - b(x-c_1)^2 + c(y-c_2)^2 + d(x-c_1)(y-c_2) + e(x-c_1)^3 = 0. \tag{4.21}$$

This generalized lemniscate equation has enough flexibility to fit the reel-out figure of eight to measurements. [22]

The fitting is done as a SLSQP (description in Appendix A) minimization optimization problem with optimization variables $(a,\ b,\ c,\ d,\ e,\ c_1,\ c_2)$ and Equation 4.21 as an optimization function. The idea is to pass azimuth ϕ as x and elevation β as y to the optimizer and find $(a,\ b,\ c,\ d,\ e,\ c_1,\ c_2)$ combination that would minimize the residuals (right-hand side of function) in Equation 4.21 in as many as possible occasions. In other words the problem becomes

$$\min F(x, y, (a, b, c, d, e, c_1, c_2)), \tag{4.22}$$

where $x = \{x_1, ..., x_n\}$ and $y = \{y_1, ..., y_n\}$ are series of azimuth and elevation parameters from the measurements and F denotes the sum of squared function f values. [12]

This type of optimization requires certain boundaries for the optimization variables in order not to lose the characteristic shape of lemniscate. The search space is investigated to understand how each one of these weight parameters influences the shape of the figure and to determine suitable boundaries. Figures 4.22-4.29 show the impact of each weight parameter which will be discussed in detail hereafter.

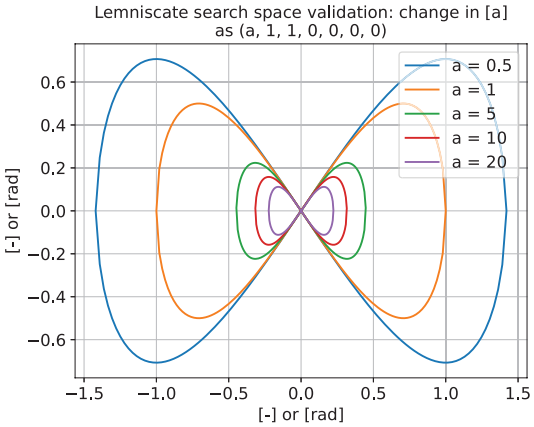

Figure 4.22: Change of [a] in generalized lemniscate

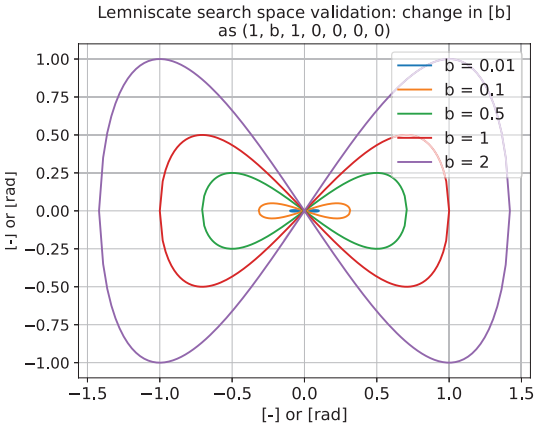

Figure 4.23: Change of [b] in generalized lemniscate

Change in weights a and b have both impact on the characteristic size of the lemniscate as shown in Figures 4.22 and 4.23. Parameter a maintains the horizontal and vertical ratio whereas changes in b have more vertical impact on the shape compared to the horizontal direction. An important note is that smaller shape is obtained when a increases whereas b has similar effect with decreasing values. Since figures of eight from the data are usually between $\sim [-0.3, 0.3]$ rad, the original shape of lemniscate needs to shrink. Based on the observations the defined boundaries are $a \in [0.1, 20]$ and $b \in [0.01, 5]$.

Parameter c only changes vertical properties of figure, maintaining the horizontal size. This is shown in Figure 4.24. The essence of vertical modification becomes obvious when looking at the measurement figure of eight (Figure 4.20). The measured shape has much narrower lobes in vertical direction than the original lemniscate of Gerono. Nevertheless, parameter b has also a notable impact on the shape in vertical direction, meaning the combination of b and c may lead to a magnifying function required from c. From these observations the c boundaries are set wide $c \in [0.1, 50]$. The letter c is also used for denoting the centre point coordinates of the lemniscate. As shown in Figure 4.25 c_1 is used for centre point azimuth adjustments and c_2 for changing the elevation of figure of eight without having any impact on the shape itself. Since azimuth is physically limited with $[-\frac{\pi}{2}, \frac{\pi}{2}]$ rad and elevation with $[0, \frac{\pi}{2}]$ rad these are set as the boundary conditions for c_1 and c_2 respectively.

Parameters d and e represent the weights for extra terms added to the generalized Equation 4.16 of lemniscate. They are responsible for the asymmetrical changes in the shape. As could be noted in Figures 4.26 and 4.27 the parameter d changes the tilt in vertical direction. Positive d values raise the

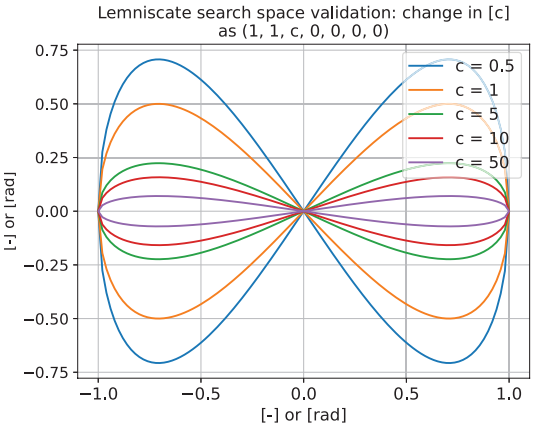

Figure 4.24: Change of $[c]$ in generalized lemniscate

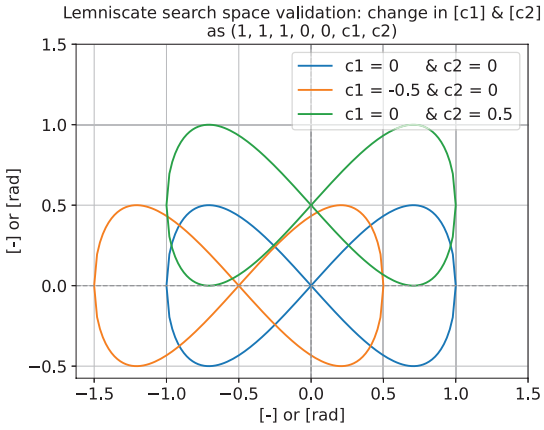

Figure 4.25: Change of $[c_1]$ and $[c_2]$ in generalized lemniscate

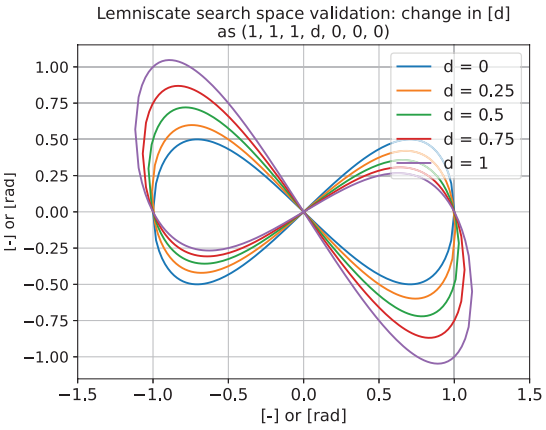

Figure 4.26: Change of $[d]$ in positive direction in generalized lemniscate

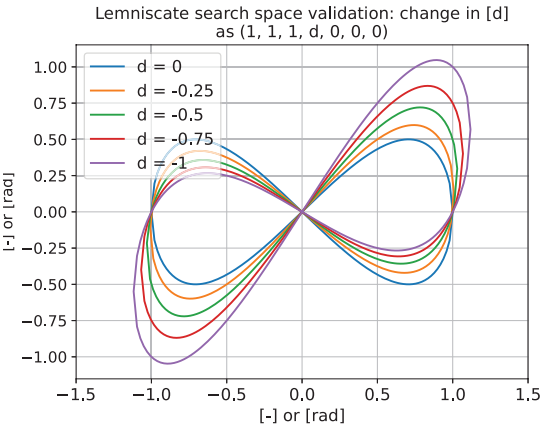

Figure 4.27: Change of $[d]$ in negative direction in generalized lemniscate

left lobe above the right one and vice versa. Because in reality the reel-out figure of eight has right and left lobe difference smaller than 0.1 rad only small d values are required and the boundary is set to be $d \in [-0.5, 0.5]$. Similar logic could be applied to the size difference between the lobes (Figures 4.28 and 4.29). One lobe is never more than twice the size in vertical direction compared to the other one and the boundary for e could be $e \in [-0.5, 0.5]$.

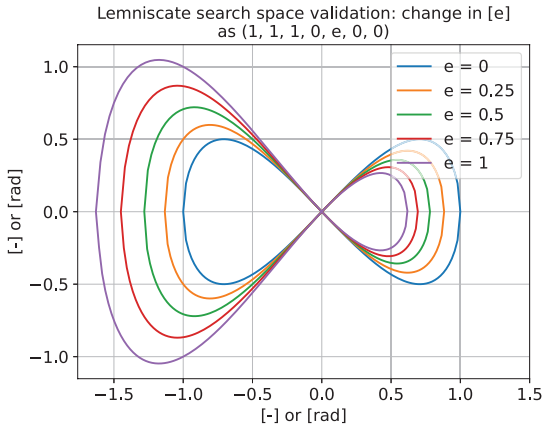

Figure 4.28: Change of $[e]$ in positive direction in generalized lemniscate

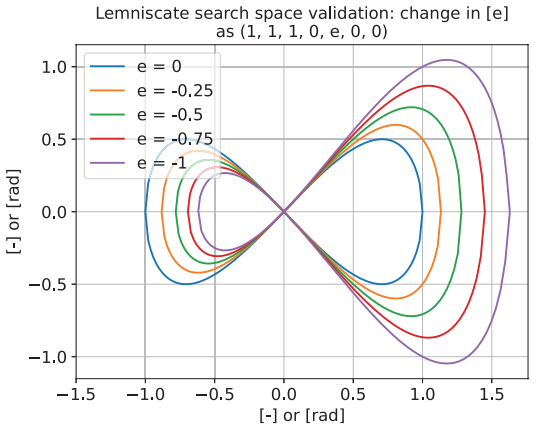

Figure 4.29: Change of $[e]$ in negative direction in generalized lemniscate

Combining the boundaries for weight parameters $(a,\ b,\ c,\ d,\ e,\ c_1,\ c_2)$ the following optimization problem is formed

$$\min \sum_{n=1}^{i} [f(\phi_n, \beta_n, a, b, c, d, e, c_1, c_2)]^2 \tag{4.23}$$

$$\begin{aligned} \text{subject to } & a \in [0.1, 20],\ b \in [0.01, 5],\ c \in [0.1, 50] \\ & d \in [-0.5, 0.5],\ e \in [-0.5, 0.5] \\ & c_1 \in \left[-\frac{\pi}{2}, \frac{\pi}{2}\right],\ c_2 \in \left[0, \frac{\pi}{2}\right], \end{aligned} \tag{4.24}$$

where f is the generalized function of lemniscate (Equation 4.21), ϕ_n and β_n are the azimuth and elevation pairs from the measurements for the given figure of eight and i is the number of measurement instances. This optimization problem is solved using the SLSQP algorithm.

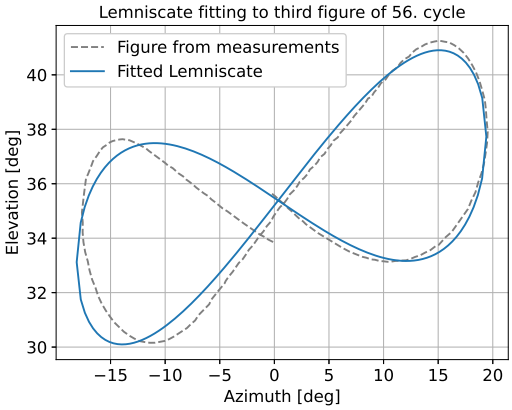

Figure 4.30: Lemniscate fitting to the third figure of eight from the 56th cycle

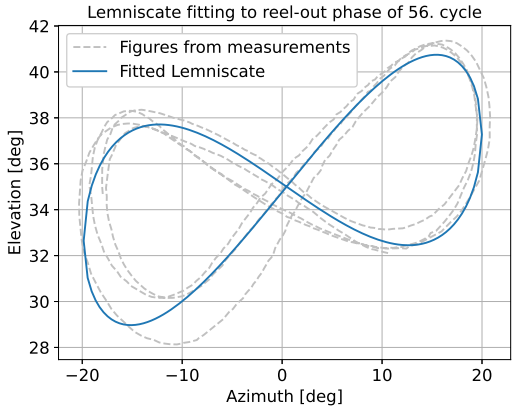

Figure 4.31: Lemniscate fitting to the reel-out phase of the 56th cycle (three figures)

Parameters of Lemniscate Fitting of the 56th Reel-Out Phase								
	a	b	c	d	e	c_1	c_2	Objective f. value
Third figure	2.482	0.240	1.716	-0.422	-0.027	0.006	0.618	0.0005
Whole phase	2.540	0.283	1.746	-0.406	0.033	0.008	0.611	0.0061

Table 4.7: The weight parameters of fitting lemniscate of Gerono to the third reel-out figure of eight or to the whole traction phase of the 56th cycle

The results obtained with fitting to the traction phase of the 56th cycle or to the third figure of eight from the same phase are plotted in Figures 4.30 and 4.31. The corresponding weight parameters could be seen in Table 4.7. For a single figure fitting the azimuth and elevation pairs are passed to the optimizer about one figure of eight. For the whole reel-out phase fitting the coordinates of three figures are given as a list. What can be observed from Figure 4.30 is that the fitted lemniscate matches relatively well to the right lobe but has some fitting problems with the left one. Since the measured figure of eight is not connected at the centre the optimizer has issues finding a suitable location for the centre point. This causes geometrical deviations of fitted figure from the measurement shape. Another figure of eight fitting technique is investigated hereafter which could potentially give better results. The QSM output power when flying the fitted figures comparison to the measurements is done for the method that provides a better fit out of two techniques. This is done in the end of this section.

Optimization Using Universal Parametric Geometry Representation Method

The second approach for figure of eight fitting involves the universal parametric geometry representation method or in other words the class function/shape function transformation technique (CST) that has been developed to reduce the number of coordinates and variables required to describe specific geometries. The idea is to form figures using a combination of class and shape function. The class function has a purpose of defining general classes of geometries, whereas for describing the specific shapes in a geometry class the shape function is used. The resultant multiplication of the class and the shape function gives the desired geometry output. [10]

To describe the general reel-out figure of eight, lemniscate of Gerono carries the essential characteristics to fulfill the class function requirements. It is general enough to be the basis shape for modifications which would give the actual figure of eight. The class function lemniscate with parametric Equations 4.17, 4.18 and $a = 1$ is shown in Figure 4.32.

To introduce the asymmetric properties in class function, the shape function is used. Every shape function should have an initial condition of 1, which by multiplying with the class function gives an output geometry equal to the latter. Additionally, the shape function should carry enough flexibility for various modifications. Bernstein polynomials are commonly used to form the shape function. These polynomials are given by equation

$$B_{i,n}(t) = \binom{n}{i} t^i (1-t)^{(n-i)}, \tag{4.25}$$

where $\binom{n}{i}$ is a binomial coefficient, n denotes the order of polynomials, i is the number of that particular polynomial between 0 & n and $t \in [0, 1]$ are the points on the horizontal axis which serve as an input to the function. Figure 4.33 shows an example of order 4 Bernstein polynomials. The shape function is the sum of these polynomials. This sum is 1 if the weight of each polynomial is 1, meaning the polynomials are not modified. [15]

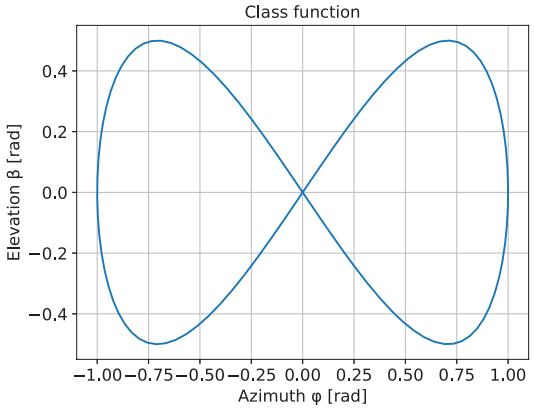

Figure 4.32: Class function lemniscate (lissajous) for the CST method

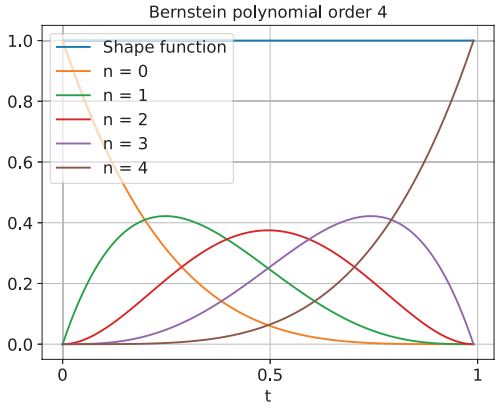

Figure 4.33: Bernstein polynomial makes up a shape function used for the class function modification in the CST method

Bernstein polynomials are generally a good tool for shape function formulation but not all polynomials of them are periodical in a certain range of $t \in [0, 1]$, meaning the first derivative at $t = 0$ and $t = 1$ is 0 for only one or few polynomials depending on the polynomial order chosen. Non-periodical polynomials in shape function for lemniscate modification could lead to unexpected kinks in the curve. Figure 4.34 shows the only periodical Bernstein polynomial out of order 4 polynomials. This $n = 2$ polynomial that peaks at $t = 0.5$ is the only Bernstein polynomial used here for smooth figure of eight fitting. One could observe that it is also symmetrical from the vertical axis and not coupled to any other polynomial, enabling the one-by-one addition of polynomials.

Since a single polynomial is not enough to form the shape function, a new method for shape function formulation is developed here. As a first step the width of the chosen polynomial is reduced by a half. This way the polynomial could have more local impact on the figure. Secondly, multiples of polynomial are made and shifted evenly from the original position. Ten polynomials shifted with an interval of $0.1t$ are formed. The number ten is conservatively selected here to prepare the fitting method for even the

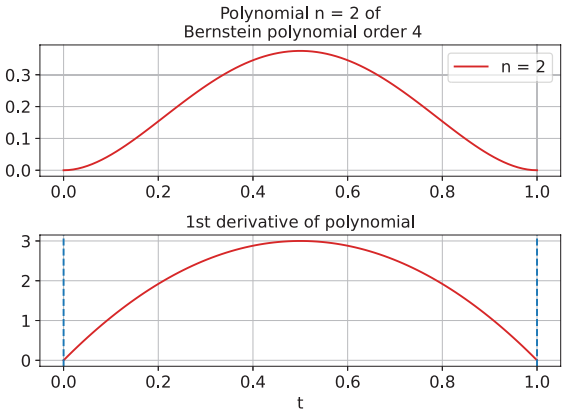

Figure 4.34: The periodical Bernstein polynomial $n = 2$ which has the first derivative equal to 0 at $t = 0$ and $t = 1$

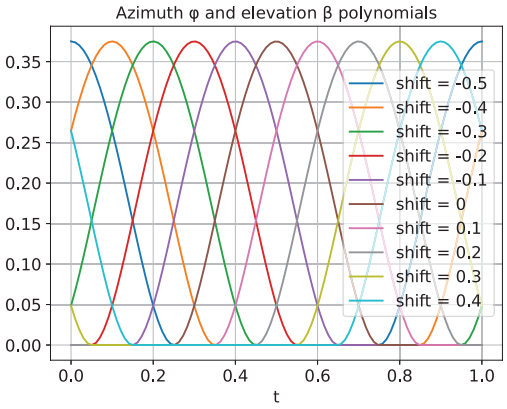

Figure 4.35: Shifted Bernstein polynomial $n = 2$ of order 4 polynomials. The curve is shifted from the centre ($t = 0.5$) with even steps of $0.1t$.

most asymmetrical figures of eight. One could change this number based on the shape of measurement figure if computational speed is of relevance. These ten polynomials are plotted in Figure 4.35. Looking at the class function parametric Equations 4.17 and 4.18 which could be written as

$$x = a \sin(t * 2\pi) \tag{4.26}$$

$$y = a \sin(t * 2\pi) \cos(t * 2\pi), \tag{4.27}$$

where $t \in [0, 1]$ is the same t used for polynomial plotting and a defines the width and height of a single lobe, then both lobes of figure of eight have equally 4 polynomials for modification and 2 polynomials are peaking at the centre. This means the lemniscate plotting goes through the centre when $t = 0$ and $t = 0.5$ and the maximum and minimum azimuth values are plotted when $t = 0.25$ and $t = 0.75$ respectively.

When the shape smoothness issues are believed to be resolved with the new combination of ten polynomials another problem occurs. The summation of modified polynomials does not equal 1 as it is for the full set of Bernstein polynomials. This could be solved by making the initial weights of polynomials 0 and adding 1 to form the default shape function (N). The calculation of the latter goes now as

$$N = \mathbf{w} \cdot \mathbf{p} + 1, \tag{4.28}$$

where $\mathbf{w}$ is a vector of weights and $\mathbf{p}$ a matrix of polynomials. The shape function with a value of 1 does not make any changes to the geometry defined by the class function. If the weights deviate from 0 the original shape function value changes and the output of class and shape function multiplication is also modified, introducing the asymmetries to the geometry.

Before investigating how changes in the newly defined shape function have impact on the outputs of CST, final modifications to class function parametric equations should be implemented. First of all, the Equations 4.26 and 4.27 plot first the right-hand lobe (positive azimuths) of figure of eight and then the lobe on the left (negative azimuths). Inversely the kite according to the measurement data flies first the left lobe (negative azimuths) before moving to the right one. This becomes relevant when optimization problem for fitting is set. Fortunately, the class function can be easily flipped by adding minus sign to x (or ϕ) term. Secondly, the optimizer would have more options to make a better fit to the measurement reel-out figure of eight if the height and the width of the class function could be modified as extra parameters. The same goes for the lemniscate centre point adjustments which could lift the shape to comparable elevations with the measurement figure. Making these changes the parametric equations of the class function become

$$\phi_c = -a_\phi \sin(t * 2\pi) + c_\phi \tag{4.29}$$
$$\beta_c = b_\beta \sin(t * 4\pi) + c_\beta, \tag{4.30}$$

where a_ϕ denotes half of the class function maximum width (or width of a single lobe) and b_β marks half of the class function maximum height. These parameters are measured in rad. For the class function example shown in Figure 4.32 these values are $a_\phi = 1$ and $b_\beta = 0.5$. The coefficients c_ϕ and c_β are the lemniscate centre point coordinates. For the example case these values are $(0, 0)$.

With the presented theory about forming the class function (Equations 4.29 and 4.30) and calculating the shape function (Equation 4.28) a minimization optimization problem could be set up. According to Appendix A the idea is to minimize the sum of squared differences between the fitted and the measurement figure. For a more accurate fit both the azimuth ϕ and elevation β coordinates of the class function are modified with a separate set of polynomials (set for ϕ & set for β). This is somewhat different than in previous parametric equation optimization technique where ϕ and β coordinates originate from the measurements and the residue of Equation 4.21 is minimized. Now, an extra parameter which links the measurement ϕ and β to the CST output ϕ and β is required. This parameter t is already in use in the class function Equations 4.29 and 4.30 but is missing from the measurements. Path length S of the measured figure of eight is used to find the values of t for the measurement figures. This S is a cumulative sum of

$$\begin{aligned} S_0 &= 0 \\ S_{n+1} &= S_n + \sqrt{(\phi_{n+1} - \phi_n)^2 + (\beta_{n+1} - \beta_n)^2}, \end{aligned} \tag{4.31}$$

where S_n is the path length of figure of eight up to that point n. The last element S_f in this array gives the total path length of figure of eight. The parameter t which belongs to $t \in [0, 1]$ could also be considered as a completion rate. The starting path length S_0 corresponds to $t = 0$ and the final path length S_f to $t = 1$. All the t values are calculated as

$$t = \left[\frac{S_0}{S_f}, \frac{S_1}{S_f}, ..., \frac{S_f}{S_f}\right]. \tag{4.32}$$

This array of t values is passed to the class function parametric Equations 4.29 and 4.30 to calculate the corresponding ϕ_c and β_c values. These values are modified with the shape function to get ϕ_{CST} and β_{CST} which could be compared to measured ϕ_m and β_m for the same completion rate t. For fitting the SLSQP is used.

Counting all the parameters together the optimization gets a total of 24 optimization variables. The shape function Equation 4.28 can be used for both azimuth and elevation changes. These two shape functions are denoted as N_ϕ and N_β respectively and both of them have ten polynomials with ten different weights w. The 20 weights all together make 20 optimization variables. The four missing variables from the complete set come from the class function Equations 4.29 and 4.30 where the optimizer could find suitable values for a_ϕ, b_β, c_ϕ and c_β. Since the weights do not have any restrictions in this type of fitting it is difficult to find any boundaries for them. However, to keep the optimizer from placing the class function at an arbitrary non-feasible location for figure of eight flight (out of the wind sphere, below the ground) and then modifying it with a dominant shape function to bring the figure back to the feasible region, one could define boundaries for class function variables. The figures of eight from the measurements are hardly ever wider than 60° which sets a_ϕ boundaries using $a_\phi = width/2$ to $a_\phi \in [0, 0.5]$ rad. The value for b_β is usually two times smaller than a_ϕ and the bounds could be written as $b_\beta \in [0, 0.25]$. The figure of eight cannot leave the downwind sphere and the centre point of the class function is therefore restricted with $c_\phi \in \left[-\frac{\pi}{2}, \frac{\pi}{2}\right]$ and $c_\beta \in \left[0, \frac{\pi}{2}\right]$. Together with the bounds the optimization problem can be stated as

$$\min \sum_{t=0}^{1} \left[(\phi_{CST,t} - \phi_{m,t})^2 + (\beta_{CST,t} - \beta_{m,t})^2 \right] \tag{4.33}$$

$$\text{with } [w_{\phi,1}, ..., w_{\phi,10}, w_{\beta,1}, ..., w_{\beta,10}, a_\phi, b_\beta, c_\phi, c_\beta]$$

$$\text{subject to } a_\phi \in [0, 0.5],\ b_\beta \in [0, 0.25] \tag{4.34}$$

$$c_\phi \in \left[-\frac{\pi}{2}, \frac{\pi}{2}\right],\ c_\beta \in \left[0, \frac{\pi}{2}\right],$$

where $\phi_{CST,t}$ & $\beta_{CST,t}$ are the CST calculated coordinates at the given t and $\phi_{m,t}$ & $\beta_{m,t}$ are the measurement values. It is important to mention that t is in reality a continuous function between $[0, 1]$ but the steps are defined by the measurement instances. In principle the corresponding CST coordinates $\phi_{CST,t}$ & $\beta_{CST,t}$ to t would be the result of a simple class and shape function multiplication. However, figures of eight from the measurements tend to cross $\phi = 0$ rad at some points. This has an impact on the CST results since the shape function cannot have any shape-changing impact on these points due a multiplication with zero. Another CST method modification is introduced here step-by-step to overcome this problem.

1. Class function without any parameters a_ϕ, b_β, c_ϕ and c_β is used first. This class function is shifted with an arbitrarily selected value Δ to avoid any lemniscate zero crossings.

$$\phi_{c,\Delta,t} = -\sin(t * 2\pi) + \Delta \tag{4.35}$$

$$\beta_{c,\Delta,t} = \sin(t * 4\pi) + \Delta \tag{4.36}$$

2. Then the shifted class function is multiplied with the shape function as

$$\phi_{\Delta,t} = (\phi_{c,\Delta,t})(N_{\phi,t}) \tag{4.37}$$

$$\beta_{\Delta,t} = (\beta_{c,\Delta,t})(N_{\beta,t}), \tag{4.38}$$

   where the shape functions (N) are calculated using Equation 4.28.

3. The displaced positions are shifted back to the origin of coordinates.

$$\phi_{O,t} = \phi_{\Delta,t} - \Delta \tag{4.39}$$

$$\beta_{O,t} = \beta_{\Delta,t} - \Delta \tag{4.40}$$

4. The final CST output could be received when bringing the class function parameters into the calculations.

$$\phi_{CST,t} = (a_\phi)(\phi_{O,t}) + c_\phi \tag{4.41}$$

$$\beta_{CST,t} = (b_\beta)(\beta_{O,t}) + c_\beta \tag{4.42}$$

The defined minimization problem with Equation 4.33 is practiced on the measured reel-out phase of the 56th cycle. Fitting is done for the third figure of eight of the given phase as well as for the whole phase. For the single figure case $\phi_{m,t}$ and $\beta_{m,t}$ values together with the completion rate t for only the third figure of eight are passed to the optimizer. The class and shape function of this optimization can be seen as Figures 4.36 and 4.37. These functions are achieved with parameters presented in column ”Figure” in Table 4.8 and the objective function value with optimized weights is given in Table 4.9. The latter is used in the end of this section to select the best fitting technique for the expansion to the whole set of 86 measurement cycles.

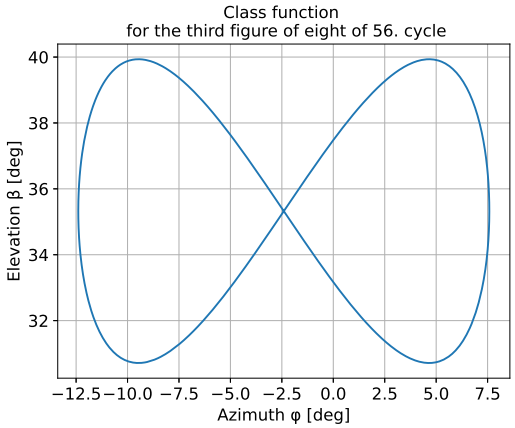

Figure 4.36: Class function for the third figure of eight fitting of the 56th cycle

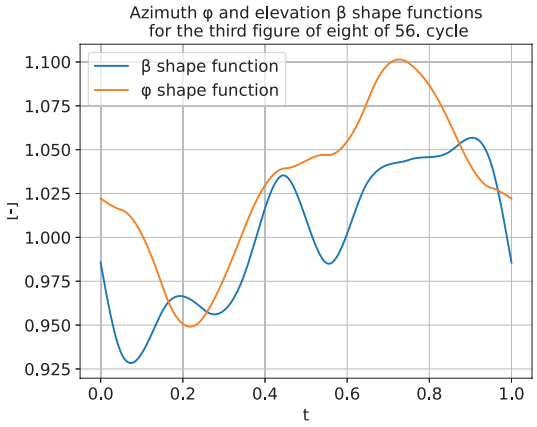

Figure 4.37: Shape function for the third figure of eight fitting of the 56th cycle

The multiplication of the class and the shape function results in a fitted figure of eight plotted in Figure 4.38. As it could be visually observed the CST method gives a relatively good fit to the measured figure of eight. The problematic left lobe fitting that occurred in the parametric equation direct optimization one can see in Figure 4.30 is disappeared. Yet, there is a sharp turn in the fitted figure at the loose ends of the measured figure of eight. The biggest error between the measured and the fitted figure situates indeed at the end value of $t = 1$ as it is shown in the error plot in Figure 4.39. This sharp turn is believed to be smoothened if more figures are included in the optimization since the end of measured figure of eight serves as a starting point for the next figure and the curve is continuous.

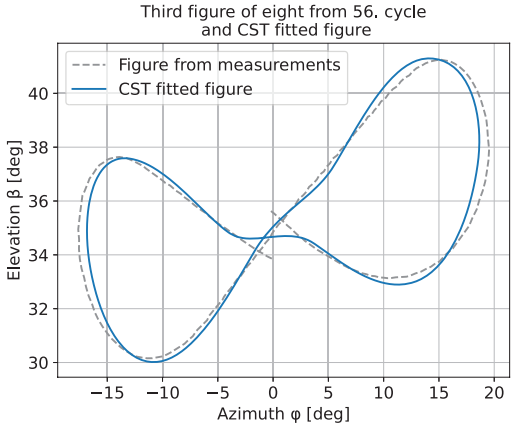

Figure 4.38: Measured and CST fitted third figure of eight of the 56th cycle

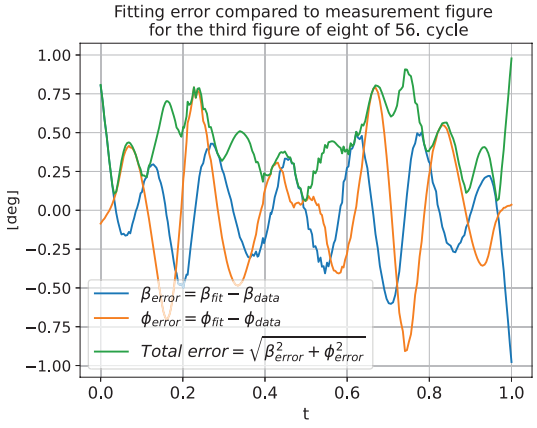

Figure 4.39: Fitting error in azimuth and elevation direction for the third figure of eight of the 56th cycle

As a following step the CST method is expanded to the whole reel-out phase of the 56th cycle. Now the difference is the optimizer takes three figures of eight simultaneously as optimization inputs instead of one. The boundaries previously set remain the same but the objective function changes from Equation 4.33 to

$$\min \sum_{t=0}^{1} \sum_{n=1}^{3} \left[(\phi_{CST,t} - \phi_{m,n,t})^2 + (\beta_{CST,t} - \beta_{m,n,t})^2 \right] \tag{4.43}$$

$$\text{with } [w_{\phi,1}, \ldots, w_{\phi,10}, w_{\beta,1}, \ldots, w_{\beta,10}, a_\phi, b_\beta, c_\phi, c_\beta]$$

$$\text{subject to } a_\phi \in [0, 0.5],\ b_\beta \in [0, 0.25] \tag{4.44}$$

$$c_\phi \in \left[-\frac{\pi}{2}, \frac{\pi}{2}\right],\ c_\beta \in \left[0, \frac{\pi}{2}\right],$$

where $\phi_{m,n,t}$ and $\beta_{m,n,t}$ are the measured coordinates of the nth figure in the reel-out phase. Running the optimization with Equation 4.43 the class function in Figure 4.40 and the two shape functions in Figure 4.41 are received. A relevant observation is that the class function is not centering close to $\phi = 0°$. This is the result of Δ shift which has an impact on how the optimizer chooses a_ϕ, b_β, c_ϕ and c_β values. This class function is plotted using Equations 4.29 and 4.30 but in the optimization process the class function is shifted by $\Delta = 1$ rad.

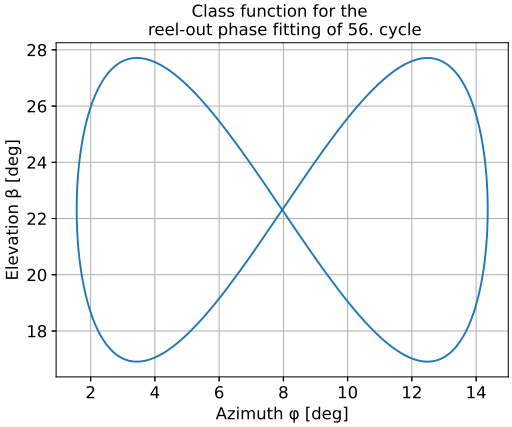

Figure 4.40: Class function for the whole reel-out phase fitting of the 56th cycle

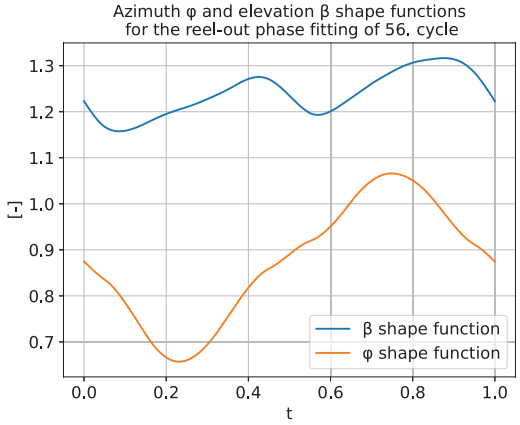

Figure 4.41: Shape functions for the whole reel-out phase fitting of the 56th cycle

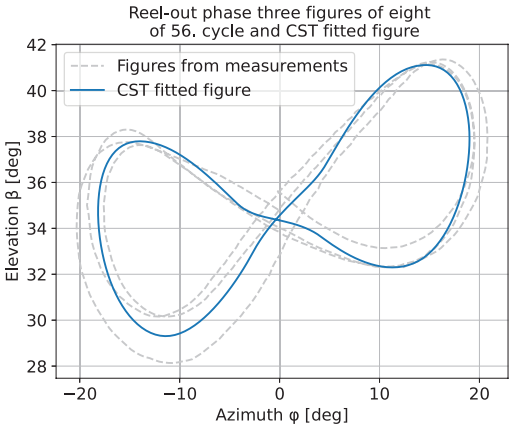

Figure 4.42: Measured and CST fitted figure for the whole reel-out phase of the 56th cycle

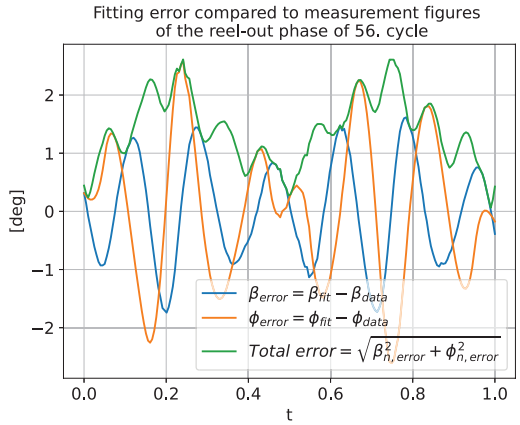

Figure 4.43: Fitting error in azimuth and elevation direction for the reel-out phase of the 56th cycle

The fitting using the CST method results in a figure of eight that is shown as Figure 4.42. As expected the sharp turn in the centre of the figure is smoother than in the fit for a single figure. Otherwise, the figures look visually similar. Due the fact that the errors from three figures are summed up as in Equation 4.43 the total error shown in Figure 4.43 increases in comparison to the single figure fitting. The error peaks around $t = 0.25$ and $t = 0.75$ when the kite is flying the furthest azimuth points from the centre. This error is mainly caused by one measurement figure which is wider than the two alternative paths. One could clearly observe the ϕ_{error} has the biggest share in the total error at these points. The square of the total error parameter is used in the following comparison with the parametric equation fitting technique in order to choose a suitable method for the reel-out phase power calculations considering all the 86 measurement cycles.

Power and Kite Velocity Calculations Using Fitted Figures of Eight

The power calculations for the whole set of measurement cycles are conducted using the method with the best fit. The criterion for defining the best fit is to calculate which one of the fitting approaches has

Parameters of CST Fitting of the 56th Reel-Out Phase											
	Figure	**Phase**		**Figure**	**Phase**		**Figure**	**Phase**		**Figure**	**Phase**
$w_{\beta,1}$	-0.0134	0.1857	$w_{\beta,7}$	0.3326	0.4290	$w_{\phi,3}$	-0.0795	-0.4278	$w_{\phi,9}$	0.1437	0.1562
$w_{\beta,2}$	0.3121	0.4084	$w_{\beta,8}$	-0.6592	-0.2714	$w_{\phi,4}$	-0.1463	-0.5115	$w_{\phi,10}$	-0.0956	-0.2140
$w_{\beta,3}$	-0.7440	-0.3126	$w_{\beta,9}$	0.7978	0.8822	$w_{\phi,5}$	0.1930	0.0435	c_{ϕ}	-0.0420	0.1390
$w_{\beta,4}$	0.7104	0.7370	$w_{\beta,10}$	-0.3573	0.0663	$w_{\phi.6}$	0.0091	-0.1157	c_{β}	0.6165	0.3894
$w_{\beta,5}$	-0.5040	0.0048	$w_{\phi,1}$	0.1055	-0.0471	$w_{\phi,7}$	-0.0520	-0.2439	a_{ϕ}	0.1744	0.1117
$w_{\beta,6}$	0.1418	0.2600	$w_{\phi,2}$	0.0178	-0.1432	$w_{\phi,8}$	0.2095	0.2382	b_{β}	0.0805	0.0943

Table 4.8: The values of optimization variables for CST fitting. The process is done for the third figure of eight of the 56th cycle and the whole reel-out phase. Single figure fitting parameters are marked in column ”Figure” and phase fitting parameters in column ”Phase”. The numbers are given in [rad].

the smallest fitted figure difference in both azimuth ϕ and elevation β compared to the measurement figure of eight. In the CST method the sum of the squared ϕ and β errors is the objective function to be minimized. These objective function values with optimized parameters are presented in Table 4.9 in rows considering the ”CST method”. In contrary, this error value is missing from the technique involving the use of weight parameters directly on the parametric equation of figure of eight. This method is described in the previous subsection and the minimized residue of the function in Equation 4.23 cannot be directly considered as the error parameter in ϕ and β. Therefore, the error requires additional calculation after the optimization process is finished.

One could define the fitted figure azimuth and elevation values at certain completion rate t similarly to the measurement figures. This invloves the calculation of path length with Equation 4.31 followed by defining the completion rate vector with Equation 4.32. With the calculated t values that link the measurement and the fitted figure corresponding coordinates, the error for generalized lemniscate parametric equation optimization technique could be calculated as

$$\sum_{t=0}^{1} \left[(\phi_{PE,t} - \phi_{m,t})^2 + (\beta_{PE,t} - \beta_{m,t})^2 \right], \tag{4.45}$$

where $\phi_{PE,t}$ and $\beta_{PE,t}$ are the parametric equation azimuth (x) and elevation (y) values from Equation 4.21 with optimized weights $(a,\ b,\ c,\ d,\ e,\ c_1,\ c_2)$. Both the lemniscate parametric equation optimization and the CST results for the same measurement figure and for the same 56th reel-out phase are given in Table 4.9. It can be seen that the CST method provides a better fit with smaller error than the alternative approach. Therefore, the CST fitting is expanded to all the 86 reel-out phases and the fitted figure becomes an input for the QSM power and kite velocity calculations.

Sum of Squared ϕ and β Errors Between Fit and Measurements			
		[rad]	[deg]
Parametric Eq. method	Figure	0.0566	3.2418°
	Phase	0.5009	28.6981°
CST method	Figure	0.0162	0.9278°
	Phase	0.2439	13.9693°

Table 4.9: The sum of squared azimuth and elevation errors between the fitted figure and the figure from the measurements. The fitting is done with two alternative techniques for the third figure of eight of the reel-out phase of the 56th cycle and for the whole phase.

With the best of two fitting approaches defined still methodological questions concerning the reel-out power calculations remain. It is yet unknown how many points on the fitted figure of eight should be used as QSM inputs. For that reason another convergence study is conducted. Looking at the

measurement figures of eight a single figure is usually given with around 200 points. Depending on the size of the figure and the speed parameters of the kite this number varies. For this convergence study a very conservative figure with 250 points is considered as the ultimate accuracy target. It is then investigate how much the average power calculated deviates form the 250 point value when less points for the fitted figure are used. This power difference in percentage is plotted in Figure 4.44. The power starts rapidly converging when more than 50 points are used for the power calculation. A round number of 100 figure of eight points gives 99.5% accuracy to 250-point value. In an attempt to minimize the computational time yet to keep the accuracy level high the selected number of points is the same 100.

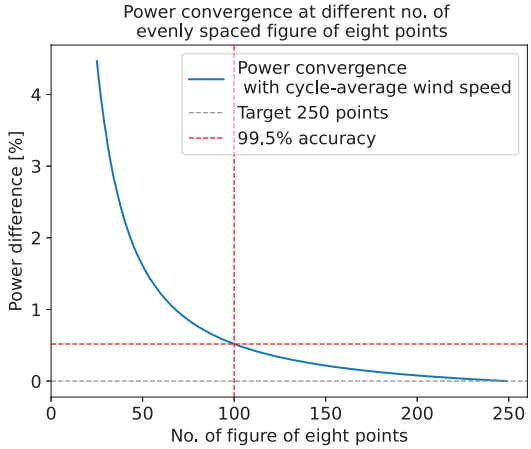

Figure 4.44: Power convergence using the 56th cycle averaged wind and fitted third figure of eight from the same reel-out phase as QSM inputs. 100 evenly spaced points forming the fitted figure give 99.5% power accuracy compared to 250 points. This accuracy could be considered sufficient.

The defined number of figure of eight points enables a good approximation for a single figure of eight but when it comes to the reel-out phase the different radial distances become relevant. For that an additional convergence study is not made and the results from Figures 4.15 and 4.16 are used. As it could be noted the difference between using two radial distances (one at the starting tether length and the other at the ending tether length) and averaging the value gives about 99.85-99.9% accuracy to an alternative of using 100 radial distances. Therefore, the selected number of radial distances has less impact on power results as one would expect. Since the reel-out phase has three figures of eight the number of radial distances selected is three.

For each reel-out phase the kite in the QSM simulation flies three phase-fitted figures of eight with 100 figure points at three different radial distances. The radial distance is kept constant (but the reel-out speed is introduced) during the flight of a single figure and the tether length value changes when the simulation moves to the next figure. The three radial distances are at the start of the corresponding measurement reel-out phase, at the end and a value in the middle. It is important to mention that in reality the power generation cannot happen if the kite is not reeled out but the tether length is kept constant. However, in the QSM the opposite is currently introduced. To enable power calculation the mean reel-out speed from the measurement cycle is passed to the QSM but with a fixed tether-length. This is possible since the QSM makes the power calculation for the current steady-state without knowing the information if the tether length changes for the next steady-state or not.

The other input parameters for the QSM are similar to what are used in the reference simulation in Section 4.1. Each phase has a cycle-averaged wind input and the aerodynamic coefficients as system properties are the optimized values for the reference case. Running the QSM for 86 measurement cycles and using the reference simulation inputs with an exception of kite coordinates and reel-out tether length the phase-averaged power and the kite velocity v_k are calculated for the CST fitted figures of eight. These parameters are again compared to the measured values and the relative difference is plotted in Figures 4.45 and 4.46.

Both the phase-averaged power output and the velocity of the kite experience change in accuracy when compared to the reference simulation in Section 4.1. According to Table 4.10 the median and the mean power experience a negative shift when compared to the reference values in Table 4.4. In

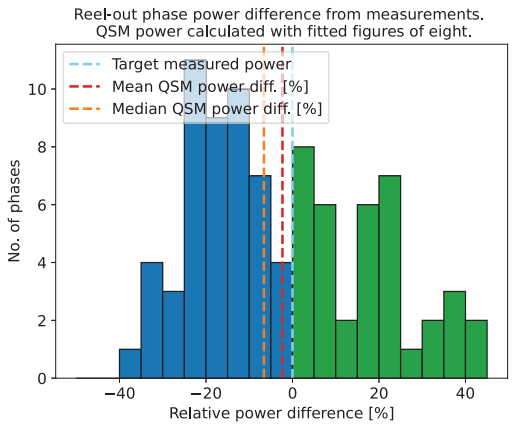

Figure 4.45: Relative power difference of measurement time-averaged reel-out power per phase vs steady-state power calculated using the QSM and the CST fitted figures of eight

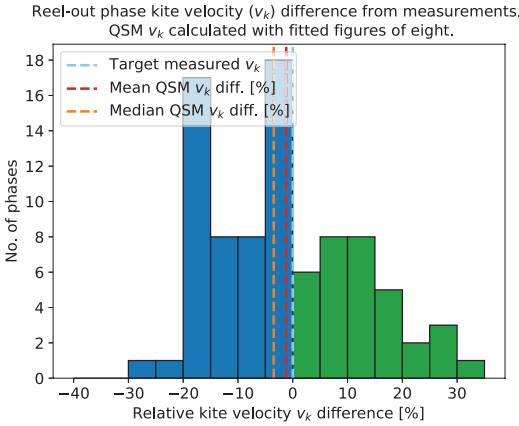

Figure 4.46: Relative kite velocity difference of measurement time-averaged reel-out v_k per phase vs steady-state v_k calculated using the QSM and the CST fitted figures of eight

Reel-Out Phase QSM Output Relative Difference from Measurements Using Fitted Figures of Eight in QSM		
Parameter	**Method**	**Time-Averaged Phases**
Power	Median	-6.604%
	Mean	-2.313%
Kite velocity	Median	-3.474%
	Mean	-1.196%

Table 4.10: Power and kite velocity difference on average over all the 86 reel-out phases between the measurements and using QSM with fitted figures of eight

median value the accuracy has reduced by -2.7%. The same number in mean is -1.7%. Kite velocity v_k follows a similar trend to power accuracy when the QSM is made to follow fitted figures of eight. The median value has turned from reference -0.245% into -3.474%. In case of mean the reduction in accuracy has been -3.3%. The previous accuracy of 2.107% is now -1.196% when compared to the measurement kite velocity.

Hence, both the power and the kite velocity results have a negative shift in accuracy when going from the reference simulation and flying the measured flight path to a flight of fitted figure of eight. The explanation could be threefold.

- Due the loose ends of measurement figure the optimizer has problems placing the centre point of fitted figure of eight. This misplacement is dragging the kite from the ideal straight flight trajectory. One could see that in Figure 4.42. The usual straight flight paths in the middle of the figure of eight (between $[-10, 10]$ deg) are rather winding. These are the paths the kite is flying upwards and the power generation and the kite speed are lower for that section. Due winding flight path the upwards flight becomes more dominant in time-average than it is in the measured flight.

- Separately the simplifications of using few radial distances and a limited number of figure of eight points have small impact on the power accuracy. The difference is ~0.15% and 0.5% from the selected ideal situation. However, the combination of small errors may lead to a bigger power deviation than expected.

- In the QSM calculations with fitted figure the average reel-out speed of the kite is used. This averaged number belongs to the measured figure of eight. If the coordinates of the fitted figure differ from the measurement path the reel-out speed of each steady-state point should also be

different and the resulting average reel-out speed varies from the measurements. Now, the measurement reel-out speed is forced on the CST fitted figure. Additionally, the steady-state points on the fitted figure are distance-wise evenly spaced. This is not the case in the measurement coordinates where the points are measured after a time interval of 0.1 s. This has an additional impact on the kite speed parameters.

4.2.3. Discussions About Reel-Out Flight Path Alternatives

Reel-Out Phase QSM Output Relative Difference From Measurements Using Various Flight Paths as an Input				
Parameter	**Method**	**Measured Coordinates (ref. sim.)**	**Time-Averaged Coordinates**	**Fitted Figure**
Power	Median	-3.923%	0.516%	-6.604%
	Mean	-0.606%	3.470%	-2.313%
Kite velocity	Median	-0.435%	-6.150%	-3.474%
	Mean	2.107%	-5.037%	-1.196%

Table 4.11: Power and kite velocity difference on average/median over all the 86 reel-out phases between the measurements and using QSM with alternative flight path inputs

In Sections 4.2.1 and 4.2.2 two alternative reel-out path representations are described and used in the QSM calculations. One focuses on finding a single azimuth-elevation angle combination from time-averaging the trigonometric functions of measurement coordinates. The angle pair is passed at different radial distances to the QSM steady-state calculations. The other approach fits a general figure of eight, describable with parametric equations, to the measurement figures and the steady-state calculations follow the coordinates from the fitted path. Two techniques for fitting are demonstrated: deforming the general lemniscate equation directly with parameters or using polynomial-formed shape function for the figure of eight modifications. The latter, named the CST method, shows more accurate fitting results and is tested for the power calculations.

The results of alternative flight path representations together with the reference case are condensed into Table 4.11. Comparing the fitted figure of eight QSM output accuracy to using a time-averaged coordinates representation the mean power accuracy is improved and closer to the measurement values with the CST fit. The same goes for the mean kite velocity parameter. Some general comments could be added on this comparison.

- The CST fitted figure of eight QSM input tends to underestimate the time-averaged output power and kite velocity when compared to the measurements.
- With the single reel-out azimuth-elevation set the trend is not so clear as the power estimation goes from the reference simulation power underestimation to overestimation with this technique. In the speed of the kite the opposite is experienced, meaning the time-averaged trigonometric function of course angle is probably not an accurate representation of the reel-out phase.
- Both reel-out path methods show less than +/-7% deviation from the measurement values. The reference simulation where the kite flies measured coordinates in the QSM has an accuracy of more that 99% to the measured power on average (deviation -0.606%). This is a good reference parameter. The fixed azimuth-elevation combination for the whole phase as QSM input has a mean power accuracy loss of $\sim$4.1% from that reference parameter, the CST fit only $\sim$1.7%.
- Based on the example simulations for 86 reel-out phases the CST fitted figure as QSM input tends to be $\sim$2-3% more accurate than by using a fixed set of coordinates. The dilemma for choosing the best method for power calculations goes between few arguments.
  - The CST method requires approximately 300 steady-state points for the reel-out phase calculations if the example in Section 4.2.2 is used. Using the time-averaged values of coordinates only needs about 5 steady-state points, each at different radial distance to calculate the average phase power. The use of CST method is suggested to improve the output power

accuracy of the QSM. However, from the perspective of computational complexity one needs to critically evaluate if the accuracy improvement of 2-3% justifies the selection for a slower method.

– The suitability of method for future power calculations is of question. Time-averaging the measurement coordinates for a fixed set requires the presence of measurement dataset. In the CST method the class function of figure of eight does not need the measurements to be created. But the asymmetries are introduced with an optimized shape function to make a fit to the measurement figure. However, an attempt for finding general weights for shape function could be made by comparing a variation in weight parameters to a change in environmental conditions. This would be a good follow-up study enabling the use of CST method in the future power estimation process.

4.3. Power Optimization of Reel-Out Figure of Eight

The flight of a reel-out figure of eight is based on a principle the relative velocity at maneuvering flight increases in comparison to a non-maneuvering simple kite. This is already proven by Loyd and discussed in Section 2.2. With higher velocity the aerodynamic force and consequently the traction force and the generated power increase. The KCU is responsible for keeping the kite on right maneuvering course to maximize the system output power. Although, in reality the kite deviates from the defined path due weather conditions. This issue is in the scope of control system developers but here the topic of ideal reel-out flight path is discussed from the perspective of mathematical optimization. The idea is to deform a figure of eight into the most optimal path for power production and few examples with discussions are presented.

The figure of eight is a good shape for the reel-out phase. First of all, it enables the maneuvering of the kite while keeping it around $\phi = 0°$ and close to downwind direction. Secondly, this type of movement does not twist the tether as much as a circular or a helical path for instance would do. Therefore, the objective is to keep the principle of figure of eight unchanged but vary the size and the shape of the lobes. The analysis is split into two different elevation cases.

- Flight around $\phi = 0°$ and $\beta = 0°$. This could be denoted as downwind flight. Although, small deviations from the perfect downwind point appear.
- Flight above $\beta \geq 30°$. Looking at the measurements this is about the elevation the kite is usually operated.

The question in scope is: how does the shape of an optimized figure of eight change due cosine loss in these two different elevations? According to Diehl in an ideal flight (without mass) the aerodynamic force is aligned with tether but not with the direction of wind if the kite is operated at an elevation angle larger than zero. This means the total power in wind is reduced. One could calculate this power as

$$P_{wind} = v_w F_a \cos\gamma, \tag{4.46}$$

where γ is the angle between the tether and the vector of downwind. This is the same angle used in the inertial force simulation framework in Chapter 3. The power a flying wing could extract from wind reduces with the decreasing values of a cosine function. This means at small γ angles not much power is lost but at bigger angles the drop in power occurs faster. This is expected to become the key principle in the selection of path the optimizer chooses for the kite to fly at different elevations. [7]

4.3.1. Flight at Ground Elevation

The flight around $\phi = 0°$ and $\beta = 0°$ is investigated in two situations. First, a simplified straight flight path is introduced. This is a bit too ideal case to reflect the reality but provides relevant information for further optimization. As a second situation an optimization for maneuvering reel-out figure of eight is investigated in these downwind conditions.

Straight Flight Path

Before moving to a figure of eight optimization the average power output at different course angles becomes of interest. This could provide some insight about the preferred and the optimal flight directions.

The idea is to fly a straight path horizontally, vertically and at a 45° angle. The kite flies on the given path in both ways when the time-averaged power is calculated. The length of the path is optimizer to select but the total flight time is constrained. Looking at the measurements the kite completes a single figure of eight with approximately 19-21 s. Currently 20 s is chosen for the straight path example. The measurements are also looked at to define a suitable reeling factor f for the QSM calculations. In the 56th cycle during the reel-out it is ~ 0.13. The wind speed is arbitrarily selected to be 10 $\frac{m}{s}$. Other system and environmental properties that are unique for this simulation together with the explained values are given in Table 4.12. These are the additional system properties to the ones already defined in Table 3.1 about Kitepower 20 kW system also used in this section.

Environmental and System Properties for Straight Flight Path Power Opt.			
Wind speed	10 $\frac{\text{m}}{\text{s}}$	Reeling-factor	0.13
Air density	1.225 $\frac{\text{kg}}{\text{m}^3}$	Time	20 s
Tether length	250 m		

Table 4.12: Environmental and system properties that are unique for the straight flight path optimization problem

Since the SLSQP is capable of only minimizing the objective function the average power output is made negative for the optimizaton while keeping the absolute value the same. The optimization problem for this type of experimental straight flight path could be written as

$$\min \; -P_{QSM}(S, \mathbf{a}) \tag{4.47}$$

$$\text{subject to } T_{total} = 20, \tag{4.48}$$

where P_{QSM} is the power calculated with the QSM, S denotes the objective variable path length, $\mathbf{a}$ is a vector of relevant QSM inputs for the calculation and T_{total} is the total time to complete the path in seconds. One of the variables optimizer receives in $\mathbf{a}$ is a selection of possible course angles. For example for the vertical flight these parameters are $\chi = 0°$ and $\chi = 180°$, meaning the kite needs to fly down and up to complete the straight flight path in 20 s. Four sets of course angles are possible and these paths could be seen in Figure 4.47.

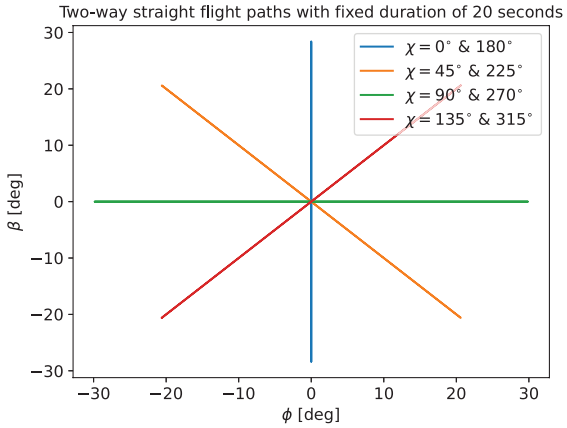

Figure 4.47: Flying a straight path at four different sets of course angles. The target is to finish the two-way flight in 20 s. The length of the path differs since the speed of the kite varies with χ.

Table 4.13 shows the results for the optimization problem presented with Equation 4.47. The highest time-average power results are achieved with the horizontal flight ($\chi = 90°$ and $270°$) which is followed by the diagonal flight and the vertical flight is placed as third. This gives an indication it is beneficial to keep an uniform speed of the kite as it is for the horizontal case. When kite is flying vertically at downwards flight the speed of the kite is boosted by gravity and the path is finished quickly. In contrary

Flying Kite on Straight Flight Path for 20 s (2 ways total)		
Course angles χ on paths	**Total path length [deg]**	**Time-averaged power [W]**
$\chi = 0°$ and $180°$	113.53°	8504.42 W
$\chi = 45°$ and $225°$	116.56°	8800.04 W
$\chi = 90°$ and $270°$	119.40°	9074.59 W
$\chi = 135°$ and $315°$	116.56°	8797.43 W

Table 4.13: Results of the kite flying a straight path. The objective is to maximize the QSM power but fly exactly 20 s.

when the kite is flying at $\chi = 180°$ the kite velocity v_k is slow and also the power generation at this angle is low. Calculating the time-average power the slower upwards flight becomes dominant and hence the calculated power is also smaller than for the alternative flights. The horizontal flight is preferred over flying vertically up and down. Understandably this is not the case anymore if the kite flies only one way at $\chi = 0°$ (and not back at $\chi = 180°$) when the power is maximized according to Schmehl et al. [21]

Flying Figures of Eight

The horizontal flight is a very simplistic case with course angles fixed at known values. Now, the optimization is expanded to figure of eight shape which introduces a broader set of ϕ, β and χ combinations. This creates a need for additional constraints. To define them a default figure of eight as a starting point for the optimization should be specified. The already known lemniscate shape is used here together with the observations from the measured figure of eight. The measurement figure provides an approximate width and height parameters for the lemniscate.

To get a rough indication about the figure of eight parameters Figure 4.11 where the third figure of eight of the 56th cycle is plotted is looked at. This figure has width around 37° and height about 11°. These values bring to coefficients $a_\phi = 0.32$ and $b_\beta = 0.01$ in parametric lemniscate Equations 4.29 and 4.30. The lemniscate is plotted with $c_\phi = 0$ and $c_\beta = 0$ and the corresponding coordinates are passed to the QSM for the flight with default figure. With the environmental and system properties used in the straight flight path optimization (Tables 4.12 and 3.1) the kite completes the flight in 13 s. This time span is shorter than for the measurement figures of eight but it can be explained with better wind conditions and higher kite velocities due flying around $\phi = 0°$ and $\beta = 0°$. This becomes the time constraint for that optimization problem. However, it is used as an inequality constraint to avoid the optimizer from calculating too small figure of eights but to leave enough freedom for the optimization due more complex shape than the straight line.

Environmental and System Properties for FO8 Power Opt. at Downwind Position			
Wind speed	10 $\frac{\text{m}}{\text{s}}$	Time	13 s
Air density	1.225 $\frac{\text{kg}}{\text{m}^3}$	$R_{min,L}$	3.2 m
Tether length	250 m	$R_{min,m}$	10 m
Reeling-factor	0.13	$R_{min,F}$	13 m

Table 4.14: Environmental and system properties that are used for downwind figure of eight optimization. These are the additional properties to the ones presented in Table 3.1 for Kitepower 20 kW system.

In the previous simplistic optimization the maneuvering capabilities of the kite are not considered. Depending on the shape and the size of the kite a minimal turning radius could be defined. To show the difference in optimized shape various turning radiuses could have, three approaches are considered for that constraint. The first R_{min} calculation technique originates from Luchsinger. His R_{min} definition is used in Chpater 3 and given with Equation 3.9. This is a hypothetical absolute minimum which corresponds to kite roll $\psi_R = 90°$. With Kitepower 20 kW pumping kite power system characteristics given in Table 3.1 the minimal turning radius calculates to $R_{min,L} = 3.2$ m. [13]

Another approach for R_{min} calculation is presented by Fechner and Schmehl. [8] They define a non-dimensional turning radius with

$$\varrho = \frac{R}{r}, \tag{4.49}$$

which is a division of turning radius R and tether length r. For 20 kW Kitepower system the estimated value for the non-dimensional turning radius is $\varrho = 3° \approx 0.052$ rad. With tether length $r = 250$ m the minimal turning radius becomes $R_{min,F} = 13$ m. This is a significantly larger number than what is provided with Luchsinger's method of calculation. The third value to validate these calculations is needed which would be realistic and somewhere in between.

This third minimal turning radius parameter is taken from the measurement third figure of eight of the 56th cycle. Knowing the change in course angle with step $d\chi$ and the particular time interval between the measurements T_{step} one could calculate the course rate as

$$\dot{\chi} = \frac{d\chi}{T_{step}}. \tag{4.50}$$

Taking the tangential component of the kite velocity $v_{k,\tau}$ from the measurements then according to Equation 3.68 the turning radius could be calculated as

$$R = \frac{v_{k,\tau}}{\dot{\chi}}. \tag{4.51}$$

Conducting these calculations for every measurement step of figure of eight the smallest of these measurement values is $R_{min,m} \approx 10$ m. With the third alternative value of turning radius a complete set of input parameters required for the optimization is defined and presented in Table 4.14.

The optimization problem itself is based on the CST method described in Section 4.2.2. However, since the objective is not finding the best fit to measured figure of eight but to provide an optimal shape for the power generation, the method is modified. Still ten polynomials as shown in Figure 4.35 are used but only for β direction modifications, not in ϕ direction. This reduces the number of optimization variables significantly and the modifications happening to the shape are more controlled. Additionally, the weights could be found for only polynomials considering a single lobe and then the modifications simply mirrored from the vertical axis, meaning the weights could be identical as $w_{\beta,1} = w_{\beta,6}$, $w_{\beta,2} = w_{\beta,7}$, $w_{\beta,3} = w_{\beta,8}$, $w_{\beta,4} = w_{\beta,9}$, $w_{\beta,5} = w_{\beta,10}$. Furthermore, the centre point of the figure of eight could be placed by c_β and the polynomials peaking at $t = 0$ and $t = 0.5$ which have a direct impact on the centre point of the figure are eliminated from the optimization and set to zero as $w_{\beta,1} = w_{\beta,6} = 0$. This can be justified by moving from the figure of eight fitting where the loose ends of measurement figures require extra parameters for centre point modification to an optimization where the asymmetries to centre are less relevant. Similarly, the centre point location c_ϕ in azimuth direction can be set to zero to ensure the vertical mirroring axis of lobes is situated on $\phi = 0$ and both lobes experience a similar misalignment from the perfect downwind position. The β direction modifications can be applied with the shape function and an extra class function height parameter is not required. Therefore, b_β is also given as a constant to the optimizer $(b_\beta = 0.01)$ but the width a_ϕ is left to be chosen by the optimization algorithm. One could see all the optimization variables used in this problem as column names in Table 4.15.

As a last step before stating the optimization problem the boundaries are defined. It is experienced in the CST fitting the polynomials have large impact on the shape at already small values of weights. In the fitting results Table 4.8 all the weights are between $[-1, 1]$. Derived from that observation the weight boundaries are also set for that gap in the power optimization. Looking at the measurements the width of the whole figure of eight is believed not to be below $20°$ and also not above $60°$. This means the width parameter representing the width of one lobe could have bounds $a_\phi \in [0.175, 0.524]$ rad. The centre point c_β is believed not to deviate too much from the downwind but the boundaries are set for $c_\beta \in [-0.262, 0.262]$ rad. Accordingly, all the parameters for optimization are defined and the problem becomes

$$\min \; -P_{QSM}(w_{\beta,2}, w_{\beta,3}, w_{\beta,4}, w_{\beta,5}, c_\beta, a_\phi, \mathbf{a}), \tag{4.52}$$

$$\text{subject to } T_{total} \geq 13, \; R \geq R_{min}, \tag{4.53}$$

$$w_{\beta,2} \ldots w_{\beta,5} \in [-1, 1],$$

$$a_\phi \in [0.175, 0.524],$$

$$c_\beta \in [-0.262, 0.262].$$

The results with the three different R_{min} values are plotted in Figure 4.48 and the weight parameters together with the time-average power are given in Table 4.15. To understand the flight path optimizer has selected the instantaneous power, the course angle and the kite tangential velocity dependence on time are shown in Figures 4.49 and 4.50.

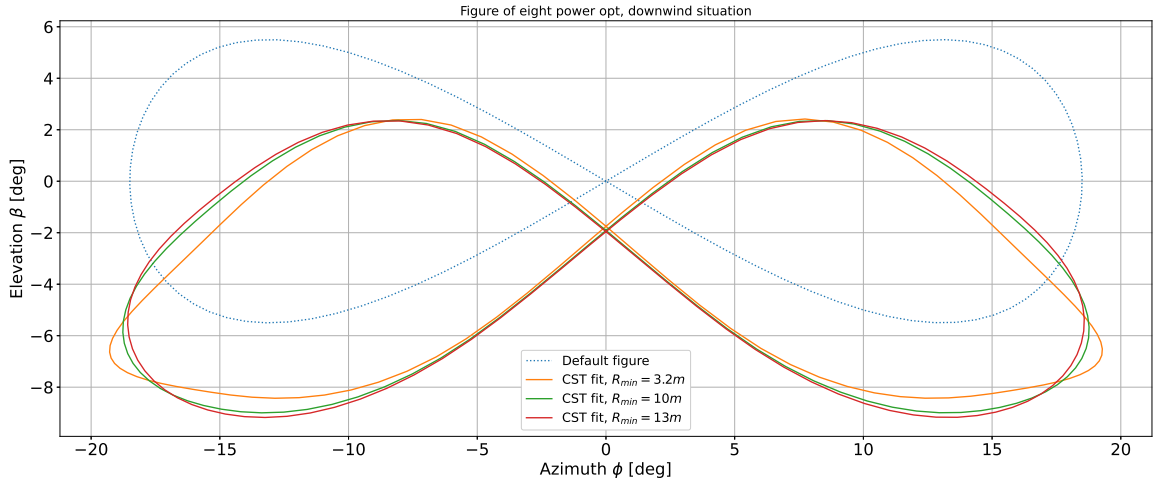

Figure 4.48: Power-optimized figures of eight around downwind position. The figures differ in R_{min} constraint set.

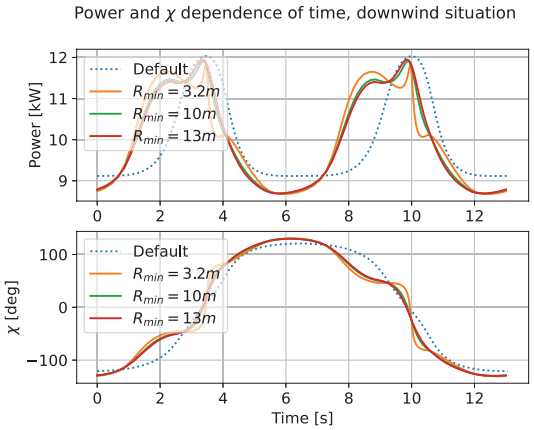

Figure 4.49: Power and course angle χ variation in time for downwind figure of eight simulation

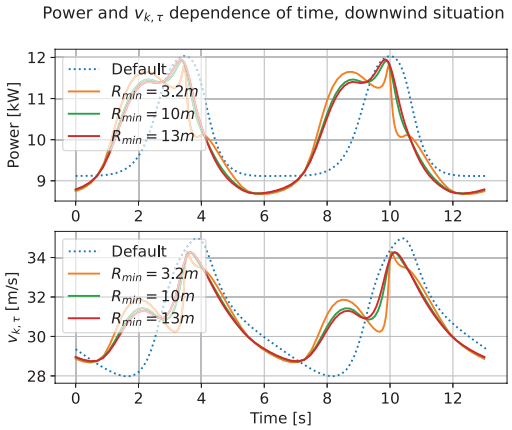

Figure 4.50: Power and tangential kite velocity $v_{k,\tau}$ variation in time for downwind figure of eight simulation

The differences between the results with various R_{min} values for downwind figure of eight optimization one could observe from Figure 4.48 are very small. The $R_{min} = 3.2$ m enables the kite to turn faster and the figure follows a more optimal path after each turn than for the other two figures. But in a bigger picture the shapes are similar and the comments are conducted on a general level and applicable for all the three figures.

- At elevation angles close to zero the cosine losses are small. This means the optimizer is not necessarily trying to flatten the figure of eight at ground level $\beta = 0°$ and the deviations in vertical

direction could be beneficial for the power generation if the kite experiences better course angles (χ close to zero).

- The kite starts the flight from the centre point with the left lobe first and the upper half of the lobe is passed for a start. If the kite needs to increase the elevation angle the changes are preferably done keeping the course angle as close to $\chi = 135^\circ$ or -135°. These angles have the best elevation change pace vs power generation balance. This way the kite manages to increase the elevation and as could be seen in Figure 4.49 the power does not drop too much below 9 kW.

- Flying downwards results in a bigger power production. To increase the time-averaged power the objective is to keep the kite in decreasing elevation flight for as long as possible. The course angles $\chi = 45^\circ$ and -45° are beneficial in that sense. The peak power becomes lower than compared to the default figure of eight, where for a short time the kite flies almost vertically downwards, but high power is kept for a longer period in optimized flight path. This results in higher overall power generation.

- The idea is to keep the tangential kite speed as uniform as possible (Figure 4.50). This means reducing the maximum kite velocity at power peaks to keep the kite in that position for prolonged period of time and increase the velocity at lower power periods to get through these low generation phases as fast as possible.

- The kite is shifted below the ground level because of the radial component sign of gravity. From Equation 2.43 the gravity points downwards on the tangential plane in both cases when the kite is above or below the ground level but the radial component switches the sign and increases tether force below $\beta \leq 0^\circ$. It is preferred to conduct upwards flights with lower power production below the ground level to increase the tether force in these conditions.

- The figures have some parts above the ground level because shifting it more into negative elevation would lose the benefits of being close to the downwind position.

The optimized path is very logical from the scope of maximizing the power and the chosen combination of angles could be justified based on the previous list of observations.

Figure of Eight Power Optimization Results. Downwind Situation. Coeff. in [rad]								
	$w_{\beta,1}$ & $w_{\beta,6}$	$w_{\beta,2}$ & $w_{\beta,7}$	$w_{\beta,3}$ & $w_{\beta,8}$	$w_{\beta,4}$ & $w_{\beta,9}$	$w_{\beta,5}$ & $w_{\beta,10}$	c_β	a_ϕ	Avg. power
Default	0	0	0	0	0	0	0.3229	9937.4 W
R_{min} = 3.2 m	0	-0.5676	0.7116	-1.0000	0.5868	-0.0305	0.3366	10018.4 W
R_{min} = 10 m	0	-0.2838	0.5188	-0.6697	0.5116	-0.0333	0.3276	10002.7 W
R_{min} = 13 m	0	-0.1794	0.4727	-0.5603	0.5185	-0.0341	0.3243	9998.3 W

Table 4.15: Optimization variables from the downwind figure of eight optimization together with the objective function final value as the time-averaged power output.

As a mathematical exercise to investigate how the average power changes, one of the optimized figures of eight is flipped vertically from the ground level. This approach could be seen in Figure 4.51 and the time variation of parameters in Figures 4.52 and 4.53. Two figures are compared to each other.

- The power of the flipped figure of eight is lower than it is for the optimized and default figures. This is presented with Table 4.16.

- The power curve of the flipped figure of eight is also a mirrored version of optimized graph but with small deviations. The peak power is lower for the flipped figure and lower power level between 6-9 s lasts longer than for the optimized variant.

- The drop in power for the flipped figure could be explained by reversed effect of gravity vector. Due the orientation of the radial gravity component above the ground (negative) the latter has a small decreasing effect on tether force and generated power.

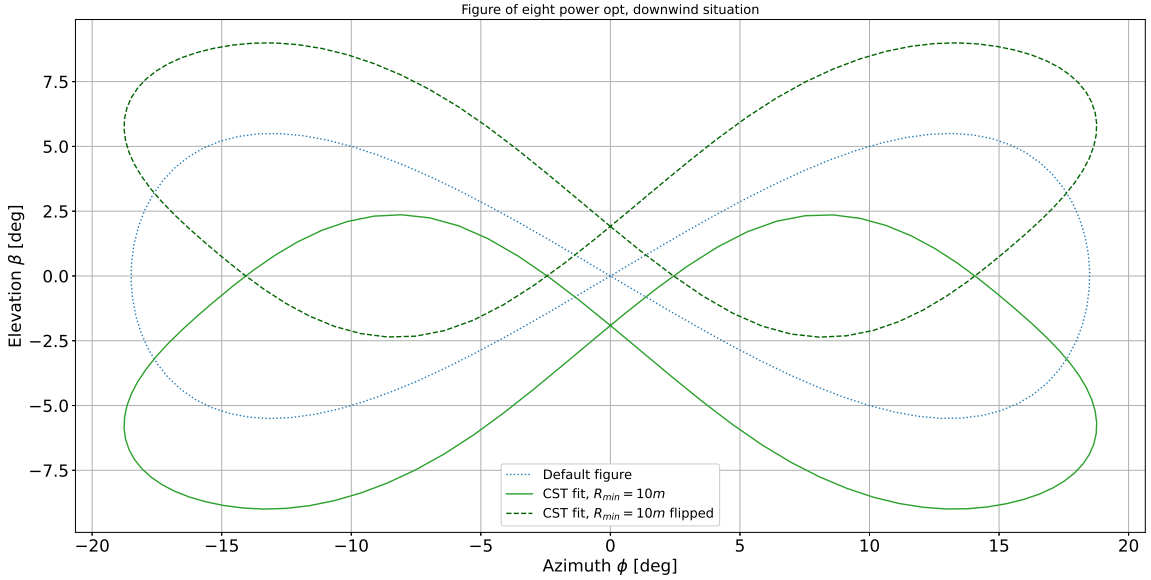

Figure 4.51: Optimized figure of eight with $R_{min} = 10$ m and the vertically flipped version of it

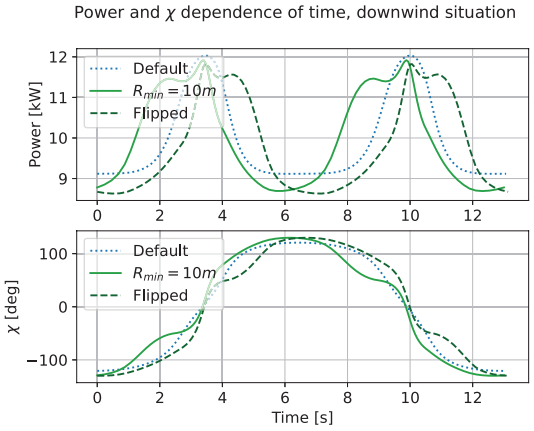

Figure 4.52: Power and course angle χ variation in time of optimized and vertically flipped figure of eight

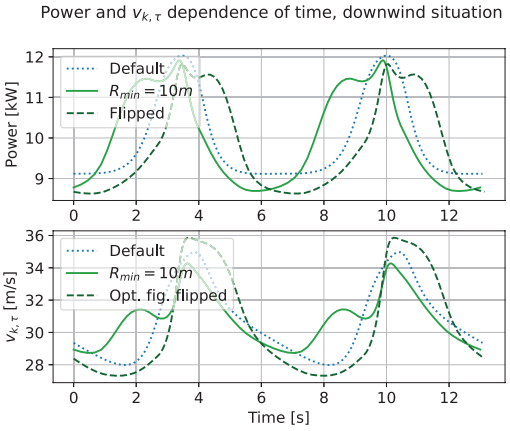

Figure 4.53: Power and tangential kite velocity $v_{k,\tau}$ variation in time of optimized and vertically flipped figure of eight

- For maximized power output the objective is to keep $v_{k,\tau}$ as uniform as possible. However, flipping the figure works against that principle and the difference between the highest and the lowest velocity is large for that figure.

Because of the directional change of radial component in gravity the optimizer chooses the selected path for a reason and flipping it would have a reverse impact of power reduction due the asymmetrical properties of the figure. This type of optimization has given an insight of possible factors having an impact on figure of eight. However, flying below the surface of the ground or even at low elevations close to the ground is unrealistic. Therefore, the optimization is expanded to the measurement elevations where the figures are flown on usual basis.

4.3.2. Flight at Measured Elevations

The optimization concept of maximizing figure of eight time average power which is introduced in Section 4.3.1 is modified here for measurement elevations. The default starting point figure of eight is the same lemniscate representation of the third figure of the 56th reel-out phase which is optimized with an additional constraint of flying above 30°. This is the elevation region the figure appears in the measurements. To make an estimation about the new time limit for the optimization the default figure is placed

Optimized Figure vs Flipped Figure Power. Downwind Situation.	
Default	9937.4 W
R_{min} = 10 m, original	10002.7 W
R_{min} = 10 m, flipped	9814.0 W

Table 4.16: Time-averaged power of default, optimized and vertically flipped optimized figure of eight

to centre at $\phi = 0°$ and $\beta = 35.5°$. This ensures the lower elevation limit of figure is at 30° and the rest of the figure remains at larger elevations. Flying the kite with the same fixed environmental and system properties the QSM calculates 19 seconds for the duration. This is a very realistic number since the completion time of a single measured figure is about the same. With the newly defined constraint the properties for this type of elevated simulation are given in Table 4.17.

Environmental and System Properties for FO8 Power Opt. at $\beta \geq 30°$			
Wind speed	10 $\frac{\text{m}}{\text{s}}$	Time	19 s
Air density	1.225 $\frac{\text{kg}}{\text{m}^3}$	$R_{min,L}$	3.2 m
Tether length	250 m	$R_{min,m}$	10 m
Reeling-factor	0.13	$R_{min,F}$	13 m

Table 4.17: Environmental and system properties that are used for figure of eight optimization above 30°. These are the additional properties to the ones presented in Table 3.1 for Kitepower 20 kW system.

The optimization boundaries for the elevated flight remain mainly the same as defined in Section 4.3.1. The one exception originates from the vertical centre point location c_β which is now essentially out of the previous bounds due the elevation change. The lower end is limited with 30° while the upper end could be allowed to go about 60°. Above that elevation the aerodynamic force due misalignment with wind vector tends to be too small to keep the particular kite in the air. In radians these bounds mean $c_\beta \in [0.52, 1.05]$ rad. All the other bounds and constraints which are not directly influenced by the elevation change stay the same as in the previous section. This goes also for the case distinction of minimal turning radius. The optimization problem becomes

$$\min \; -P_{QSM}(w_{\beta,2}, w_{\beta,3}, w_{\beta,4}, w_{\beta,5}, c_\beta, a_\phi, \mathbf{a}), \tag{4.54}$$

$$\text{subject to } T_{total} \geq 19, \; R \geq R_{min}, \tag{4.55}$$

$$w_{\beta,2}...w_{\beta,5} \in [-1, 1],$$

$$a_\phi \in [0.175, 0.524],$$

$$c_\beta \in [0.523, 1.046],$$

where vector **a** includes all the environmental and system properties passed to the objective function. The resultant figures of eight of the optimization problem Equation 4.54 are presented in Figure 4.54 with the optimization variables presented in Table 4.18.

One could clearly see from the graphs the optimized figures have lost their characteristics of figure of eight. The reasons for these results together with other observations are discussed.

- At angles above 30° the cosine loss from Equation 4.46 starts to increase rapidly. This is due the specific features of a cosine function. The loss with every extra degree in elevation consequently causing bigger misalignment with wind vector is larger than the potential gain the system could earn from varying the course angle. The optimizer attempts to lower the elevation at every possible flight point as much as possible.

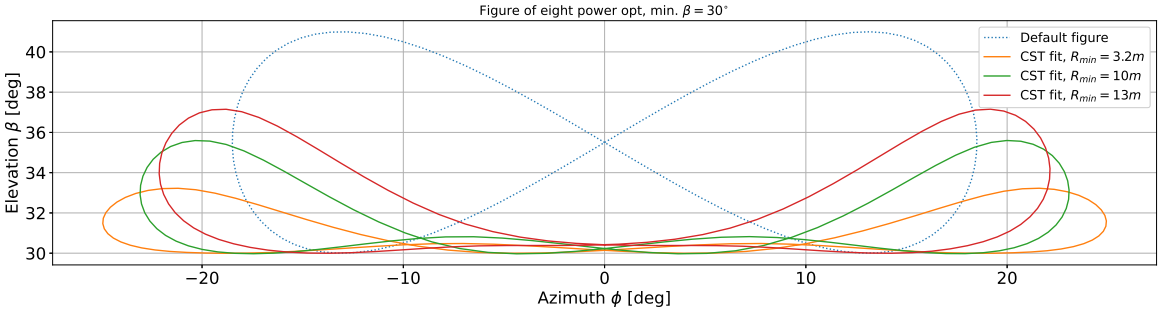

Figure 4.54: Power-optimized figures of eight at elevations above 30°. The figures differ in R_{min} constraint set.

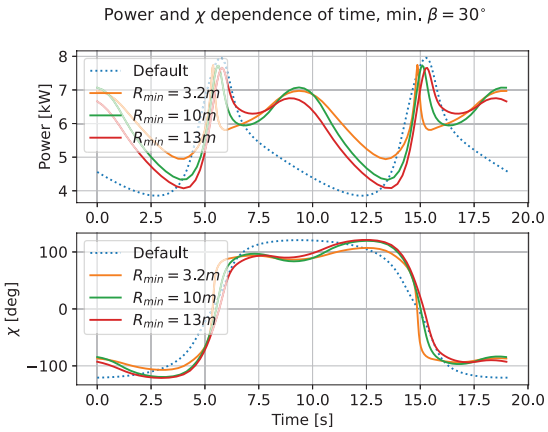

Figure 4.55: Power and course angle χ variation in time for $\beta \geq 30^\circ$ figure of eight simulation

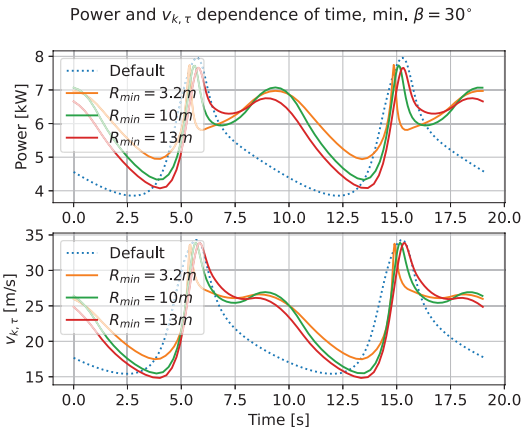

Figure 4.56: Power and tangential kite velocity $v_{k,\tau}$ variation in time for $\beta \geq 30^\circ$ figure of eight simulation

- The difference between various R_{min} constraints is well distinguished in Figure 4.54. The optimizer increases the elevation just as much the kite could make the turn with minimal turning radius and fly back.
- As could be seen from Figure 4.55 the default figure of eight gets comparably high power level to optimized figures as it gets close to $\beta = 30^\circ$ at ~ 6 & 16 s. But the power output is also similar right before the peaks when the kite is at higher elevations but flies downwards. This the only not at the minimal elevation flight condition that could show similar results. Although, to fly at $\chi = 0^\circ$ the kite needs to gain elevation first and this is a big loss.
- The tangential kite velocity $v_{k,\tau}$ is more uniform for the optimized flight paths. This is also logical since the kite flies mostly horizontally where the velocity vector is perpendicular to the gravity vector.

The defined constraints are not restricting the optimizer enough to keep the characteristic features of figure of eight. Although, from minimal turning radius R_{min} perspective this type of flight could hypothetically be possible it is not very realistic. The figure of eight is only flat because the minimal elevation constraint. In reality the kite would fly below that elevation but causing a new set of problems (e.g. reduced safety). An alternative approach for elevated figure of eight optimization should be used. Some insight with the directions for the follow-up study are suggested in Section 4.3.3.

4.3.3. Discussions About Figure of Eight Power Optimization

Sections 4.3.1 and 4.3.2 show flying the most optimal reel-out figure of eight is crucial from the perspective of time-averaged power generation. The optimization results at elevation angles above 30° show an improvement from the default figure of eight time-averaged power 5120.9 W to the most promising power result of 6077.8 W from the optimized figure. However, this gain comes with a cost of losing

Figure of Eight Power Optimization Results. Min β = 30°. Coeff. in [rad]								
	$w_{\beta,1}$ & $w_{\beta,6}$	$w_{\beta,2}$ & $w_{\beta,7}$	$w_{\beta,3}$ & $w_{\beta,8}$	$w_{\beta,4}$ & $w_{\beta,9}$	$w_{\beta,5}$ & $w_{\beta,10}$	c_β	a_ϕ	Avg. power
Default	0	0	0	0	0	0.6196	0.3229	5120.9 W
R_{min} = 3.2 m	0	-0.2827	-0.5801	0.3628	0.5270	0.5261	0.4352	6077.8 W
R_{min} = 10 m	0	-0.0691	-0.8122	0.6860	0.7256	0.5276	0.4028	5921.3 W
R_{min} = 13 m	0	-0.2148	-0.6107	0.4816	-0.7285	0.5309	0.3862	5777.3 W

Table 4.18: Optimization variables from above 30° figure of eight optimization together with the objective function final value as the time-averaged power output.

the characteristic shape of figure of eight and with viable figure solution the increase would probably be smaller. The solution for a more realistic power output change requires further optimizations with a different approach and/or using additional optimization constraints.

The selected flight path gets a new level of importance when inertial forces are included in the simulation framework. Equation 3.1 shows how the magnitude of centrifugal force is directly dependent on turning radius R. The smaller the turning radius the bigger impact of centrifugal force the system has. According to the results presented in Section 3.4 at certain larger cone angles γ this could have gaining impact on tether force and output power. Yet, the centrifugal force caused roll could serve an opposite effect at smaller γ values as well. Supported by other inertial forces (e.g. coriolis force) the power results could be very different to what one is calculating with the current QSM. Especially, if the simulations are conducted for rigid wing where the inertial effects are more perceptible due bigger mass and higher velocity of the wing. This again shows the importance of selecting R for optimizations correctly. Based on this train of thought some general remarks for the future optimizations could be brought out.

- When running the simulations around the perfect downwind position the effect of gravity has unreal impact on the system due flight below the ground level. The small cosine losses at elevations close to zero retain the characteristic shape of figure in optimizations but one cannot be sure the output shape is the most optimal in realistic flight conditions. A flight close to ground but with an additional constraint of $\beta \geq 0°$ could be experimented with. This solves the issues with gravity.

- In the flight with inertia R is a more relevant parameter than in the current QSM. One could optimize for the balance between R big enough to keep the centrifugal impact low but just as small to complete the turning maneuvers rapidly and keep the kite on optimal path. This turning radius problem requires more information from tested systems as the kite can fly R_{min} under certain conditions. These constraints that define the possible minimal turning radius could be the speed of the kite and the tether length. Additionally, due inertia the change from one turning radius to another experiences delay which is currently not considered in the optimization framework.

- The most optimal size for the reel-out shape is yet unknown. This is a balance between keeping the kite close to $\phi = 0°$ where the alignment with downwind is better vs keeping the tangential kite speed $v_{k,\tau}$ as uniform and high as possible which requires a change in ϕ and β coordinates at optimal course angles χ. The current size of the figure of eight is forced on the optimizer with the time constraint. The latter should be investigated as well.

- Alternative optimization techniques could be used. Classical optimization approach (used here) which creates a single point in each iteration and uses gradient to calculate the direction for the next point might not be the best option in a complex optimization problem. Some of the results could be local minimas but not global. Another approach would be genetic algorithm which makes a population of points at each iteration and selects the minimal value points. The next population is generated and the selected points are compared. This may give better results since the problem is not very deterministic and linear in the flight path optimization. [14]

5

Conclusions and Recommendations

An earlier validation study showed that the output power of the quasi-steady model (QSM) deviated from the flight measurement power. This has been an indication that the assumptions and simplifications made in the model need to be reassessed. In this thesis, the assumptions concerning the turning maneuvers of the kite have been investigated. The question in scope was how much accuracy in the QSM could be gained by including additional details on the turning maneuvers of the kite. To answer the main research question, two sub-questions were tackled. First, it was researched how the simulated reel-out paths can be resolved with inertial effects. These inertial effects had been excluded from the QSM as a simplification in earlier studies. In this thesis the inertial forces were added to a simplified reel-out flight framework and the effect of inertia was quantified for a lightweight soft wing kite. Second, it was studied which representative reel-out flight paths in the QSM simulations yield the most accurate power output. In a pevious study, the QSM reel-out path had been assumed to follow a straight line without any turning maneuvers. In this thesis, the loss of QSM output power accuracy caused by this simplification was estimated. This was complemented by an investigation of reel-out figure of eight parameterization. Flying the developed geometry representation of the figure of eight enabled turning maneuvers in the simulation. The QSM accuracy gain from this addition was quantified. Subsequently, the figure of eight parameterization technique was used for a different purpose: to find the figure of eight that maximizes the power output.

To address the first research sub-question of resolving the reel-out turning maneuvers with inertial effects inertial force equations were studied first. These equations required setting the turning radius to solve them. The first step to overcome the absence of a known turning radius in asymmetric figures is to fly a path with a predefined radius and observe the impact of inertia at first in a simplified simulation framework. For that purpose, both circular and helical trajectory flight paths were investigated in the thesis. First, the inertial equations were analytically derived in Cartesian coordinates for the simplified simulation framework. The developed set of equations could be used to verify the inertial force equations proposed by previous authors. This was followed by adapting the inertial equations presented by Schmehl et al (2013) in spherical coordinates and in QSM. This implementation required an introduction of a new parameter in the QSM called the course rate. The latter shows the rotation speed of the kite on a tangential plane.

Both the analytically developed set of equations and the new contribution to the QSM were tested in a specific helical flight simulation where the tether sweeped a conical surface around the downwind axis. The two alternative approaches reached the same results in this framework and verified each other. It was observed at larger cone angles, meaning the tether length was rather short but the turning radius was large, that the inertial effect can increase the tether force and the power output. With small cone angles the effect was the opposite. Based on the example case, the impact of the inertial effects on the output power computed with the QSM is limited to 1-2% for lightweight soft kites. This marks a simulation accuracy improvement with the inclusion of inertia in the maneuvering flight of a flexible wing.

In response to the second sub-question about reel-out flight paths and their impact on the output power accuracy of QSM, reference simulations were set up. As a QSM input, a flight measurement set of 86 reel-out phases provided by Kitepower was used. The objective was to have minimal median

power and kite velocity error between the QSM outputs and the measurements assuming the kite is made to follow the exact coordinates from the flight data. This way QSM was tuned for particular measurements by optimizing a suitable set of reel-out aerodynamic coefficients: $C_{L,out}$ = 0.60 and $C_{D,out}$ = 0.13. The reference simulations were used to quantify the accuracy of alternative reel-out flight paths.

With the fixed reference simulations the impact of two alternative approaches for the reel-out flight path on the QSM output accuracy were compared. The first method did not resolve the maneuvering flight but made the kite fly a straight line with a constant azimuth, elevation and course angle. These fixed angles were calculated by time-averaging the trigonometric functions of measurement angles. This path representation was in use in the QSM. Applying the time-averaging technique to all measurement 86 reel-out phases the average power accuracy loss experienced was +4.1% compared to the reference simulations.

The second option for reel-out path representation examined considered fitted figures of eight to the measured flight path. Two figure of eight parameterization techniques were investigated. The first technique used a parametric equation of a known figure of eight, lemniscate of Gerono, which has weights included for asymmetric modifications to the figure. An optimization problem was set for finding these weights to minimize the geometric difference between the lemniscate and the measured figure. The second technique used a general equation for the figure of eight as a class function. To introduce asymmetric properties on the fitted figure a shape function was used. The optimization variables in this optimization problem were the weight parameters in that shape function. The multiplication of the class and the shape function led to a fitted figure of eight. This method is named class function/shape function transformation technique (CST). The latter also showed better results in the least squares fitting and was, therefore, the only fitting technique used when expanding the approach to the 86 measurement reel-out phases. Making the kite fly the fitted figure in QSM and comparing the power outputs to the reference simulations the CST fit showed a -1.7% deviation in time-averaged power results. Hence, the CST-fitted figure of eight as the QSM input yielded more accurate power output results than flying a straight line with constant angles.

The CST technique was also tested on the figure eight modification with the objective to find the most optimal path for maximizing power generation. The optimizations were conducted for flying the figure in perfect downwind elevation $\beta = 0^\circ$ (unrealistic) and above $\beta \geq 30^\circ$ (realistic) conditions using a set of constraints. For the downwind case, the optimized path retained the characteristics of the figure of eight and a power improvement of $\sim$1% was observed from the generalized lemniscate shape with the approximated size of measurement figures. Above 30° elevations the optimizer tried to lower the elevation coordinates in every possible figure of eight point and the path was deformed to an unrealistic shape for the kite to fly. This indicated that the flight path optimization requires additional constraints to count for the cosine loss of power in winds at elevated heights.

Follow-up studies to this thesis could be conducted in three fields. Firstly, the inertial equations in the circular path could be expanded to a reel-out figure of eight. The inclusion of a turning radius of the kite in simulations is likely to become a key problem, but three options are suggested to overcome this issue.

- The turning radius can be made into a simulation control parameter with the limiting values originating from the theories of Luchsinger (2013) or Fechner (2018).
- The turning radius variable can be calculated from measurements by, for example, averaging the parameter and using it for the particular figure or phase.
- A specific turning radius can be used for each steady-state point. This requires the kite coordinates from the previous or following steady-state to estimate how much the course angle changes between steady-state steps which gives directly the course rate needed in inertial equations.

For the second follow-up study, the CST fitting and fixed azimuth-elevation combination approaches should be tested with more flight data to confirm the small impact on power output accuracy of these simplifications. Finally, the search for the most optimal reel-out flight path requires a reassessment of the chosen constraints. These include flight time and turning radius. Additional constraints may be required to ensure that the figure of eight is feasible for the kite to fly. It is also recommended to try to solve this complex power maximizing optimization with genetic optimization which may perform better than classical optimization algorithms in the context of the given problem.

A

Optimization with Quadratic Programming

In this paper the commonly used optimization technique is the Sequential Least Squares Programming (SLSQP). This optimization tool is a part of SciPy library and aims to minimize the function. By definition the optimization problem SLSQP algorithm tackles is

$$\begin{aligned} &\min f(x) \\ &\text{subject to } c_i(x) = 0,\ i \in \mathcal{E} \\ &\qquad\qquad c_i(x) \geq 0,\ i \in \mathcal{I}. \end{aligned} \tag{A.1}$$

When linearizing the constraints the problem becomes

$$\begin{aligned} &\min f_k + \nabla f_k^T p + \frac{1}{2} p^T \nabla^2_{xx} \mathcal{L}_k p \\ &\text{subject to } \nabla c_i(x_k)^T p + c_i(x_k) = 0,\ i \in \mathcal{E} \\ &\qquad\qquad \nabla c_i(x_k)^T p + c_i(x_k) \geq 0,\ i \in \mathcal{I} \end{aligned} \tag{A.2}$$

where $\mathcal{L}_k$ is the Lagranian and p the search direction. [17]

Depending on the optimization problem the function to be minimized is defined uniquely. For example, in figure of eight power maximization it is the negative value of time-averaged QSM power output that is to be minimized when the kite is flying a figure of eight. In the search for the best fit the sum of squared residuals between the function output and the measured value is to be minimized. In the latter the least square fitting technique is used where the sum of squared residuals is given as

$$S_R \equiv \sum_{i=1}^{n} [y_i - f(x_i, \mathbf{a})]^2. \tag{A.3}$$

In this equation **a** denotes the vector of all the arguments used in the function which would give from input x_i the corresponding function output $y_{i,f}$. This is subtracted from the measurement value y_i. In this paper the least square fitting technique is used in various similar optimization problems (e.g. for finding the optimal aerodynamic coefficients). [16]

Bibliography

[1] I. Argatov, P. Rautakorpi, and R. Silvennoinen. “Estimation of the mechanical energy output of the kite wind generator”. In: *Renewable Energy* 34.6 (2009), pp. 1525–1532.

[2] Calculator.net. *Triangle Facts, Theorems and Laws*. 2021. URL: https://www.calculator.net/triangle-calculator.html (visited on 07/01/2021).

[3] A. Cherubini et al. “Airborne Wind Energy Systems: A review of the technologies”. In: *Renewable and Sustainable Energy Reviews* 51 (2015), pp. 1461–1476.

[4] Global Wind Energy Council. *GWEC Global Wind Report 2021*. 2021. URL: https://gwec.net/global-wind-report-2021/ (visited on 05/27/2021).

[5] Our World in Data. *How much energy does the world consume?* 2020. URL: https://ourworldindata.org/energy-production-consumption#how-much-energy-does-the-world-consume (visited on 04/27/2021).

[6] M. De Lellis et al. “The Betz limit applied to airborne wind energy”. In: *Renewable Energy* 127 (2018), pp. 32–40.

[7] M. Diehl. “Airborne Wind Energy: Basic Concepts and Physical Foundations”. In: *Airborne Wind Energy*. Ed. by U. Ahrens, M. Diehl, and R. Schmehl. Berlin, Heidelberg: Springer Berlin Heidelberg, 2013, pp. 3–22. ISBN: 978-3-642-39965-7. DOI: 10.1007/978-3-642-39965-7_1.

[8] U. Fechner and R. Schmehl. “Flight Path Planning in a Turbulent Wind Environment”. In: *Airborne Wind Energy: Advances in Technology Development and Research*. Ed. by R. Schmehl. Singapore: Springer Singapore, 2018, pp. 361–390. ISBN: 978-981-10-1947-0. DOI: 10.1007/978-981-10-1947-0_15.

[9] Kitepower. *KitePower Technology*. 2012. URL: http://www.kitepower.eu/technology.html (visited on 03/04/2021).

[10] B. M. Kulfan. “Universal parametric geometry representation method”. In: *Journal of aircraft* 45.1 (2008), pp. 142–158.

[11] M. L. Loyd. “Crosswind kite power (for large-scale wind power production)”. In: *Journal of energy* 4.3 (1980), pp. 106–111.

[12] The Numerical Algorithms Group Ltd. *E04 — Minimizing or Maximizing a Function*. 2013. URL: https://www.nag.com/numeric/mb/manual64_24_1/html/e04/e04intro.html (visited on 03/30/2021).

[13] R. H. Luchsinger. “Pumping Cycle Kite Power”. In: *Airborne Wind Energy*. Ed. by U. Ahrens, M. Diehl, and R. Schmehl. Berlin, Heidelberg: Springer Berlin Heidelberg, 2013, pp. 47–64. ISBN: 978-3-642-39965-7. DOI: 10.1007/978-3-642-39965-7_3.

[14] Mathworks. *Genetic Algorithm. Find global minima for ighly nonlinear problems*. 2021. URL: https://www.mathworks.com/discovery/genetic-algorithm.html (visited on 06/18/2021).

[15] MathWorld. *Bernstein Polynomial*. URL: https://mathworld.wolfram.com/BernsteinPolynomial.html (visited on 04/04/2021).

[16] MathWorld. *Least Squares Fitting*. URL: https://mathworld.wolfram.com/LeastSquaresFitting.html (visited on 04/05/2021).

[17] J. Nocedal and S. Wright. “Sequential Quadratic Programming”. In: *Numerical Optimization*. New York, NY: Springer New York, 2006, pp. 529–562. ISBN: 978-0-387-40065-5. DOI: 10.1007/978-0-387-40065-5_18.

[18] A. Roullier. “Experimental analysis of a kite system’s dynamics”. MA thesis. École polytechnique fédérale de Lausanne (EPFL), Mar. 2020.

[19] M. Schelbergen and R. Schmehl. “Validation of the quasi-steady performance model for pumping airborne wind energy systems”. In: *Journal of Physics: Conference Series*. Vol. 1618. 3. IOP Publishing. 2020, p. 032003.

[20] R. Schmehl. *Airborne Wind Energy. An introduction to an emerging technology*. 2019. URL: http://www.awesco.eu/awe-explained/ (visited on 04/07/2021).

[21] R. Schmehl, M. Noom, and R. van der Vlugt. “Traction Power Generation with Tethered Wings”. In: *Airborne Wind Energy*. Ed. by U. Ahrens, M. Diehl, and R. Schmehl. Berlin, Heidelberg: Springer Berlin Heidelberg, 2013, pp. 23–45. ISBN: 978-3-642-39965-7. DOI: 10.1007/978-3-642-39965-7_2.

[22] H. A. Souza. *Non-symmetrical lemniscate curve parameterization*. 2016. URL: https://math.stackexchange.com/questions/1808380/non-symmetrical-lemniscate-curve-parameterization (visited on 03/30/2021).

[23] *Spherical coordinate system*. 2021. URL: https://en.wikipedia.org/wiki/Spherical_coordinate_system (visited on 05/20/2021).

[24] R. van der Vlugt, J. Peschel, and R. Schmehl. “Design and Experimental Characterization of a Pumping Kite Power System”. In: *Airborne Wind Energy*. Ed. by U. Ahrens, M. Diehl, and R. Schmehl. Berlin, Heidelberg: Springer Berlin Heidelberg, 2013, pp. 403–425. ISBN: 978-3-642-39965-7. DOI: 10.1007/978-3-642-39965-7_23.

[25] R. van der Vlugt et al. “Quasi-steady model of a pumping kite power system”. In: *Renewable Energy* 131 (2019), pp. 83–99.

[26] S. Watson et al. “Future emerging technologies in the wind power sector: A European perspective”. In: *Renewable and Sustainable Energy Reviews* 113 (2019), p. 109270.

[27] E. W. Weisstein. *Eight curve*. 2004. URL: https://mathworld.wolfram.com/EightCurve.html (visited on 03/30/2021).

[28] M. West. *Spherical coordinates*. 2015. URL: https://dynref.engr.illinois.edu/rvs.html#rvs-eb-d (visited on 05/20/2021).